

**FACULTY  
OF MATHEMATICS  
AND PHYSICS**  
Charles University

**DOCTORAL THESIS**

Juraj Lörinčík

**Magnetic reconnection and its manifestations  
in solar flares and eruptions**

Astronomical Institute of Charles University

Supervisor of the doctoral thesis: doc. RNDr. Jaroslav Dudík, PhD.

Study programme: Theoretical Physics, Astronomy, and  
Astrophysics (P4F1)

Prague 2021



I declare that I carried out this doctoral thesis independently, and only with the cited sources, literature and other professional sources. It has not been used to obtain another or the same degree.

I understand that my work relates to the rights and obligations under the Act No. 121/2000 Sb., the Copyright Act, as amended, in particular the fact that the Charles University has the right to conclude a license agreement on the use of this work as a school work pursuant to Section 60 subsection 1 of the Copyright Act.

In Prague, Jun 30th, 2021

.....



In the first place, I would like to thank doc. RNDr. Jaroslav Dudík, PhD., whose supervision, starting eight years ago during my undergrad studies, is finally coming to an end. I take this opportunity to thank him for involving me in interesting projects, overseeing my scientific and personal development, and for being a good friend. I wouldn't be able to call myself a scientist if it weren't for all the energy he invested in making me one. I owe immense gratitude to Dr. Guillaume Aulanier for the patience he was not obliged to have, for sharing with me his profound knowledge of physics, and teaching me how to effectively communicate my results.

I am thankful to my colleagues from the Astronomical Institute of the Academy of Sciences of the Czech Republic, the Astronomical Institute of Charles University, and the Paris Observatory in Meudon for creating such stimulating working environments.

I want to express a never-ending gratitude to my parents, who did everything to make me feel excited about science and the world around me. Finally, I thank my fiancée Dominika, who has been showing me that there are other things to live for than work, yet at the same time motivating me when I no longer had the strength to continue.



Title: Magnetic reconnection and its manifestations in solar flares and eruptions

Author: Juraj Lörinčík

Department: Astronomical Institute of Charles University

Supervisor: doc.RNDr. Jaroslav Dudík, PhD., Astronomical Institute of the Czech Academy of Sciences

Abstract: Solar flares and eruptions are manifestations of violent releases of magnetic energy from the solar atmosphere. They are powered by magnetic reconnection, a mechanism in which magnetic field lines change their connectivities to reach a lower-energetic state. Theoretical predictions regarding the generalised three-dimensional magnetic reconnection are imposed by the standard flare model in 3D. In this work we present the results of five peer-reviewed publications in which we focused on different predicted aspects of magnetic reconnection in 3D. We analyse evolution and morphology of seven eruptive flares, primarily using observations of the Atmospheric Imaging Assembly onboard the Solar Dynamics Observatory. In the first publication, (Lörinčík et al., 2019a), we interpreted variations of velocities of slipping flare kernels using the mapping norm of field line connectivity simulated via the model. In Lörinčík et al. (2019b) we showed that the observed conversion of filament strands to flare loops is a signature of the ‘ar–rf’ reconnection geometry between erupting flux rope and overlying coronal arcades. In another observation (Dudík, Lörinčík et al. (2019)), all constituents of this geometry were successfully identified together with the constituents of the ‘rr–rf’ geometry between two field lines of the erupting flux rope. Further, the ar–rf reconnection was found to act in a spatial expansion of a core dimming region, in which potential new sources of the solar wind were identified (Lörinčík et al., 2021a). Finally, in Lörinčík et al. (2021b) we found that the ar–rf reconnection geometry leads to a formation of saddle-shaped arcades of flare loops, a newly-discovered phenomenon. These publications provide important observational support for recent theoretical predictions imposed by the standard flare model in 3D. Their results show that numerous flare-related phenomena can naturally be explained in the context of magnetic reconnection in 3D.

Keywords: solar flares, Sun, solar corona, UV and X-ray emission, magnetic reconnection



# Contents

<b>1</b>	<b>Introduction</b>	<b>3</b>
1.1	The Sun . . . . .	3
1.2	Magnetism in the solar atmosphere . . . . .	4
1.2.1	Photosphere . . . . .	4
1.2.2	Chromosphere . . . . .	5
1.2.3	Corona and the heliosphere . . . . .	6
1.3	Magnetohydrodynamic approach to solar plasma . . . . .	7
1.3.1	Basic equations of magnetohydrodynamics . . . . .	8
1.3.2	The two limits of the induction equation . . . . .	8
1.3.3	Magnetic reconnection . . . . .	9
<b>2</b>	<b>Solar flares and eruptions</b>	<b>11</b>
2.1	Basic properties of solar flares . . . . .	11
2.1.1	Classification of solar flares . . . . .	11
2.1.2	Flare loops and flare ribbons . . . . .	12
2.1.3	Eruptive flares . . . . .	13
2.1.3.1	Coronal Mass Ejections . . . . .	13
2.1.3.2	Eruptive flux ropes . . . . .	14
2.1.3.3	Dimming regions . . . . .	15
2.2	Eruption triggering mechanisms . . . . .	15
2.3	Two-dimensional model of solar flares . . . . .	17
<b>3</b>	<b>Magnetic reconnection in three dimensions</b>	<b>21</b>
3.1	Magnetic topology in three dimensions . . . . .	21
3.1.1	Three-dimensional null points . . . . .	21
3.1.2	Quasi-separatrix layers . . . . .	22
3.2	Standard flare model in three dimensions . . . . .	24
3.2.1	Basic properties of the model . . . . .	24
3.2.2	Slipping and slip-running reconnection . . . . .	26
3.2.3	Three-dimensional reconnection geometries . . . . .	29
<b>4</b>	<b>Instruments and data</b>	<b>33</b>
4.1	Solar Dynamics Observatory . . . . .	33
4.1.1	Atmospheric Imaging Assembly . . . . .	33
4.1.1.1	AIA temperature responses . . . . .	33
4.1.1.2	Processing of AIA data . . . . .	34
4.1.2	Helioseismic Magnetic Imager . . . . .	35
4.2	Other instruments . . . . .	36
4.2.1	The X-ray Telescope . . . . .	36
4.2.2	Extreme Ultraviolet Imager . . . . .	36
4.2.3	Large Angle and Spectrometric Coronagraph . . . . .	37
<b>5</b>	<b>Results</b>	<b>39</b>
5.1	Velocities of flare kernels and their relation to QSL properties . . . . .	39
5.2	Conversion of filament strands to flare loops as a manifestation of the ar-rf reconnection geometry . . . . .	55
5.3	Observations of all constituents of the three-dimensional magnetic reconnection geometries . . . . .	68
5.4	Plasma outflows from a core dimming region and their relation to the ar-rf reconnection . . . . .	78
5.5	Saddle-shaped arcades of flare loops . . . . .	95
<b>6</b>	<b>Conclusions</b>	<b>105</b>
6.1	Summary of results . . . . .	105
6.2	Future prospects . . . . .	105
	<b>Bibliography</b>	<b>107</b>
	<b>List of publications</b>	<b>131</b>



# 1. Introduction

## 1.1 The Sun

The Sun is our closest star. It is an important astrophysical object, being a natural laboratory of plasma physics and an essential factor in the habitability of its planetary system. Basic characteristics of the Sun are listed in numerous textbooks (e.g., Stix, 2002; Foukal, 2004; Lang, 2009). The radius of the Sun measures roughly  $6.96 \times 10^8$  m, its mass is around  $1.99 \times 10^{30}$  kg, and its equatorial surface gravity equals  $274 \text{ m s}^{-1}$ . Its age is roughly  $4.6 \times 10^9$  years, which makes it a relatively-young star. The Sun is rich in metals, it belongs to Population I, with average composition of  $X_{\odot} \approx 0.73$ ,  $Y_{\odot} \approx 0.25$ , and the metallicity  $Z_{\odot} \approx 0.01 - 0.02$ . The luminosity of the Sun reaches  $\approx 3.86 \times 10^{26}$  W. The Sun is a main-sequence star of a spectral class G2V. To the first order, the solar spectrum can be approximated by a black-body radiating at 5778 K. This effective temperature leads to the B – V color index of 0.66, which in the Hertzsprung–Russell diagram corresponds to a yellow color.

The source of stellar energy is thermonuclear fusion. The Sun generates the energy by fusing hydrogen into helium via two main processes, the proton-proton chain and the CNO cycle. The nuclear reactions occur in the solar core, where the temperature and pressure are the highest. The solar core extends to roughly 25% of the solar radius, but contains 50% of its mass. The energy generated in the core is consequently transferred outwards in the form of photons. The second innermost layer of the Sun is the radiative zone, characterised by radiative transfer of energy. There, photons are being constantly scattered as they are absorbed and then re-emitted by ionized atoms. Due to the high density of plasma in the solar interior, it can take up to about  $10^6$  years for photons to escape the Sun. At roughly 70% of the solar radius, convective instability sets, carrying the energy via ‘bubbles’ of material rising all the way to the solar surface. The convective motions and the rotation of the Sun cause the solar plasma to exhibit differential rotation above the tachocline, a zone roughly corresponding to the bottom boundary of the convection zone. The differential rotation is characterised by variations of rotational velocities of solar plasma at different depths and latitudes. Since the interior of the Sun cannot be observed, the spatial variations of different properties of solar plasma are subjects to estimates of physical models constrained by observations. These indicate that the temperature in the centre of the core rises up to  $T_0 = 1.57 \times 10^7$  K, the central density is  $\rho_0 = 1.54 \times 10^5 \text{ kg m}^{-3}$ , and the pressure  $P_0 = 2.35 \times 10^{16} \text{ N m}^{-2}$ . While the internal pressure and density drop exponentially, the decrease of the temperature is less steep, close to linear in radiative and convective zones. For example, according to the well-known model ‘S’ of Christensen-Dalsgaard et al. (1996), the temperature at the boundary between the radiative and convective zones is close to 1 MK. An important tool for investigation of the solar interior is helioseismology, a discipline focused on addressing the properties of the solar interior via studying the oscillations of the Sun (Christensen-Dalsgaard, 2002). Global helioseismology helps characterise variations of properties of plasma with depth, its chemical composition, and differential rotation. Local helioseismology provides important information about the convection zone by studying waves propagating to the solar surface.

By far the most important property concerning the convection zone in the context of our study is the generation of the solar magnetic field. The invention of a magnetograph (Babcock, 1953), a device for measuring solar magnetic fields, led to discovery of the solar magnetic field. Its surface line-of-sight intensities vary between  $10^{-1}$  and  $10^3$  G. A dynamo mechanism is thought to be causing the generation of solar magnetic field, based on convective circulation of bulks of conductive plasma. The most prominent manifestation of the solar magnetism is its 11-year cycle which begins (and ends) with a complete reversal of the solar magnetic field. The Babcock’s model of the solar dynamo (Babcock, 1961) initiates with an axisymmetric dipole whose field lines gradually wrap around the Sun because of the differential rotation. This results in intensifying of strength of the magnetic field in individual flux tubes, theoretical cylindrical volumes of constant  $\vec{B}$  parallel to field lines. Under the effect of the buoyancy force, some flux tubes rise above the solar surface, producing magnetic bipoles observed as active regions in the solar atmosphere. During the course of the cycle, active regions appear closer and closer to the equator. There, a portion of the magnetic flux cancels-out with the flux of the opposite polarity, while the remaining magnetic flux concentrations migrate toward the solar poles. At the poles, they progressively replace the magnetic field of the original dipole, until the global field is completely reversed.

## 1.2 Magnetism in the solar atmosphere

In solar active regions, the magnetic field reaches  $10^2 - 10^3$  G in stronger concentrations. Areas outside of active regions are in turn referred to as quiet Sun. Even though quiet Sun is usually associated with weak fields of  $10^0 - 10^1$  G, it still contains most of the total magnetic flux of the photosphere (see e.g., the review of Bellot Rubio and Orozco Suárez, 2019). The appearance of structures associated with active regions and quiet Sun varies across different layers of the solar atmosphere. Traditionally, it is divided into four layers; the photosphere, the chromosphere, the transition region, and the corona. Basic physical properties of these layers are, for example, described in one-dimensional (1D) models of the solar atmosphere. They describe variations of different plasma parameters with height (see Vernazza et al. (1981) as well as Phillips et al. (2008, Section 1.2 therein)). However, in reality, the physical properties of the solar atmosphere vary dramatically at short temporal and spatial scales. The solar atmosphere should not be regarded as a series of individual symmetric shells stacked one atop of another. Instead, its morphology and evolution is intimately related to that of the solar magnetic field. In the following section, manifestations of the magnetic activity in each layer of the solar atmosphere are described. Theoretical description of behaviour of magnetised plasmas is the objective of magnetohydrodynamics, discipline focused on magnetized conductive fluids (Section 1.3).

### 1.2.1 Photosphere

The name of the lowest layer, the photosphere, is derived from Ancient Greek and means ‘the sphere of light’. Indeed, more than 99% of the solar radiation originates in the photosphere, for which its typical temperature roughly equals the solar effective temperature. The photosphere is considered to be the visual surface of the Sun, because at depth equivalent to an optical thickness of  $\tau = 2/3$ , the plasma becomes opaque. The photosphere is only a few hundreds of kilometres thick and has a mass density of roughly  $3 \times 10^{-4} \text{ kg m}^{-3}$ .

The most typical manifestations of the magnetic activity observed at the photosphere are sunspots. During the solar cycle, the number of sunspots visible at the disk changes and serves as a proxy for characterising the phase of the solar cycle. In the simplest case, sunspots appear in pairs, with each spot representing one polarity. However, extensive groups composed of numerous sunspots, hosting complicated magnetic configurations, are sometimes observed. Their diameters range between  $10^1$  and  $10^5$  km, but the sunspots evolve, sometimes rapidly, as well as exhibit proper motions across the disk.

The darkness of sunspots is caused by their relatively-lower temperature compared to the surrounding photosphere, ranging between  $3 - 5 \times 10^3$  K. The drop of temperature is related to the presence of magnetic flux which inhibits effective mass transfer via the convection. Sunspots are composed of two parts. In the relatively-darker umbra located at cores of sunspots, vertical magnetic field lines are present. Field lines observed in the penumbra, relatively-larger, lighter, outer part of sunspot, have inclinations reaching  $80^\circ$  (e.g., Jurčák, 2011). The difference of the intensity between the umbrae and penumbrae is caused by the spatial distribution of magnetic flux. While the magnetic fields within umbra can be 2500 – 3500 G strong, those in penumbrae are usually below 1000 G (see e.g., the review of Solanki et al., 2006). Apart from sunspots, concentrations of magnetic fields reaching a few hundred G are sometimes observed in plages or faculae.

Detailed view of the photosphere outside of active regions reveals granulation. Granules are upper parts of convective cells and their properties bear signatures of the convective transport of plasma to the photosphere. The central part of each granule exhibits upflows of plasma at speeds of  $0.5$  to  $1.5 \text{ km s}^{-1}$ . The boundaries of granules, roughly  $0.3 \text{ Mm}$  wide, show signatures of cooled falling material. The mean lifetimes of granules range between 1 and 20 minutes. Their characteristic diameter is  $1 \text{ Mm}$  (Title et al., 1989). Another signature of the convection is visible in the dynamics of supergranules, bulks of plasma typically  $30 \text{ Mm}$  large (Hagenaar et al., 1997). Supergranules were discovered using measurements of the Doppler velocities of the photospheric plasma. Cores of supergranules reveal upflows of plasma with speeds of  $\approx 30 \text{ m s}^{-1}$ . Consequently, plasma moves horizontally towards boundaries of supergranules at speeds larger by a factor of up to 10, and finally descends.

Granules and supergranules play an important role in the spatial distribution of the photospheric magnetic field. Concentrations of both weak and strong magnetic flux can be found along ‘lanes’ separating supergranules. At large spatial scales, these flux concentrations add-up to the so-called network, sometimes termed supergranulation network. Within individual supergranules, the internetwork, or inner network fields can be recognized. Magnetic flux of the internetwork field by far exceeds that of the network. However, most of this flux is concentrated in tiny magnetic loops closed at low altitudes (De Pontieu, 2002).

## 1.2.2 Chromosphere

The solar photosphere is overlaid by the chromosphere. Its name can be translated as ‘the sphere of color’, and originates in the reddish color of its structure sometimes revealed during solar eclipses. Depending on the atmospheric model, the thickness of the chromosphere reaches typically a few thousand kilometres. The properties of the chromosphere vary with the distance from the surface. Its temperature rises from roughly 3800 K in the temperature minimum to roughly a few tens of thousands of Kelvin at its outer boundary. From the inner to the outer boundary, its mass density drops from  $10^{-4} \text{ kg m}^{-3}$  to  $10^{-11} \text{ kg m}^{-3}$ .

The chromosphere is highly inhomogeneous. Outside of active regions, the morphology of the chromosphere is closely associated with internetwork and network magnetic fields. In the low and middle chromosphere, the chromospheric network can be distinguished. The interiors of supergranules are dominated by small closed loops of the internetwork. Field lines of the network, which emanate from between supergranules, broaden with increasing altitude. These topological features, which are sometimes referred to as canopies, reach out toward the solar corona.

When viewed at the limb, the chromosphere reveals thousands of thin jets of plasma called spicules. Type I spicules have heights of 3 – 4 Mm, lifetimes of 3 to 10 minutes, and ejection speeds ranging between 10 and  $50 \text{ km s}^{-1}$ . Type II spicules are more dynamic, have a shorter lifespan, and are relatively-longer than Type I spicules. The on-disk chromosphere reveals its fine structure composed of dark and elongated fibrils. Long, nearly-horizontal, and long-lived fibrils overlay supergranules. More dynamic, short-living fibrils at edges of supergranules are the on-disk counterparts of Type I spicules. Relatively-fainter fibrils, which exhibit waving motions, are the counterparts of Type II spicules (see e.g., the review of Rutten, 2006).

Observations of the Sun at chromospheric temperatures further reveal solar prominences, clouds of chromospheric plasma lifted to high altitudes between 10 and 100 Mm, where they are embedded in the solar corona (Section 1.2.3). The most extensive prominences are sometimes visible during solar eclipses. The typical temperature of the prominence plasma, of the order of  $10^3 - 10^4 \text{ K}$  (e.g., Labrosse et al., 2010), is however orders of magnitude below that of the corona. Prominences therefore appear in absorption when observed against the coronal EUV radiation or the solar disk. In the latter case, they are referred to as filaments. Filaments are sometimes seen to erupt and escape the Sun. An example of a well-known filament eruption, which occurred on 2012 August 31, is presented in Figure 1.1. The erupting filament is depicted in the chromospheric 304 Å (left) and coronal 193 Å (right) filter channels of the Atmospheric Imaging Assembly (AIA; Lemen et al., 2012, also our Section 4.1.1) onboard the Solar Dynamics Observatory (SDO; Pesnell et al., 2012).

Two principal categories of filaments are distinguished. The first are quiescent filaments which form in regions of quiet Sun. The lengths of quiescent filaments can reach hundreds of Mm. Their thickness is usually of the order of tens of Mm, but depends on the part of spectrum in which they are observed. When viewed in EUV, filaments are typically thicker than those in  $\text{H}\alpha$  (Heinzel et al., 2001) and have extended EUV filament channels (Heinzel et al., 2008; Dudík et al., 2008). Quiescent filaments can be supported in equilibrium for weeks or even months before they eventually erupt. Active region filaments are smaller and their lifetime is shorter than that of both quiescent filaments and active regions in which they form, typically spanning a few days only. Filaments forming at boundaries between quiet Sun and active regions are termed intermediate filaments. The filament plasma is observed to be dynamic, exhibiting both horizontal and vertical motions at speeds of several tens  $\text{km s}^{-1}$ . Further, turbulent motions occurring at relatively-lower speeds, sometimes below the velocity resolution of instrumentation, are recognized (e.g., Schmieder et al., 2000). Filaments are highly structured. Their legs, which can sometimes be traced down to the solar surface (e.g., Schmieder et al., 1991; Lin et al., 2008) are composed of individual ‘threads’ (or ‘strands’) with a typical thickness of several  $10^2 \text{ km}$ . Further, lateral extensions from the main body of filament which do not connect to the solar surface, termed ‘feet’ or ‘barbs’ (e.g., Martin, 1998; Aulanier and Schmieder, 2002), are distinguished.

Filament legs sometimes exhibit rotational motions at speeds up to several tens of  $\text{km s}^{-1}$ , at which they become reminiscent of tornadoes. These phenomena are usually short-lived, lasting up to a few days, and have been interpreted as signatures of supply of plasma to filament along helical field lines (Li et al., 2012; Orozco Suárez et al., 2012). A vast majority of filaments form above polarity inversion lines (PILs), where magnetic field lines are sheared (e.g., Mackay et al., 2008). Magnetic fields in filaments are mostly horizontal (Bommier and Leroy, 1998) composed of field lines containing ‘dips’. Spectro-polarimetric measurements of filamentary magnetic fields reveal fields with typical strengths of the order of  $10^1 \text{ G}$  which increase with height.

First modern concepts on formation of filaments were developed by van Ballegoijen and Martens (1989). They shown that magnetic reconnection (Section 1.3.3) can lead to transfer of magnetic flux

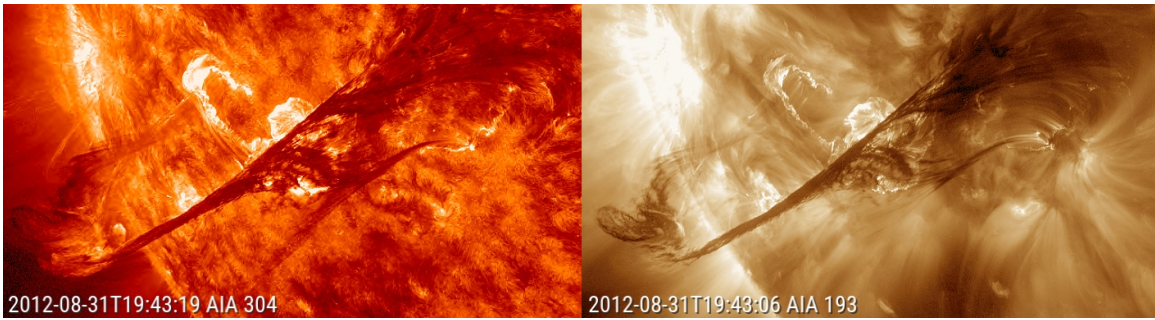


Figure 1.1: Filament eruption from 2012 August 31 in the 304 Å (left) and 193 Å (right) filter channels of SDO/AIA.

from sheared coronal arcade fields to dipped helical fields. In these dips, filamentary plasma can be trapped (see e.g., the review of Mackay et al., 2010). Based on the source of plasma supplied to the dips, two principal categories of mass supplying mechanisms are recognized. The first category describes mechanisms which can cause lifting of plasma from the photosphere and chromosphere (e.g., Litvinenko and Martin, 1999). The second category concerns the condensation of the hot plasma of the solar corona (e.g., Berger et al., 2012).

### 1.2.3 Corona and the heliosphere

At the outer boundary of the chromosphere, the solar transition region is located. At a spatial scale of a few tens of kilometres, the density drops by approximately another two orders of magnitude and, at the same time, the temperature rises from  $\approx 10^4$  K to  $\approx 10^6$  K. Such high temperature is a typical characteristic of the solar corona, a layer of solar plasma extending up to several millions of kilometres from the Sun. The structure of the solar corona was first discovered during solar eclipses. The observations were however possible only for very limited periods of time, later extended with the invention of a coronagraph by B. Lyot in 1931. Another instrument which found a wide usage in studies of the corona was a spectroscope. In the first half of the 20th century, emission lines of numerous elements formed in the corona have been recognized, usually from ions with a high degree of ionisation corresponding to plasma temperatures of  $\approx 10^6$  K. The mechanism heating the corona to such high temperatures is still unknown. Due to this high temperature, plasma of the solar corona is emitting (the ‘E-corona’) mostly in the extreme-ultraviolet (EUV) part of the spectrum and its study is a subject to space-borne observations. Visible-light observations during total solar eclipses can reveal the K-corona, visible due to scattering of sunlight at free electrons. The last source of the coronal radiation comes from the F-corona, created by scattering on dust particles in the interplanetary space.

The strong association between the morphology of the corona and the distribution of the solar magnetic field is clear at the first glance; the plasma of the solar corona follows either closed, arc-shaped, or ‘open’ field lines stretching into the interplanetary space. The most common components of the solar corona are coronal loops. Coronal loops are found in active regions, where they join oppositely-oriented magnetic field concentrations. Cores of active regions are populated by ‘hot’ loops whose temperatures exceed 2 MK (e.g., Warren et al., 2010; Schmelz and Winebarger, 2015). Footpoints of these loops are observed as low-lying coronal moss. Active region cores are usually surrounded by ‘warm’, roughly 1 MK, loops (e.g., Warren et al., 2010). Warm loops at peripheries of active regions sometimes show fan-like morphology (e.g., Ugarte-Urra et al., 2009). The temperature of coronal loops generally depends on the properties of the heating mechanism (e.g., Klimchuk, 2006). The size and spatial distribution of coronal loops is dictated by the magnetic topology of the associated active region.

Despite being much more homogeneous than that of active regions, quiet Sun corona still includes many small-scale and large-scale structures and phenomena. Small-scale structures can easily be related to underlying concentrations of photospheric magnetic flux. These include e.g., EUV or X-ray coronal jets exhibiting signatures of magnetic reconnection (Shimojo et al., 2007), or coronal bright points. Bright points are fibril-like bundles of loops located above strong, but compact concentrations of the photospheric magnetic flux. They are visible in both EUV and soft X-rays. Large-scale structures are represented e.g., by coronal arches or transequatorial loops (Aschwanden, 2005, Section 1.2 therein). The existence of such extensive loops is due to the fact that magnetic field lines stretched away from the surface are still closed, behaving according to Gauss’s law for magnetism (Equation 1.3).

Aside from active regions and quiet Sun, coronal holes are observed. They are dominated by field lines extending far away to the heliosphere and can thus locally be regarded as open. Along these field lines, solar plasma outflows to the interplanetary space in the form of the fast solar wind. Coronal holes are therefore more tenuous, for which they are relatively-darker compared to the corona that surrounds them. Near the minimum of the solar cycle, coronal holes concentrate at the poles of the Sun where they can reside for as long as 7 or 8 years. They can also appear elsewhere on the disk, but their lifespan is much shorter, typically reaching a few weeks. When the solar cycle reaches its maximum, coronal holes disappear, typically for periods of 1 to 2 years (see, for example, the review of Cranmer, 2009).

The solar wind is a continuous stream of plasma into the interplanetary space. It flows along field lines which become spiral as the Sun rotates. The solar wind defines the heliosphere, a volume in space characterised by the pressure of the solar wind dominating the outside pressure of the interstellar medium. The velocities of the fast solar wind originating from coronal holes can reach up to  $800 \text{ km s}^{-1}$  at 1 AU, while the slow solar wind flows at velocities of up to  $400 \text{ km s}^{-1}$ . Sources of the slow solar wind are not yet well established, however, traces of its generation have been observed at edges of active regions (e.g., Sakao et al., 2007) and transient coronal holes (Kahler and Hudson, 2001). The mass losses associated with both the slow and fast components of the solar wind are of the same order of magnitude, roughly  $10^9 \text{ kg s}^{-1}$ .

In the complex magnetic fields of the active region and quiet Sun corona, sudden releases of the energy, manifested as nanoflares, microflares, and ordinary solar flares (Section 2) occur. The frequency  $N$  of these phenomena was found to depend on the released energy  $E$  and is given by a power-law distribution (e.g., Maehara et al., 2015):

$$\frac{dN}{dE} \propto E^{-\alpha}, \quad (1.1)$$

where  $\alpha$  is the slope of the distribution which varies among different types of flares. The weakest, but the most frequent are nanoflares, nowadays widely discussed as possible drivers of the coronal heating (e.g., Klimchuk, 2015). The typical energy budget of nanoflares is only  $10^{24}$  erg, which makes them difficult to resolve. Nanoflares are usually associated with transient, localised brightenings in the EUV and X-ray parts of the spectrum. The value of  $\alpha$  for nanoflares is 1.79 (e.g., Aschwanden et al., 2000). The frequency of occurrence of average-energy nanoflares is higher by roughly 4 – 10 orders of magnitude compared to average microflares and flares. Microflares are much easier to observe than nanoflares, e.g., during coronal jets or in active regions. Microflares exhibit energies of  $\approx 10^{27}$  erg and the slope of their distribution follows  $\alpha = 1.74$  (Shimizu, 1995). Finally, the most energetic and violent manifestations of the solar magnetism are solar flares. The amount of energy released during flares usually exceeds  $10^{28}$  erg and their distribution is given by  $\alpha = 1.53$  (Crosby et al., 1993).

### 1.3 Magnetohydrodynamic approach to solar plasma

The Sun is a gaseous object. Due to the high temperatures, the atoms are partially or completely ionized. The same property applies to the solar atmosphere. While, for example, the photosphere is ionized only partially, the matter in the corona is in a state of a nearly complete ionisation. The ionised gases of the Sun satisfy the conditions necessary for matter to be considered plasma:

1. The system is quasi-neutral. At large distances, a bulk of plasma appears to be neutral and possible inhomogeneities in the distribution of charges are negligible.
2. The system exhibits a collective behaviour. The number of charged particles in the system is  $\gg 1$ , ensuring that charge of each individual particle is shielded by the neighbouring particles.
3. The frequency of oscillations of charged particles is higher than their collisional frequency. The electromagnetic force in plasma dominates over other forces.

Solar plasma is composed of a large number of particles. This claim holds even in the solar corona, where the electron number densities  $N_e$  still typically exceed  $> 10^8 \text{ cm}^{-3}$ . An effective method for treating plasma is via fluid dynamics, which characterises motions of a bulk of plasma as a fluid, behaving under the effect of various internal and external forces. Since plasma is composed of charged particles, the electromagnetic (Lorentz) force plays a prominent part in its physics. The basic laws of magnetohydrodynamics (hereinafter ‘MHD’) must therefore fulfil the Maxwell equations. In their differential forms, the Maxwell equations read

$$\epsilon_0 \vec{\nabla} \cdot \vec{E} = n_i q_i + n_e q_e, \quad (1.2)$$

$$\vec{\nabla} \cdot \vec{B} = 0, \quad (1.3)$$

$$\vec{\nabla} \times \vec{E} = -\frac{\partial \vec{B}}{\partial t}, \quad (1.4)$$

$$\frac{1}{\mu_0} \vec{\nabla} \times \vec{B} = n_i q_i \vec{u}_i + n_e q_e \vec{u}_e + \epsilon_0 \frac{\partial \vec{E}}{\partial t}, \quad (1.5)$$

where  $\vec{B}$  and  $\vec{E}$  are the electric and magnetic fields, respectively. Further,  $n$  stands for the concentration of charges  $q$  which move at the velocity  $\vec{u}$  and  $t$  is time. Finally,  $\mu_0$  and  $\epsilon_0$  is the magnetic permeability and permittivity of vacuum, respectively, whose values are close to those of astrophysical plasmas (Aschwanden, 2005, Section 5.1.1 therein).

### 1.3.1 Basic equations of magnetohydrodynamics

Basic equations of magnetohydrodynamics are derived assuming the plasma approximation. Their simplest form further involves a single-fluid approximation, where terms describing properties of ions and electrons are linearly combined. The basic MHD equations (e.g., Section 2.4 of Priest, 2014) consist of the equation of motion (Eq. 1.6), the continuity equation (Eq. 1.7), the equation of state for ideal gas (Eq. 1.8), and the energy equation (Eq. 1.9)

$$\rho \frac{d\vec{u}}{dt} = \vec{j} \times \vec{B} - \nabla p + \vec{F} \quad (1.6)$$

$$\frac{d\rho}{dt} + \rho \vec{\nabla} \cdot \vec{u} = 0 \quad (1.7)$$

$$p = \frac{k_B}{m} \rho T \quad (1.8)$$

$$\frac{\rho^\gamma}{\gamma - 1} \frac{d}{dt} \left( \frac{p}{\rho^\gamma} \right) = -\vec{\nabla} \cdot \vec{q} - L_r + j^2 / \sigma + F_H \quad (1.9)$$

The equations of continuity and motion (1.6, 1.7) include additional quantities such as  $\rho$  and  $\vec{j}$ , the charge and current density, respectively, and the general force term  $\vec{F}$ . In textbooks, it is sometimes replaced by the gravitational force  $\vec{F} = \rho \vec{g}$ . The energy equation (1.9) is rather complicated, as the form we list accounts for all of the most important energy balance mechanisms in solar plasma. The first term on the right-hand side stands for the thermal conduction introduced via the heat flux vector  $\vec{q}$  and the second term stands for the radiative losses  $L_r$ . The fourth term,  $F_H$ , combines the heating generated by viscous dissipation with additional chromospheric or coronal heating. Finally,  $k_B$  is the Boltzmann constant,  $\gamma$  the adiabatic coefficient, and  $\sigma$  the electrical conductivity. The MHD equations are sometimes accompanied by Ohm's law, which is for ideal plasma (or ideal MHD) expressed as

$$\vec{E} + \vec{u} \times \vec{B} = 0. \quad (1.10)$$

Non-ideal effects are, in the simplest case, introduced by including the resistivity  $\eta$ :

$$\vec{E} + \vec{u} \times \vec{B} = \frac{\vec{j}}{\sigma} = \vec{j} \eta, \quad (1.11)$$

or by replacing the right-hand side of the equation with a general non-ideal term  $\vec{N} \neq 0$ .

### 1.3.2 The two limits of the induction equation

We finally complete the set of MHD equations by the induction equation. Maxwell equations and Ohm's law can easily be combined to recover the induction equation which relates the magnetic field strength with plasma velocity and magnetic diffusivity  $\xi = 1/(\mu_0 \sigma)$  as

$$\frac{\partial \vec{B}}{\partial t} = \vec{\nabla} \times (\vec{u} \times \vec{B}) + \xi \nabla^2 \vec{B}. \quad (1.12)$$

Depending on how conductive studied plasma is, either the first or the second term on the right-hand side can be neglected. For a collisional, fully ionised plasma the electric conductivity can be expressed using the Spitzer's formula (Section 1.2.2 in Priest and Forbes, 2000)

$$\sigma = 1.53 \times 10^{-2} \frac{T^{3/2}}{\ln \Lambda}. \quad (1.13)$$

Analogically, the magnetic diffusivity then reads

$$\xi = 5.2 \times 10^7 \frac{\ln \Lambda}{T^{3/2}}, \quad (1.14)$$

where  $\ln \Lambda$  is the Coulomb logarithm describing elastic collisions between charged particles. Its values depend on plasma temperature and density and are tabulated (see e.g., Table 2.1 in Priest, 2014).

Since  $\sigma \propto T^{3/2}$ , for sufficiently high temperatures plasma becomes fully conductive, at which  $\xi \rightarrow 0$ . Equation 1.12 then transforms to its ideal limit

$$\frac{\partial \vec{B}}{\partial t} = \vec{\nabla} \times (\vec{u} \times \vec{B}). \quad (1.15)$$

and Ohm's law to its ideal form (Equation 1.10). As such, Equation 1.15 implies that the time-evolution of the magnetic field is given only by the term on the right-hand side of Equation 1.15, i.e., it is given by the rotation of the plasma velocity field. The magnetic fields do not diffuse in plasma, meaning that the magnetic flux as well as field lines are conserved. In the ideal limit, plasma is frozen-in to the magnetic field lines, which is thought to be the case for example in coronal loops (Section 1.2.3) in which plasma follows the field lines.

The second limit is the non-ideal diffusive limit, in which the induction equation transforms to

$$\frac{\partial \vec{B}}{\partial t} = \xi \nabla^2 \vec{B}. \quad (1.16)$$

This simple diffusion equation means that the time-variation of the magnetic field is given only by its diffusion. This limit is important when the magnetic Reynolds number  $R_m = (l_0 v_0)/\xi$ , in which  $l_0$  and  $v_0$  is the spatial scale and velocity of plasma, is  $\ll 1$ . The lowest values of  $R_m$  can be found in very thin diffusion regions. These lead to development of current sheets, layers in which electric currents can be compressed to  $l_0$  of one kilometre or even less.

### 1.3.3 Magnetic reconnection

Perhaps the most prominent example of a non-ideal process occurring in small-scale diffusion regions is magnetic reconnection. Magnetic reconnection is a process in which field lines change their connectivity. As a result, the lines, or the magnetic topology with which they are associated, are rearranged to a state of a lower energy.

This phenomenon has first been considered by Dungey (1953), who suggested that strong Ohmic currents can 'destroy' magnetic flux close to a neutral line. Principal aspects of magnetic reconnection were elaborated and the term itself was coined by Parker (1957) and Sweet (1958). In their analytical model, the current sheet forms between magnetic field lines of opposite orientation, which are carried to the current sheet by motions of conductive fluids. In regions where the magnetic diffusivity is non-zero, the fields reconnect and are carried away by reconnection outflows. The Sweet-Parker model helped postulate key predictions on behaviour of reconnecting field lines. This was essential for addressing the physical mechanism causing solar flares, which were observed at visible and radio wavelengths at the time. The bursty nature of these phenomena, found in the solar atmosphere, has quickly been associated with abrupt releases of the magnetic energy by annihilation of field lines (e.g., Parker, 1963).

The Sweet-Parker model shown that a half of the magnetic energy inflowing to the reconnection region is converted to the kinetic energy and the other half to the thermal energy. The authors defined the reconnection rate, a ratio between the velocity of plasma inflowing to the reconnection rate and outflowing from it. Magnitude of the derived reconnection rate was however too small to reflect the observations of solar flares. A solution to this problem was subsequently proposed in the Petschek's model (Petschek, 1964). It was based on a thinner diffusion region, to which field lines are carried via standing MHD waves. The derived reconnection rate was substantially higher, allowing for releases of energy needed to power flares at timescales as small as  $10^2$  seconds, which was substantially closer to observations. This finding vindicated how important magnetic reconnection is, for which it has become the center of attention of many physicists for decades to come. As we will however demonstrate in Section 3 and with our own observational analyses, the reconnection mechanism has proven to be substantially more complicated than initially thought.



# 2. Solar flares and eruptions

## 2.1 Basic properties of solar flares

Solar flares are sudden brightenings in the solar atmosphere. They are among the most energetic phenomena occurring in the solar system. The total energy released during flares ranges between  $10^{28}$  and  $10^{32}$  erg (e.g., Schrijver et al., 2012). Solar flares are consequences of sometimes complex evolution of photospheric magnetic flux and related magnetic reconnection occurring in the solar corona (Section 1.3.3). Signatures of solar flares can be observed in the entire electromagnetic spectrum, from microwaves to high-energy gamma rays (see e.g., Fletcher et al., 2011).

The first report on observations of solar flare was provided by British astronomer R. Carrington. His publication (Carrington, 1859) describes, how “two patches of intensively bright and white light broke out” from a group of sunspots he just finished to draw. According to Carrington’s drawings, in the course of the following 5 minutes, these patches “traversed a space of about 35 000 miles” across the solar surface. At night of the following day, aurorae as well as failures of telegraphic network were reported, signatures of a powerful geomagnetic storm. While observations of flares visible at optical wavelengths were generally considered rare (see e.g., Švestka, 1966), ‘The Carrington event’ was particularly strong, sometimes regarded as the largest solar flare in the last 500 years. This claim is supported by the long duration of the white-light emission associated with the flare, most-likely produced as a result of unusually strong heating of the chromosphere (Section 2.1.2). Even though comparisons between the Carrington event and flares observed in the era of modern measurements are difficult, we will still revisit this important observation in Section 5.1. Over the decades, the study of flares has become a subject to observations primarily carried out at UV, EUV, and X-ray wavelengths, where most of the flare emission originates. As such, flares reveal their complex nature involving not only the white-light signatures above the photosphere, but distinct morphological features in all layers of the solar atmosphere.

### 2.1.1 Classification of solar flares

Solar flares can be divided into confined and eruptive flares (e.g., Magara et al., 1996). Confined flares, sometimes called compact or impulsive flares (Section 2.3 in Shibata and Magara, 2011) do not lead to ejections of solar plasma. Such events can however still be energetic, as confined X-class flares have already been observed (e.g., Thalmann et al., 2015). The second category concerns eruptive flares, characterised by eruptions of plasma from the Sun, which we focus on in this work (Section 2.1.3).

A widely-used classification of solar flares is based on measurements of the X-ray flux provided by the Geostationary Operational Environmental Satellite (GOES). The X-ray flux at the Earth varies in time, typically between  $10^{-8}$  and  $10^{-4}$  W m<sup>2</sup>, with peaks representing and caused by solar flares. According to the peak value, five different classes of flares are distinguished; A, B, C, M, and X, where each class represents a 10-fold increase of the released energy, with X  $> 10^{-4}$  W m<sup>-2</sup> as the strongest class. The total number of solar flares per year follows the progression of the 11-year cycle of the solar magnetic activity. For example, during the peak of the Solar cycle 23, which occurred between 2000 and 2002, more than 7000 flares have been recorded. Out of these, more than 6600 flares were of class C, a few hundred of class M, and only 50 reached out to the class X. During the same cycle on November 4 2003, the strongest flare ever recorded was observed. It was of class X28 (Tsurutani et al., 2005), however, as the flare was partially occulted by the solar limb, it was later hypothesised that its class could have been as high as X45. On the other hand, in the whole year 2008 which corresponded to the solar minimum, only 8 C-class flares occurred.

The characteristics of the energy release associated with the X-ray lightcurves are unique for each flare. Their lightcurves however follow a common pattern, which serves as a basis for recognition of the main phases of flares. The first phase is the impulsive phase. At a timescale of minutes or tens of minutes, the X-ray flux rapidly increases. After the flux reaches its maximum during the peak phase, the lightcurve starts to progressively drop to the pre-flare levels. This occurs while the flare is in its gradual phase, which lasts between several tens of minutes up to a few hours (e.g., Hara et al., 2008), depending on the size of the event. While the lifetime of some flares spans between minutes or tens of minutes, there are also long-duration events (LDE), which can last for several hours or even tens of hours. Note that some flares also exhibit a ‘precursor’ or ‘pre-flare’ phase (Chifor et al., 2007), characterized by a small peak of X-ray flux preceding the main flare.

## 2.1.2 Flare loops and flare ribbons

The X-ray emission measured by instruments such as GOES originates in flare loops which develop during impulsive phases of flares as a consequence of magnetic reconnection. Flare loops were first observed at temperatures exceeding 10 MK (Doschek et al., 1979; Feldman et al., 1980a), corresponding to the soft-X ray part of the spectrum, for which they used to be referred to as soft X-ray loops (e.g., Tsuneta, 1995; Shibata et al., 1995; Tsuneta, 1996). Flare loops usually compose extensive arcades which are developing above PILs (e.g., Isobe et al., 2002). Later instrumentation, in particular SDO/AIA, shown that flare loops are also visible in filters sensitive to emission of the EUV part of the spectrum, such as the 94 Å or 131 Å channels (O’Dwyer et al., 2010, see also Section 4.1.1).

As the flare progresses, flare loops undergo cooling due to radiation and thermal conduction to the chromosphere (e.g., Cargill et al., 1995). Their temperatures progressively drop from several tens of MK down to  $10^4 - 10^5$  K at which point they become visible in lines formed in the chromosphere and the transition region (e.g., Heinzel et al., 1992; van Driel-Gesztelyi et al., 1997). Flare loops visible e.g., in the chromospheric H $\alpha$  line are sometimes referred to as ‘post-flare loops’ (Bruzek, 1964; Švestka, 1989). Švestka (2007) however stressed out that this term is a misnomer. This is because magnetic reconnection and the related transformation from pre- to post-eruptive magnetic configuration does not occur instantaneously. As indicated by durations of the impulsive phases, it usually takes a few minutes or tens of minutes until flare arcade is fully formed. The formation of flare loops can however also continue well into the gradual phase of flare. In that period, the site of reconnection moves from lower to higher altitudes, indicating that extended regions of the solar corona can be affected by this process. An observational signature of this process is the formation of flare loops which are getting higher as the time goes by during the flare (Forbes and Malherbe, 1986; Schmieder et al., 1995). At the same time, the flare loops which formed at earlier times begin to cool down and flare arcades start to be visible at lower temperatures. However, since the newly-appeared flare loops radiate at high temperatures, flare arcades become multithermal (e.g., Schmelz et al., 2011), with contributions from individual flare loops of different temperatures. Multithermal arcades of flare loops are routinely observed by AIA (see e.g., Reeves and Golub, 2011; Warren et al., 2011b; Petkaki et al., 2012, as well as our Section 5.5).

Excellent tracers of magnetic reconnection, vindicating how long can this mechanism act during flares, are sources of the hard X-ray (HXR) radiation. They originate due to bremsstrahlung of thermal and non-thermal (accelerated) particles (Brown, 1971). It was shown (Vasyliunas, 1975) and has been widely-accepted ever since (e.g., Krucker et al., 2010), that the source of the non-thermal particles is magnetic reconnection. Two main categories of compact sources of the HXR radiation related to flare loops are recognized (e.g., Somov and Kosugi, 1997; Tsuneta and Naito, 1998; Gallagher et al., 2002; Tomczak and Ciborski, 2007; Hannah and Kontar, 2011). The first are the looptop sources occurring at apexes of flare loops. In some events, sources were also found above apexes of flare loops, where they are referred to as the above-the-looptop sources (Krucker and Battaglia, 2014; Oka et al., 2015). The second are the footpoints sources, which typically occur in pairs and correspond to anchorings of flare loops. Strong footpoint sources are closely related with white-light emission (Hudson, 1972). While the footpoint sources are usually associated with impulsive phases of flares (Section 2.2 in Krucker et al., 2008), the loop-top sources have been reported even during the gradual phase (e.g., Cliver et al., 1986).

The footpoints sources are signatures of ‘precipitation’ of particles to the lower atmosphere (Kane and Donnelly, 1971; Hudson et al., 1994; Fletcher and Hudson, 2001). As a consequence, the chromosphere and the transition region are rapidly heated, producing footpoints of flare arcades observed as bright, narrow, and elongated structures termed flare ribbons. Ribbons were first studied using the H $\alpha$  line observations (Heyvaerts et al., 1977) routinely obtained by ground-based telescopes. Later, ribbons became frequently observed in the ultraviolet 1600 Å channel of the Transition Region and Coronal Explorer (TRACE; Handy et al., 1999). This channel contained emission of resonance lines of C IV at 1548 Å and 1550 Å forming in the solar transition region at  $\log(T \text{ [K]}) \approx 5$ . The emission of flare ribbons can present valuable information about magnetic reconnection occurring in the corona (e.g., Falchi et al., 1997; Qiu et al., 2002, and Section 5). Flare ribbons are typically observed in pairs and, just as flare arcades below which they appear, develop along PILs. Some flares can lead to the formation of so-called secondary ribbons. Secondary ribbons are usually fainter and persist for shorter periods than the main ones (e.g., Zhang et al., 2014; Li et al., 2017). In another category of flares, circular (e.g., Masson et al., 2017; Liu et al., 2020, Section 3.1.1) or semi-circular (e.g., Zheng et al., 2015; Lim et al., 2017) ribbons can form.

Flare ribbons often exhibit a *J*-like morphology. The curved extremities of ribbons, referred to as ribbon hooks, are typically located further away from PILs and encircle footpoints of erupting structures (Chandra et al., 2009, and Section 3.1.2). When ribbons are viewed at sufficiently high

spatial resolution, their fine structure is revealed. Ribbons are composed of thousands of individual flare kernels, whose characteristic size can be as small as 100 km (Sharykin and Kosovichev, 2014; Sobotka et al., 2016). Flare kernels correspond to locations in which the energy was deposited by the reconnection along newly-formed field lines (see Section 2 in Lin et al., 2003, and references therein). Flare kernels are often observed at footpoints of flare loops. Their understanding progressed in the era of TRACE, which possessed high spatial and temporal resolutions (e.g., Metcalf et al., 2003; Berlicki et al., 2004; Fletcher et al., 2004; Li et al., 2005). Flare ribbons and kernels are nowadays studied mostly in data from the 1600 Å channel of AIA as well as slit-jaw images produced in chromospheric and transition region lines observed by the Interface Region Imaging Spectrometer (IRIS; De Pontieu et al., 2014).

As newly-reconnected field lines appear, flare ribbons start to exhibit apparent motions with respect to PILs. The motion occurring in the direction perpendicular to PILs is referred to as the ribbon separation (Švestka and Cliver, 1992). This motion is a signature of formation of progressively-higher flare loops in a flare loop arcade, leading to an increase of distance between footpoints of flare loops. The ribbon separation typically occurs at velocities of around  $20 \text{ km s}^{-1}$  (e.g., Qiu et al., 2002; Li and Zhang, 2009). However, motions *parallel* to PILs also exist, manifested as the elongation of ribbons (Qiu et al., 2017) as well as propagation of individual kernels (Berlicki et al., 2004; Tripathi et al., 2006). The main difference between these two processes is in timing of their occurrence during flares. While the elongation leads to the formation of ribbons during the impulsive phases of flares, the propagation takes place only along pre-existing ribbons. Further, the elongation is usually a substantially more dynamic phenomenon. While flare kernels typically propagate at velocities reaching tens of kilometres per second (e.g., Fletcher et al., 2004; Li and Zhang, 2009), the elongation can be faster even by an order of magnitude (e.g., Li et al., 2018; Joshi et al., 2019). Note that both phenomena, the elongation of ribbons and propagation of kernels along PILs, can be interpreted in the context of the slipping reconnection, which is a three-dimensional generalisation of magnetic reconnection (Section 3). A key signature of the slipping reconnection is a continuous motion of kernels along the ribbons (Dudík et al., 2014, 2016), which occurs due to a sequential change of connectivity affecting neighboring field lines (Section 3.2.2).

Flare kernels are sometimes investigated in relation to footpoints sources of HXR radiation. Study of HXR kernels often used to be a subject of combined observations from Reuven Ramaty High Energy Solar Spectroscopic Imager (RHESSI; Lin et al., 2002) and TRACE (e.g., Warren and Warshall, 2001; Fletcher and Hudson, 2002; Bogachev et al., 2005; Hudson et al., 2006). Even though the HXR sources are larger than ‘ordinary’ flare kernels (Schmahl and Hurford, 2002), their dynamics can still be related to that of flare kernels (Asai et al., 2002; Qiu et al., 2010; Cheng et al., 2012; Inglis and Gilbert, 2013). An interesting property of motion of kernels observed in HXR and UV was discovered in a statistical study of Yang et al. (2009). The authors found that impulsive phases of flares are characterised by kernel motion along PILs. On the other hand, motions perpendicular to PILs dominate the peak and gradual phases of flares. The dynamics of individual kernels is consistent with that of ribbons they compose as a whole.

## 2.1.3 Eruptive flares

### 2.1.3.1 Coronal Mass Ejections

During eruptive flares, solar plasma is ejected to the interplanetary space in spectacular phenomena known as coronal mass ejections (CMEs; e.g., Webb et al., 2000). CMEs expand in the heliosphere as magnetic clouds (Webb et al., 2000), sometimes termed interplanetary CMEs (e.g., Démoulin, 2008), where they present disturbances in the solar wind. When ejected toward the Earth, they can potentially lead to strong variations of its magnetic field called the geomagnetic storms. CMEs can also lead to acceleration of electrons and ions to energies exceeding 1000 MeV, which are detected during solar energetic particle (SEP) events (e.g., Reames, 1999; Gopalswamy et al., 2004). The task of predicting CMEs is among key aspects of forecasting of the space weather.

Since the beginning of the era of space-borne observations of the Sun, more than ten thousand CMEs have been detected. CMEs are listed in catalogues, for example the one based on observations of the Large Angle and Spectrometric Coronagraph (LASCO, see Section 4.2.3) onboard the Solar and Heliospheric Observatory (SOHO). Their principal properties include e.g., the speeds of ejection, masses, and kinetic energies. The values of these quantities were, in statistical studies, found to be distributed over 2 – 3 orders of magnitude (see Webb and Howard, 2012, and references therein). The mean values of the ejection speed are of the order of  $10^2 \text{ km s}^{-1}$ , their mean masses are  $\approx 10^{15} \text{ g}$ , and the associated kinetic energies roughly  $10^{30} \text{ erg}$ . A typical angular extent of CMEs observed by LASCO is  $47^\circ$ . When a CME occurs within a few degrees of the centre of the disk and is directed

toward the Earth (or away from it) it can be visible as an extensive halo surrounding the whole occulter of coronagraph. Such CMEs are termed halo CMEs (e.g., Gopalswamy et al., 2010).

Illing and Hundhausen (1985) were among the first to distinguish a three-part structure of CME, consisting of

1. leading edge or a frontal loop, corresponding to the outer boundary of CME,
2. cavity or coronal void, a relatively-darker cloud which lack of emission in both white-light and EUV has been related to low density (Chen et al., 2000),
3. and their bright core, typically associated with erupting prominences (Webb and Hundhausen, 1987).

A majority of CMEs occur during the strongest X-class flares (Wang and Zhang, 2007). On the other hand, only  $\approx 20\%$  of C-class flares exhibited a CME (Yashiro et al., 2005). Of a particular interest are ‘stealth’ CMEs, which seemingly cannot be related to a flaring activity on the surface (e.g., McAllister et al., 1996). Stealth CMEs occur when they are erupted from behind the solar limb, outside of the field of view of operating missions, or when the X-ray emission of the respective flare is below the sensitivity threshold of the detectors (see also Section 5.4).

Statistical study of Zhou et al. (2003), involving both imaging data from the EUV Imaging Telescope (EIT) onboard the SOHO spacecraft and LASCO, shown that about 79% of CMEs were associated with active regions. CMEs often originate from pre-existing coronal streamers which overlay active regions. Their helmet- or cusp-shaped morphology is given by open field lines which guide outflows of the solar wind into the heliosphere. Coronal streamers have been evidenced to grow in size for up to a few days before a ‘CME blowout’ occurs (Hundhausen, 1993). Well-known sources of CMEs are sigmoidal active regions. The *S*-like shape of the sigmoid itself is best visible in soft X-rays (e.g., Canfield et al., 1999; Glover et al., 2001). Sigmoids form in highly sheared, non-potential magnetic field. The morphology they exhibit was related to coronal loops organised in two conjugate arcades, arranged in *J* and inverse-*J* patterns. Between the arcades, a topological feature termed bald-patch separatrix can be found (Section 3.1.1). The magnetic configuration of bald-patches can easily lead to magnetic reconnection (McKenzie and Canfield, 2008). Sigmoids, often associated with high flaring activity, thus became an important objective of modelling of solar flares, eruptions, and mechanisms which trigger them (Section 2.2, 3.2.1).

### 2.1.3.2 Eruptive flux ropes

The results obtained using the latest instrumentation challenge the widely-accepted associations between CMEs and eruptions of filaments. The statistical study of Howard et al. (2017) shown that neither the composition, nor the geometry of cores of CMEs they analysed correspond to those of filaments. Out of 42 CMEs, only two had a filamentary counterpart erupting from the Sun. Instead, the authors state that the cores of CMEs are complex magnetic structures composed of numerous twisted field lines called flux ropes.

Theoretical concepts of flux ropes have initially been developed in analytical models of eruptions in 3D (Démoulin et al., 1996b). For example, in the work of Titov and Démoulin (1999), the flux rope is represented by a twisted flux tube which rises above the photosphere and eventually erupts, driving formation of current layers in which the magnetic energy dissipates due to magnetic reconnection. This concept found a wide usage in modelling of eruptions and related mechanisms in 3D (e.g., Török and Kliem, 2003, 2005; Kliem and Török, 2006; Török and Kliem, 2007). As we will further describe in Sections 2.2 and 3, substantial portions of flux ropes can be built only after the onset of flare itself or its precursor. Magnetic reconnection has an important role in their formation, as it further produces long, helical (twisted) field lines wrapping around flux rope as it erupts.

According to statistical studies focused at the occurrence of flux ropes in eruptive solar flares, flux ropes are the dominant cause of eruptions. In a sample of 2403 CMEs imaged by LASCO, STEREO, and SDO, analysed by Vourlidis et al. (2013), at least 40% of the eruptions exhibited an easily-identifiable flux rope. In the study of Nindos et al. (2015), focusing on 141 M- and X-class flares observed by SDO, 45 hot flux ropes were identified. The authors distinguished between confined and eruptive flares and found that nearly a half of the analysed eruptive flares involved a hot flux rope.

The process of flux rope formation is consistent with the spatial and temporal evolution of sigmoids observed in X-rays, which are well reproduced by 3D MHD simulations (Archontis et al., 2009; Savcheva et al., 2012). In the last decade, observations of hot flux ropes became available, owing to the high resolution and temperature sensitivity of recent instrumentation (e.g., Li and Zhang, 2015b; Huang et al., 2016; James et al., 2017; Yan et al., 2018; Wang and Liu, 2019). Observations carried out in the 94 Å and 131 Å channels of AIA sometimes reveal bundles of erupting twisted loops visible

at flaring temperatures. Such flux ropes were termed hot channels (Zhang et al., 2012; Cheng et al., 2013). The available observational studies suggest that hot channels form due to magnetic reconnection during the precursor events, in some cases only minutes before they erupt (see also Wang et al., 2018; Hernandez-Perez et al., 2019).

### 2.1.3.3 Dimming regions

The existence of eruptive flux ropes is also manifested in the form of dimming regions, structures forming in regions from which flux ropes erupted. Coronal dimmings are dark regions often observed after eruptive flares in soft X-rays (e.g., Hudson et al., 1996) or EUV (e.g., Thompson et al., 1998). These structures are also sometimes referred to as 'transient coronal holes', based on their similarity with ordinary coronal holes (Kahler and Hudson, 2001). They are however smaller and observed at shorter periods, typically spanning a few hours or days only. Based on their origin, two categories of dimming regions are recognized. The first are core dimmings, or twin dimmings since they usually occur in pairs. Core dimmings form at opposite ends of PILs and correspond to the legs of the erupting structure (Sterling and Hudson, 1997). Therefore, they are sometimes seen to be encircled by hooked extremities of *J*-shaped flare ribbons (e.g., Veronig et al., 2019). Secondary dimmings occur further away from PILs. They are however still closely associated to flares, as they form at footpoints of field lines associated with flux rope (or reconnecting with it) which are dragged away during its eruption (Mandrini et al., 2007).

The appearance of dimming regions is caused by the depletion of plasma from the corona which escapes along expanding (opening) field lines of CME (Thompson et al., 2000). Amount of mass lost from dimming regions can be as high as that contained in CMEs (see Howard and Harrison, 2004, and references therein). As evidenced by observations of density drops in dimming regions (Vanninathan et al., 2018), this escape occurs during first tens of minutes after the eruption. Afterwards, dimming regions start to shrink until the local solar corona returns to its pre-eruptive state. A possible mechanism driving the recovery of dimming regions is the interchange reconnection (Fisk and Schwadron, 2001, e.g.) between open field lines rooted in dimmings and low-lying closed loops of the surrounding corona (Attrill et al., 2008).

The first evidence for the depletion of plasma from dimming regions was provided in a spectroscopic study of Harra and Sterling (2001). They found that coronal and transition region lines are blueshifted, with Doppler velocities of 30 and 100 km s<sup>-1</sup>, respectively. Outflows (upflows) of plasma with similar velocities, which these blueshifts are signatures of, have been reported in numerous spectroscopic studies reported later on (e.g., Harra et al., 2007; Imada et al., 2007; Miklenic et al., 2011). Analyses of spatial distribution of outflow velocities revealed that the strongest outflows are typically found at footpoints of coronal loops rooted in dimmings (Attrill et al., 2010) or at the edges of dimmings (Veronig et al., 2019). In some cases, the lifetime of these outflows was found to exceed the duration of the eruption itself (Harra et al., 2007; Attrill et al., 2010). Such long-lasting outflows have been suggested to be signatures of solar wind, which is in line with earlier thoughts on dimming regions as possible sources of the solar wind (Rust, 1983; Kahler and Hudson, 2001). Our own analysis aimed at development of the solar wind from core dimming region is presented in Section 5.4.

## 2.2 Eruption triggering mechanisms

The close associations between flares, eruptions, and CMEs led to development of a unified approach, describing them all as manifestations of the same process, with release of the magnetic energy by reconnection at its centre (e.g., Harrison, 1995; Švestka, 2001). Theoretical concepts of mechanisms leading to eruptive flares are briefly outlined in the following sections.

Recent observational and numerical studies show that some flux ropes are still being built even after the onset of the precursor phase. On the other hand, filaments are usually observed for days or even weeks prior to their eruption in an equilibrium, supported by overlying field lines sometimes termed the magnetic cage (e.g., Amari et al., 2018). Whether the equilibrium remains unperturbed or is disrupted depends on a presence of an effective triggering mechanism (e.g., Chen, 2011; Schmieder and Aulanier, 2012) which would disrupt the overlying field and lead to the eruption. These mechanisms may already be at work during preflare activity, usually manifested as brightenings observed in different part of the flaring region throughout the electromagnetic spectrum (e.g., Dere et al., 1997; Fárník and Savy, 1998; Warren and Warshall, 2001; Holman et al., 2003; Chifor et al., 2006).

Mechanisms leading to initiation of an eruption involve either reconfiguration of magnetic fields above and/or below the magnetic flux rope, or MHD instabilities (see e.g., Chifor et al., 2007; Dudík et al., 2016). The former are based on a release of free magnetic energy stored in sheared low-lying

field lines above PILs, which show strong deviations from the potential state (Antiochos, 1998; Moore et al., 2001). Relations between sheared bundles of field lines and flaring activity are well established (e.g., Hagyard et al., 1984; Kusano et al., 2004). We note that the shearing motions are an important ingredient in 3D models of solar eruptions (Section 3.2).

The first mechanism we describe is the tether-cutting reconnection (Moore and Roumeliotis, 1992). The tether-cutting reconnection was first described in a simple magnetic configuration containing a bipolar active region. Above the PIL, strongly-sheared ‘core’ field lines can be found, composing for example, a sigmoid (Moore et al., 2001), which is embedded in an overlying coronal arcade which is less sheared. When the sheared core loses equilibrium, it starts to rise and field lines of the stretched, overlying field converge to the vacated space from which the core rose. There, a current sheet is formed and the field lines of the overlying arcade start to reconnect, further loosing the ties (untethering) imposed on the rising core. Note that some aspects of the tether-cutting reconnection can be interpreted in terms of the theory of flux cancellation at PILs (van Ballegoijen and Martens, 1989; Amari et al., 2003; Linker et al., 2003). It has been suggested that the flux cancellation itself occurs via slow tether-cutting reconnection (Moore and Roumeliotis, 1992) and can be its observational consequence.

Tether-cutting can also occur above the sheared core, where it is termed as the external tether-cutting or magnetic breakout. In the model of Antiochos (1998), containing a quadrupolar magnetic configuration, the sheared core appears again along the PIL. It is held down in equilibrium by overlying field lines which are not sheared. When magnetic reconnection is triggered above the sheared core, the overlying fields diminish, releasing the ties imposed on the sheared core and letting it erupt. Antiochos et al. (1999) shown that magnetic configurations possibly leading to this process can be found above delta spots, sunspots associated with the largest flares (McIntosh, 1990).

Examples of another mechanisms which can lead to eruptions involve e.g., the emergence or injection of magnetic flux into flux ropes and surrounding corona. The emerging flux triggering mechanism (Chen and Shibata, 2000) describes how do newly-emerged flux concentrations affect the stability of filaments below or near which they appear. The flux injection mechanism involves eruption due to a local increase of the poloidal flux of a previously-stable flux rope (Chen, 1996). In this case, the onset of the eruption is not only caused by the reconfiguration of the magnetic fields due to magnetic reconnection only, but due to magnetohydrodynamic (MHD) instabilities.

According to Forbes (2000), four different categories of MHD models of solar eruptions can be distinguished. In the first category, the eruptions are due to instabilities whose development is allowed by the simplest ideal (non-resistive) MHD approach. The formation of the current sheets and related magnetic reconnection is driven by the eruption itself which does not depend on it (e.g., Priest and Forbes, 1990). The resistive MHD approach, representing the second class, allows for a presence of finite (but small) resistivity, leading to magnetic reconnection in sheared arcades of field lines driving the eruption (e.g., Mikić and Linker, 1997). The ideal and resistive MHD models are combined in the third class. This approach has been utilized e.g., by Lin et al. (1998). In their model, coronal magnetic fields decay due to photospheric motions, leading to violation of the ideal MHD equilibrium. This loss of equilibrium however does not lead to the eruption of the flux rope, but to development of a current sheet below it. When the reconnection rate there is high enough, the flux rope erupts. The last, fourth class concerns effects of the gravity and gas pressure on the stability of flux ropes (e.g., Wolfson and Saran, 1998). This approach is however only applicable on CMEs consisting of prominence material, which are rare (Section 2.1.3).

Among ideal MHD instabilities that could lead to eruptive flares are the kink, loss-of-equilibrium, and torus instabilities. Flux ropes can undergo the helical kink instability when they are twisted about the flux rope axis, with the twist exceeding a certain threshold (Hood and Priest, 1981; Török and Kliem, 2005). The loss-of-equilibrium instability concerns a category of flux ropes which rise to a certain height beyond which no equilibrium state can be found (Roussev et al., 2003). The torus instability (Chen, 1989; Kliem and Török, 2006) can occur naturally in toroidal current rings embedded in external poloidal fields. Upon expansion, such rings are subjects to the hoop force (Lorentz-self force) whose gradients point radially. Bateman (1978) was the first to show that the instability sets on when the critical decay index

$$n = -\frac{d \ln B_{\text{ex}}}{d \ln R} \quad (2.1)$$

is greater than  $3/2$ . There,  $B_{\text{ex}}$  is the intensity of the external magnetic field and  $R$  is the radius of the current-carrying ring. Over the years, authors of numerous studies attempted to specify the exact value of the critical decay index (e.g., Kliem and Török, 2006; Olmedo and Zhang, 2010; Zuccarello et al., 2016; Vasantharaju et al., 2019; Cheng et al., 2020). Zuccarello et al. (2015) shown that instead of the commonly-accepted threshold of  $n > 3/2$ , the values of the decay index leading to instabilities range roughly between 1.3 and 1.5, depending on the magnetic configuration of the flux rope built

by photospheric motions. As was shown by Isenberg and Forbes (2007), the instability criterion is also affected by the height and length of the modelled flux rope. Observations of torus-unstable flux ropes were presented e.g., by Zuccarello et al. (2014), Rees-Crockford et al. (2020), or in the statistical study of Jing et al. (2018). The torus instability is the triggering mechanism in the standard solar flare model in 3D that we utilise in this work (see Section 3.2).

It has been noted (Chen, 2011) that some of the eruption triggering mechanisms are similar to each other. In reality, some of them are complementary, driving a single eruption (e.g., Longcope and Forbes, 2014; Chen et al., 2015; Inoue et al., 2016; Chen et al., 2018). For example, Démoulin and Aulanier (2010) argue that the torus and loss-of-equilibrium instabilities are manifestations of the same physical mechanism. Further, Aulanier et al. (2010) showed that in bipolar fields, the pre-flare activity associated with the build-up of the erupting flux rope is consistent with both flux cancellation and the tether-cutting reconnection. The analysed flux rope however erupted due to the torus instability. In any case, the nature of the process which finally leads to eruption is mainly contingent on the configuration of the external coronal field (e.g., Fan and Gibson, 2007). Nevertheless, the analysis of Chifor et al. (2007) still shown that the observations of pre-flare activity are most consistent with the tether-cutting reconnection, which was later supported in numerous studies (e.g., Kim et al., 2008; Sterling et al., 2011; Kliem et al., 2021). We will therefore next describe standard models of solar flares and eruptions in two and three dimensions, which involve magnetic configurations consistent with the tether-cutting reconnection.

### 2.3 Two-dimensional model of solar flares

Perhaps the most commonly-accepted picture of the flaring mechanism is conveyed in the standard two-dimensional model of solar flares (e.g., Hudson and Cliver, 2001; Shibata and Magara, 2011). It is sometimes termed as ‘CSHKP’ model, an acronym consisting of initials of authors of pioneering papers on solar flares published in the 1960s and 1970s (Carmichael, 1964; Sturrock, 1966; Hirayama, 1974; Kopp and Pneuman, 1976). The model describes the release of the magnetic energy stored in pairs of converging field lines. Upon reconnecting, they lead to the formation of features typically observed during flares. The key processes are usually combined in a single schematic cartoon, of which numerous variations can be found throughout the literature. Their eventual modifications incorporated advances in the understanding of magnetic reconnection as well as phenomenology based on the observations of flares (see e.g., Priest and Forbes, 2002).

One of the popular versions of the CSHKP model, presented by Shibata et al. (1995), is shown in Figure 2.1. The field lines first converge to a null point, sometimes called the X point or the neutral point, a place where the intensity of the local magnetic field equals zero. There, the X point collapses into the current sheet in which field lines undergo reconnection. The solar corona is an ideal environment for the formation of such structures (Low and Wolfson, 1988; Parker, 1994). Indirect evidence for the existence of current sheets has been found in cusp-shaped loops. Their apexes are thin and elongated, and are reminiscent of field lines below coronal current sheets (e.g., Tsuneta et al., 1992; Tsuneta, 1996; Yokoyama et al., 2001).

As flare progresses, more magnetic flux is carried to the reconnection region by reconnection (coronal) inflows (e.g., Hara et al., 2006; Narukage and Shibata, 2006), first observed by Yokoyama et al. (2001). Newly-reconnected field lines and associated elements of plasma leave the reconnection region via the down- and up-ward oriented reconnection jets, also termed reconnection outflows.

According to the CSHKP model, one part of the energy converted by magnetic reconnection escapes the Sun together with the erupting structure. In the left panel of Figure 2.1, it is indicated as filament (Section 2.1.3) or plasmoid. Plasmoids are blobs of plasma which were first noticed above flare loops by Ohyama and Shibata (1998). These structures have been modelled in 2D MHD simulations of Karlický and Bárta (2007) and Bárta et al. (2008), who focused on the formation of ‘magnetic islands’ – portions of current sheets undergoing the tearing mode instability (Furth et al., 1963). It has been evidenced that apart from escaping the Sun (e.g., Zhu et al., 2016), plasmoids can move downward, but also coalesce and oscillate (Jelínek et al., 2017). The downward-propagating plasmoids can collide with the arcade of flare loops developing below the current sheet and trigger its oscillations, in line with the observations of Veronig et al. (2006).

The reconnection outflows directed toward the solar surface cause the formation of flare loops. The transparent loop plotted in the left panel of Figure 2.1 is a newly-reconnected field line. The downward-pointing arrows drawn in this loop indicate the precipitation of the particles accelerated by reconnection. The particles penetrate into the solar chromosphere, which is much denser than the corona and therefore they decelerate. Their kinetic energy is converted into the heating of the chromosphere (Ichimoto and Kurokawa, 1984; Wuelser et al., 1994). This process, sometimes termed

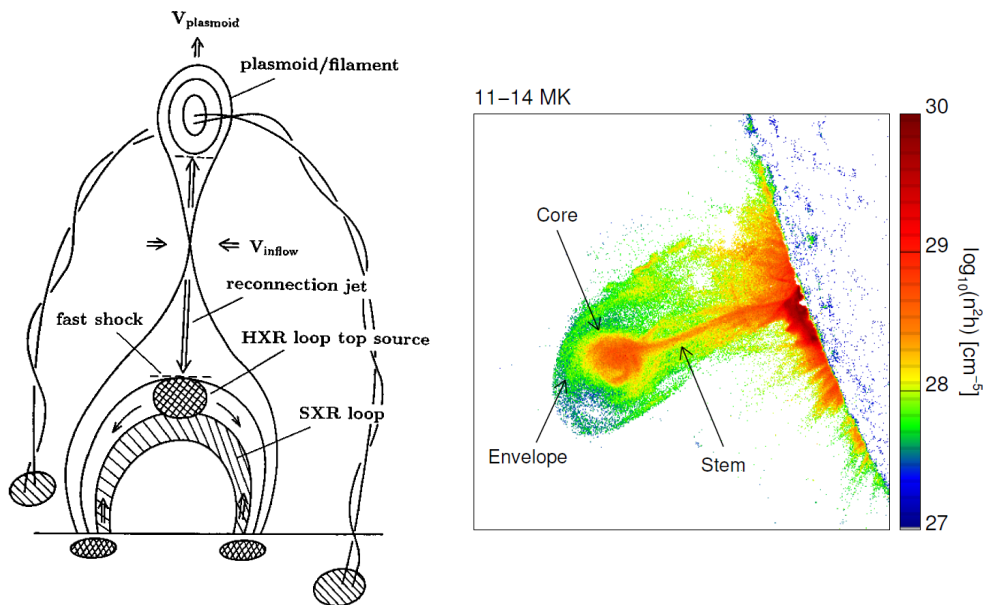


Figure 2.1: Left: The standard flare model in two dimensions. Adapted from Shibata and Magara (2011). © AAS. Reproduced with permission. Right: Eruptive flare from 2010 November 3 whose morphology qualitatively agrees to that of the two-dimensional flare model. Adapted from Hannah and Kontar (2013), reproduced with permission © ESO.

as the chromospheric condensation (e.g., Graham et al., 2020), can be regarded as deposition of the energy released in the corona down in the chromosphere (Section 2.1.2). This energy transport is manifested in downflows of plasma, typically corresponding to speeds of a few tens of  $\text{km s}^{-1}$ . Their signatures are redshifts of spectral lines formed in the solar chromosphere and the transition region ( $\log(T [\text{K}]) = 4 - 5$ ). After the chromospheric plasma has been heated, it starts to expand and upflow along the newly-reconnected field line, filling it with hot plasma whose temperature might exceed  $\log(T [\text{K}]) = 7$  (Doschek et al., 1980). This process is known as the chromospheric evaporation (e.g., Acton et al., 1982; Zarro et al., 1988; Antonucci, 1989; Del Zanna et al., 2002) which produces SXR loops, such as the one indicated using dash-like pattern in the 2D model cartoon (Figure 2.1, left). The chromospheric evaporation is manifested in blueshifts of lines forming at coronal and flare temperatures ( $\log(T [\text{K}]) = 6 - 7$ ). During impulsive phases of flares, the evaporation occurs in the ‘explosive’ regime, when its speeds can reach hundreds of kilometres per second (e.g., Feldman et al., 1980b; Watanabe et al., 2010; Tian et al., 2014; Polito et al., 2016). In the gradual phase, the evaporation slows to speeds of a few to a few tens of kilometres per second (Schmieder et al., 1987; del Zanna et al., 2006; Dudík et al., 2016). Note that Canfield et al. (1987) suggested that the momenta of the plasma downflows caused by the energy deposition are balanced with those of the upflows due to the chromospheric evaporation.

After the first flare (SXR) loops have appeared, the reconnection jet can hit their loop-tops, resulting in the development of the fast MHD shocks sometimes termed termination shocks (e.g., Polito et al., 2018). These shocks are thought to lead to the formation of the loop-top sources of HXR radiation, indicated using the patterned circle in Figure 2.1 (left). Apart from the fast shocks, cartoons containing the 2D model sometimes include the slow MHD shocks which guide the reconnection jets. In the model of Forbes and Malherbe (1986), the slow shocks are splitted into isothermal slow shocks and conduction fronts penetrating the chromosphere and heating the plasma. Cargill and Priest (1983) shown that the heating by the slow shocks is sufficient for production of flare loops emitting in  $\text{H}\alpha$ . Another manifestation of the reconnection outflows are supra-arcade downflows (SADs; Savage et al., 2010). SADs, first reported by McKenzie and Hudson (1999), are observed as dark voids (resp. faint loops) which fall down (shrink) toward flare arcades at apparent speeds roughly between 100 and  $200 \text{ km s}^{-1}$ . The interpretation of SADs was elaborated by Savage et al. (2012) who proposed that SADs are low-density regions created by retraction of thin flux tubes from the reconnection region. SADs can happen during all phases of flares and the times of their occurrence are very well correlated with observations of the HXR loop-top sources (Asai et al., 2004).

Finally, below the footpoints of the SXR loop, the footpoint sources of the HXR radiation are indicated using the same patterned circles as the loop-top source. Even though one could argue the model contains the flare kernels at each footpoint of the flare loop, it cannot address flare ribbons

themselves as it misses one dimension. Therefore, 2.5D extensions of the standard model have been developed (e.g., Tripathi et al., 2006). They are based on stacking the 2D models along the third (missing) dimension while preserving the translational symmetry (Shiota et al., 2005). The 2.5D models thus contain the entire arcade of flare loops organized one after another and the flare kernels at their footpoints form continuous lines representing flare ribbons.

The CSHKP model addresses many basic structures routinely associated with flares. The events which the model can qualitatively reproduce are usually observed at the solar limb. Such flares are viewed from the side, at which their morphology along the axis of the erupting structure is not distinguished. An example of such event is the CME from 2010 November 3 analysed by Hannah and Kontar (2013) (Figure 2.1, right). There, the spatial distribution of the emission measure of 11 – 14 MK plasma is shown, revealing a circular plasmoid wrapped in the envelope of coronal material. Below it, the filamentary stem associated with current sheet can be distinguished.

The cartoon containing the CSHKP model does not, and of course cannot, convey the entire flaring process. The model does not explain triggering of the flare, but only depicts how field lines reconnect once the flare is underway. Similarly, the model does not address the relation between flare arcades and dimming regions, as the latter have substantially longer lifespans (see Section 6.1. in Hudson and Cliver, 2001). Most importantly, the various versions of the two-dimensional CSHKP model as well as its 2.5D extensions still describe a process which is inherently three-dimensional (Hudson, 2011). Perhaps the most important issue of the 2.5D models concerns the magnetic configuration consisting of null points stacked along one axis, joined by a separator line (Section 3). In practice, such configuration would not be stable and can not lead to flare (Hesse and Schindler, 1988). Therefore, over the last decades, the community has been focused on the development of the theory of 3D magnetic reconnection hand-in-hand with its applications to solar flares and eruptions. Their brief description is the objective of the following section.



# 3. Magnetic reconnection in three dimensions

## 3.1 Magnetic topology in three dimensions

### 3.1.1 Three-dimensional null points

Three-dimensional magnetic topology is more involved than that included in the CSHKP model of a solar flare in 2D. The first topological features we introduce are 3D null points. 3D null points occur in quadrupolar configurations, produced for example when a compact bipolar source of magnetic flux emerges in a pre-existing bipole (e.g., Antiochos, 1998; Török et al., 2009). Magnetic field lines located in the vicinity of 3D null points are organised in a specific manner. Their topology consists of a magnetic spine surrounded by parallel field lines which diverge from the null point and form a fan surface, or a fan plane, along which they spread away (e.g., Longcope, 2005). The distribution of the magnetic field lines near 3D null points can be derived analytically, as they must satisfy Gauss’s law  $\vec{\nabla} \cdot \vec{B} = 0$ . An example of 3D null with associated spine and fan surface are plotted in Figure 3.1(a). This simple and symmetric configuration, suggested by Priest (2001), corresponds to field components

$$(B_x, B_y, B_z) = (x, y, -2z). \quad (3.1)$$

Lau and Finn (1990) showed that the magnetic fields in vicinity of 3D null points have three eigenvectors and eigenvalues. A symmetric configuration containing the spine curve and the fan surface can be recovered in the case when all three eigenvalues are real, two have the negative sign and one is of the positive sign. In that case the spine follows the eigenvector with the single sign (here the  $z$  axis) and the fan surface spreads in the plane given by the two eigenvectors of the opposite sign (here the  $x$  and  $y$  axes). Theoretical concepts of the reconnection at the fans and spines were investigated e.g., by Priest and Titov (1996). Spine reconnection is manifested in the change of connectivity due to continuous motions of the footpoints across the fan surface. On the contrary, reconnection at the fan occurs when the conjugate footpoints of associated field lines move across the spine. Reconnection occurring in these geometries gave rise to the theory of the magnetic flipping, a rapid, but continuous, change of connectivity in the spine and fan discontinuities termed flipping layers (Priest and Forbes, 1992; Priest and Schrijver, 1999; Masson et al., 2009).

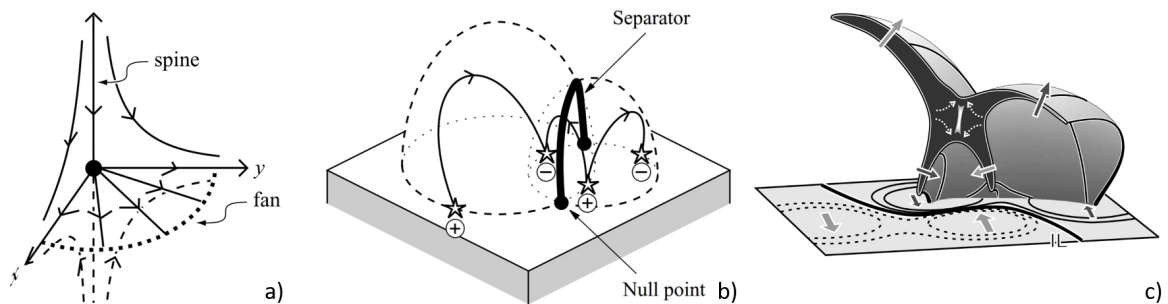


Figure 3.1: Structures associated with three-dimensional magnetic topology. Panel (a) shows magnetic null point in 3D and its related features; the magnetic spine and the fan surface. In panel (b), two separatrix surfaces forming ‘domes’, highlighted using dashed lines, are shown. Their intersection, formed by the separator line joining the null points, is indicated. Panels (a) and (b) were adapted from Priest (2001) and reproduced by permission © Springer Nature. Panel (c) shows the cross-section of the hyperbolic flux tube modelled by Titov et al. (2003). The reconnection region in the middle of the structure is also indicated. © AAS. Reproduced with permission.

Coronal magnetic fields have a very complex structure and the magnetic fields surrounding the null points are usually not symmetric. Al-Hachami and Pontin (2010) found that asymmetric fields around the null points still show the typical spine/fan topology. In their numerical experiments, they found that deviations from the symmetrically distributed fields affect the dimensions of the current sheet at null. Complex magnetic configurations might contain multiple null points. An example of such topology, adapted from Priest (2001), is shown in panel (b) of Figure 3.1. It consists of two positive and two negative polarities at the bottom boundary, which are joined by three field lines. The field

lines bordering domains of specific connectivity are called separatrix surfaces (dashed), or separatrix curves in a 2D case (Mandrini et al., 1991; Lau, 1993). The separatrix surfaces intersect in the separator line, which in this case joins two null points. Along separators, current sheets can form, triggering the separator reconnection (e.g., Longcope and Cowley, 1996).

Apart from null points, the separatrix surfaces can be associated with photospheric magnetic dips called bald patches (Titov et al., 1993). The bald patches are topological features in which field lines are tangent to the photosphere, for example when field lines of two neighboring bipoles touch above the PIL. The existence of the bald patches was, for the first time, observationally confirmed by López Ariste et al. (2006).

The topological features of the configuration shown in Figure 2.1(b) are usually plotted in so-called magnetic skeletons, which are used to map the complicated fields in which the corona is often organized (e.g., Priest and Titov, 1996). Since the coronal magnetic fields are difficult to measure, the identification of the null points in the corona relies on extrapolations of the coronal magnetic fields (see e.g., the review of Schmieder et al., 2015). This task is based on measurements of the photospheric magnetic field contained in line-of-sight or vector magnetograms, usually under the assumption of linear and nonlinear force-free fields (e.g., Alissandrakis, 1981; Amari et al., 1997; Wiegmann, 2008).

Examples of analyses employing magnetic field extrapolation in order to find 3D null points and associated topological features were presented e.g., by Sun et al. (2013) and Mandrini et al. (2014). Together with high-resolution imagery of the flare and corona, these studies confirmed that in some flares, field lines indeed reconnect in the fan/spine topology. Magnetic reconnection in such configuration is typically manifested in the formation of circular flare ribbons (e.g., Masson et al., 2009, Section 2.1.2). As however pointed out by Schmieder et al. (2015), some observations indicate that flaring activity is not necessarily related to null points. This makes the null point reconnection only one specific category of reconnection processes powering flares.

### 3.1.2 Quasi-separatrix layers

Three-dimensional magnetic reconnection is not contingent on a presence of null points or separators. The cornerstone of the ‘general magnetic reconnection’ in such topologies was laid by Hesse and Schindler (1988) and Schindler et al. (1988), who proposed that the necessary and sufficient condition for magnetic reconnection is

$$\int E_{\parallel} ds \neq 0, \quad (3.2)$$

integrated along a selected magnetic field line. This equation means that magnetic field lines can reconnect when electric currents parallel to them develop. This definition includes all non-ideal MHD effects which potentially lead to formation of electric currents with the parallel component (Section 6 in Priest, 2014). The groundbreaking prediction of Schindler et al. (1988) was first vindicated in the analysis of Démoulin et al. (1994), who used observations of flare kernels combined with reconstructions of the observed magnetic fields to show that can flares indeed occur in environments where no null points are present. Instead, their results indicate that whether and where the field lines reconnect depends only on characteristics of the local magnetic field. Similar outcomes were later presented in observational analyses by Li et al. (2006) and Schmieder et al. (2007). Even though some null points were present in regions where the flares in these studies occurred, none of them played a role in their triggering. An example of a flare which occurred in a topology completely free of null points was presented e.g., by Schrijver et al. (2011).

Magnetic reconnection in configurations without null points or bald patches was further studied by Priest and Démoulin (1995). In an isolated domain without these features, field lines were reconnecting in so-called quasi-separatrix layers (QSLs). QSLs are thin volumes across which the magnetic connectivity varies rapidly but is continuous, in contrast to the discontinuities in magnetic connectivity associated with true separatrices. When one footpoint of a given field line moves through QSL, the high distortion of connectivity causes a rapid flipping of its conjugate footpoint (see e.g., Figure 9 in Priest and Démoulin (1995)). QSL can be thought of as a generalisation of the magnetic flipping layer mentioned in Section 3.1.1.

The method used for tracing of QSLs above the photosphere is based on the identification of regions where the connectivity of individual field lines dramatically changes. To do that, the mapping norm  $N$  of field line connectivity has been introduced (Démoulin et al., 1996a). This quantity measures the displacement of one of the footpoints with coordinates  $(X, Y)$  of a given field line, with respect to a slight shift of its conjugate footpoint  $(x, y)$ . The norm can be calculated as

$$N = \sqrt{\left(\frac{\partial X}{\partial x}\right)^2 + \left(\frac{\partial X}{\partial y}\right)^2 + \left(\frac{\partial Y}{\partial x}\right)^2 + \left(\frac{\partial Y}{\partial y}\right)^2}. \quad (3.3)$$

The footpoint traces of QSLs, determining the variations of the field line connectivity across the photosphere, correspond to high values of  $N$ . The norm however varies when the conjugate footpoint of the same field line is taken as the reference one. Titov et al. (2002) therefore introduced the squashing degree  $Q$ , which combines the norms calculated at both footpoints of a selected field line (Pariat and Démoulin, 2012):

$$N_{12} = \sqrt{\left(\frac{\partial X_2}{\partial x_1}\right)^2 + \left(\frac{\partial X_2}{\partial y_1}\right)^2 + \left(\frac{\partial Y_2}{\partial x_1}\right)^2 + \left(\frac{\partial Y_2}{\partial y_1}\right)^2}, \quad (3.4)$$

$$N_{21} = \sqrt{\left(\frac{\partial x_1}{\partial X_2}\right)^2 + \left(\frac{\partial x_1}{\partial Y_2}\right)^2 + \left(\frac{\partial y_1}{\partial X_2}\right)^2 + \left(\frac{\partial y_1}{\partial Y_2}\right)^2}, \quad (3.5)$$

weighted by the ratios of the horizontal components of the magnetic field:

$$Q = Q_{12} = \frac{N_{12}^2}{|B_{z,1}(x_1, y_1)/B_{z,2}(X_2, Y_2)|} = Q_{21} = \frac{N_{21}^2}{|B_{z,2}(X_2, Y_2)/B_{z,1}(x_1, y_1)|}. \quad (3.6)$$

Similarly to  $N$ , QSLs are then defined by regions with high values of  $Q$ . Intersections of QSLs, especially when recovered in a quadrupolar configuration, form a 3D structure termed a hyperbolic flux tube (HFT; Titov et al., 2002). In 3D magnetic topology, HFTs are preferable sites for the reconnection of magnetic field lines. A transverse cut through HFT, adapted from Titov et al. (2003), is shown in Figure 3.1(c). At its centre (black), the reconnection region, where the highest currents develop, is indicated (see also Aulanier et al., 2005). Clearly, the morphology of HFTs is indeed reminiscent of two intersecting hyperboles. HFTs can be thought of as a 3D representation of hyperbolic field lines near the null point described of the CSHKP model of solar flares (Section 2.3). They can also be related to the intersection of two separatrix surfaces plotted in panel (b) of Figure 3.1, however, in terms of the generalised 3D magnetic reconnection occurring in QSLs.

Theoretical concepts of magnetic reconnection in QSLs associated with flares and eruptions were elaborated by Démoulin et al. (1996b). The authors investigated the formation of QSLs associated with flux ropes formed in different magnetic configurations. They found that the bottom traces of QSLs have a double- $J$  pattern, corresponding to the morphology typically exhibited in two-ribbon flares. While the straight parts of  $J$ s are parallel to the PIL, their curved parts are located at the periphery of the domain, where the modelled flux rope was rooted. The curvature of the round parts of  $J$ s was found to depend on the twist of the flux rope field lines rooted below the domain.

In practice, calculations of QSLs in 3D present a very difficult challenge, which involves tracing numerous field lines related to the flare. Fast codes aimed to speed and facilitate this task have therefore started to appear (e.g., Tassev and Savcheva, 2017). Nevertheless, authors of several studies (e.g., Savcheva et al., 2012, 2015; Janvier et al., 2016; Zhao et al., 2016) managed to do so, for example by employing the numerical methods investigated by Pariat and Démoulin (2012). Distribution of QSLs is usually obtained at either the bottom boundary of flare, or in vertical cuts through it. A comparison between the QSLs footprints and flare ribbons, analysed by Zhao et al. (2016), is shown in Figure 3.2. In the left panel,  $J$ -shaped (hooked) flare ribbons observed in the 304 Å filter channel

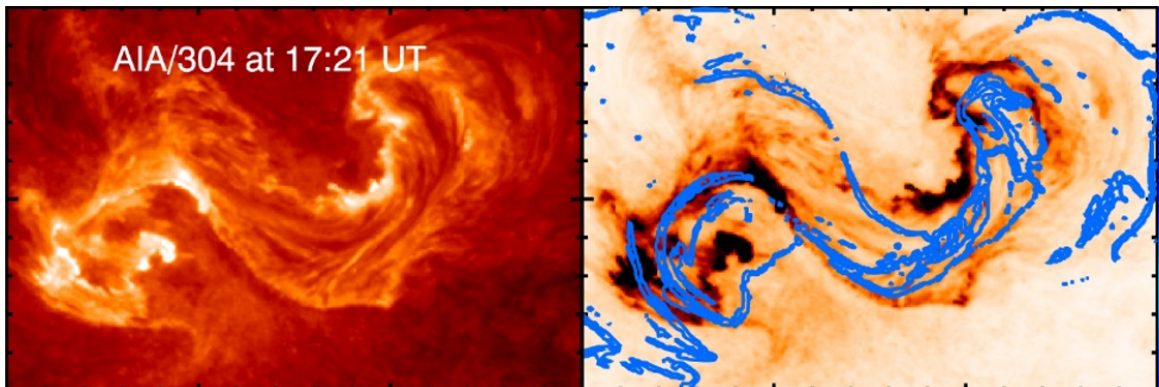


Figure 3.2: Left: Flare ribbons observed in the 304 Å filter channel of AIA. Right: Quasi-separatrix layer (QSL) footprints at the bottom of the domain, recovered from non-linear force-free field extrapolations of a magnetogram observed by HMI (blue). QSLs are plotted atop the 304 Å image with inverted color-scale. Adapted from Zhao et al. (2016). © AAS. Reproduced with permission.

of AIA are shown. QSL footprints, obtained at the lower boundary of the domain, are plotted in the right panel using blue color. The calculations of QSLs are based on measurements of the magnetic field strength from the Helioseismic and Magnetic Imager (HMI; Scherrer et al., 2012, Section 4.1.2) onboard SDO. The respective magnetogram was acquired two hours before the onset of the eruption and the distribution of the magnetic field was obtained using non-linear force-free field extrapolations. To ease the comparison of the structures, the QSLs have been plotted atop the 304 Å data with reversed colors. An agreement between the locations of QSLs and flare ribbons is apparent. This demonstrates that flare ribbons indeed form as a consequence of magnetic reconnection, as they are spatially coincident with field lines with high gradients of connectivity.

Note that slight discrepancies between the two are due to the temporal evolution of the ribbons, which QSLs do not reproduce as they were recovered in one instant only. Nevertheless, observational case-studies such as the presented one provide ever-growing support for the QSL reconnection as a favourable, general picture of 3D magnetic reconnection.

## 3.2 Standard flare model in three dimensions

The progress in understanding of the general magnetic reconnection and MHD processes in solar plasma played an important role in the development of models of eruptions in three dimensions. Carrying-out this ambitious goal was possible only thanks to super-computers.

Over the last two decades, numerous 3D MHD models of eruptions were developed. At their centre is a flux rope which becomes unstable either due to ideal or non-ideal MHD processes, or its eruption is forced. Regardless of its origin, the characteristics of the eruptions vary among different simulations, as they are usually modelled in distinct magnetic environments. While some models occur in theoretical bipolar or quadrupolar configurations (Amari et al., 2000; Aulanier et al., 2010; Török et al., 2010; Schrijver et al., 2011; Syntelis et al., 2017), some are case-dependent, based on observed distributions of the magnetic field (e.g., Evans et al., 2011; Lugaz and Roussev, 2011; Lugaz et al., 2011; Inoue et al., 2015; Xue et al., 2016; Price et al., 2019). A combined approach was employed e.g., by Savcheva et al. (2012), who evidenced that magnetic fields and topological features reproduced in simple bipolar configurations can well mimic those obtained in observed, more complicated, configurations.

Each model is developed with a specific purpose, addressing different aspects of the evolution of flares and eruptions; from the build-up of the erupting structure (e.g., Aulanier et al., 2010) to its propagation through the interplanetary space (e.g., Lugaz and Roussev, 2011). In this study, we mainly focus on magnetic reconnection driving the build-up and early evolution of erupting flux ropes. Their description is well addressed by the standard flare model in three dimensions (Aulanier et al., 2012, 2013; Janvier et al., 2013).

### 3.2.1 Basic properties of the model

The standard flare model in 3D is based on the model of the torus-unstable flux rope of Aulanier et al. (2010). It was developed using the *Observationally-driven High-order scheme Magnetohydrodynamic* code (OHM; Aulanier et al., 2005), which calculates the temporal evolution of the mass density, plasma velocity, and the magnetic field, given by the basic MHD equations (Section 1.3). The model is constructed under the zero- $\beta$  approximation, i.e., does not include plasma temperature.

Aulanier et al. (2010) first describe the build-up of the flux rope. Initially, a potential arcade of field lines joins two polarities of the bipole. Due to the slow motions induced at the photosphere, the arcade becomes sheared and this shear increases as the time goes by (Figure 1 in Aulanier et al. (2010)). Later, a bald patch (BP) appears, becoming a location in which field lines start to reconnect. As a result, long field lines composing a weakly-twisted *S*-shaped flux rope start to appear. Further shearing leads to the transformation of BP to a hyperbolic flux tube (HFT). The quasi-separatrix layers (QSLs) exhibit a double-*J* pattern surrounding the footpoints of the flux rope. In HFT, field lines reconnect in the slip-running reconnection regime (Section 3.2.2), further producing *S*-shaped field lines contributing to the flux rope build-up. Further, as a consequence of the reconnection, sheared flare loops form below the flux rope. The generation of the *S*-shaped field lines and flare loops is in line with the theoretical predictions imposed for the tether-cutting reconnection in a sigmoid (Section 2.1.3), which the growing flux rope morphologically reminds. This shows that the slip-running reconnection is consistent with the tether-cutting reconnection of sheared arcades. However, neither the tether-cutting reconnection, nor the shearing motions of the photosphere and related flux cancellation at the PIL cause the eruption (Figure 3 in Aulanier et al. (2010)). Instead, these mechanism drive the formation and slow rise of the flux rope. Upon reaching a certain height in which the condition for the torus instability is met (Equation 2.1), the flux rope starts to rise exponentially and then erupts.

The model further describes the electric currents developing during the eruption. At the bottom of the domain, local increases of the electric current density were found in photospheric traces of QSLs, associated with flare ribbons (see e.g., Janvier et al., 2016). These electric currents were studied by Janvier et al. (2014) who, among other, shown that flare ribbons possibly form due to the collapse of the coronal current sheet, leading to an impulsive energy release via reconnection.

The highest coronal electric current densities develop in the vertical current sheet below the erupting flux rope, where the flare reconnection, leading to the formation of flare loops, takes place. The development of the arcade of flare loops in the standard flare model in 3D is detailed in Aulanier et al. (2012). Since the reconnection involves sheared field lines located above the PIL, the newly-reconnected flare loops are sheared too. As the time goes by during the eruption, the shear is relaxing to a nearly-potential state, at which the arcade becomes nearly perpendicular to the PIL. This strong-to-weak transition of flare loops is driven not only by magnetic reconnection, but also by straightening of the inner legs of the erupting flux rope. In Aulanier et al. (2012), the strong-to-weak transition was also analysed in observations of a C5.4-class flare accompanied by a CME. The observed evolution of the shear corresponded well to that predicted by the simulation.

In our work, we utilised the extensions of the model corresponding to the latest runs of the OHM code performed by Zuccarello et al. (2015). The evolution of the eruption corresponding to these runs, adapted from Aulanier and Dudík (2019), is shown in Figure 3.3. The field lines plotted therein were traced using the *Topology and field line Tracing* code (TOPOTR; Démoulin et al., 1996b). In panel (a), the flux rope (pink) is surrounded from one side by the orange field lines. Before the eruption, these were forming an inclined coronal arcade. Further, the green field lines overlaying the flux rope are shown. The orange and green arcade field lines reconnect with the flux rope when its eruption is in progress (panels (b) and (c)). In panel (c), the closed field lines representing flare loops forming below the flux rope can be distinguished.

The photospheric footprints of QSLs at respective times are plotted in panels (d) – (f). The grey-scale color coding marks the variations of  $\log(Q)$  which ranges between 0 (black) and 4 (white). Yellow labels and arrows are used to mark the PIL and the straight portions of the ribbons together with their separating motion, while green color denotes the ribbon hooks.

The standard flare model in 3D and its extensions provided theoretical background for various flare-related phenomena observed in numerous studies. For example, Aulanier et al. (2013) utilised the model to provide constraints on the total energy released during the largest flares. Zuccarello et al. (2015) analysed how is the critical decay index (Equation 2.1) affected by different current profiles

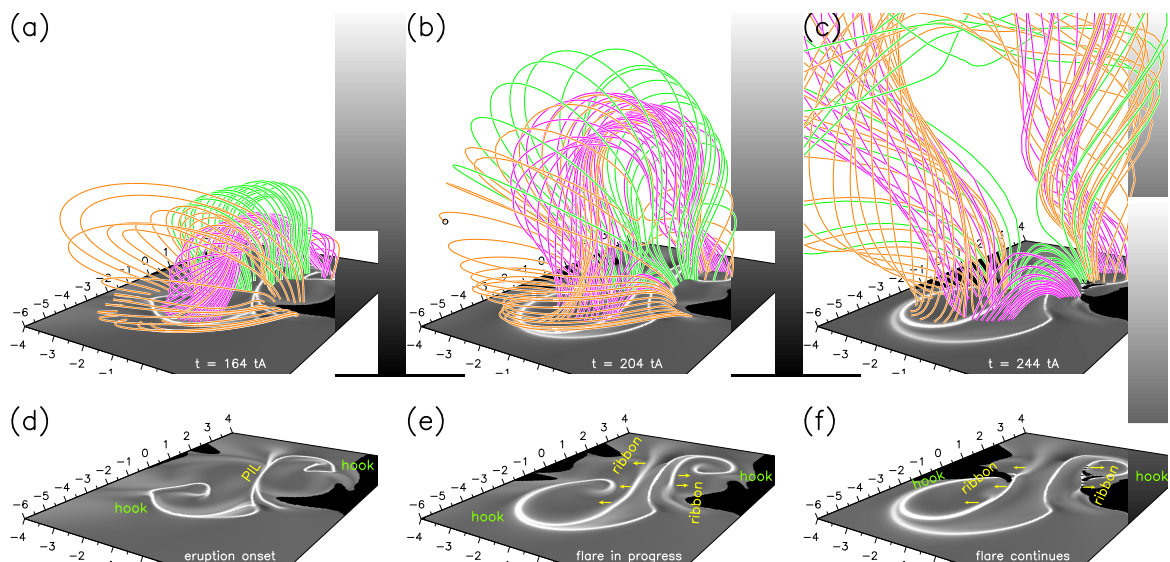


Figure 3.3: Standard flare model in 3D. Panels (a) – (c) detail the temporal evolution of the eruption of the flux rope, depicted using the pink field lines in panel (a). The orange field lines from the same panel represent field lines surrounding the legs of the flux rope. The green field lines in panel (a) are arcades overlying the flux rope. By the end of the simulation, both the orange and green field lines reconnect to become parts of the flux rope and flare loops (panels (b), (c)). At the bottom of the domain, the variations of  $Q$  are indicated using the greyscale. The PIL and the photospheric traces of QSLs corresponding to the ribbons and ribbon hooks are indicated. Adapted from Aulanier and Dudík (2019), reproduced with permission © ESO.

in flux ropes and/or varying dynamics of the photosphere before the eruption. The model was also used to identify the presence of two coronal vortices at both sides near the legs of the erupting flux rope (Zuccarello et al., 2017) that were subsequently found in observations (Dudík et al., 2017) as a co-existence of expanding and contracting motions of coronal loops. This provides an alternative explanation for the contracting motions of loops previously attributed to ‘coronal implosion’ (e.g., Hudson, 2000; Simões et al., 2013; Russell et al., 2015).

Recently, the model was utilized in an investigation of evolution of magnetic field and electric currents at footpoints of eruptions. Barczynski et al. (2019) used the model to interpret the increase of the horizontal component of photospheric magnetic field and downward Lorentz force observed along PILs during eruptions. They found that this increase is caused by the contraction of sheared flare loops driven by reconnection. Analysis of development of electric currents at footpoints of solar flares was performed by Barczynski et al. (2020). Electric currents, measured in the regions encircled by the hooks during 9 eruptive X-class flares as well as the OHM 3D MHD simulation, exhibited a consistent decrease. This decrease was interpreted in terms of the expansion of the erupting flux rope in the corona.

Most importantly, this model provides a general picture of how do the field lines reconnect in 3D. The most important theoretical properties as well as the first observations of this process are described in the next section. Last but not least, the model describes the geometries in which different pairs of field lines, composing and surrounding the flux rope, reconnect during the eruption. Their description is left for Section 3.2.3.

### 3.2.2 Slipping and slip-running reconnection

As mentioned in Section 3.1.2, quasi-separatrix layers correspond to regions in which field lines reconnect by magnetic flipping (e.g., Priest and Schrijver, 1999). This process was first treated analytically in kinematic models involving calculations of velocity of plasma frozen-in the field lines which were reconnecting by flipping in QSLs (Priest and Démoulin, 1995). Later, analysis of magnetic reconnection in QSLs became the aim of 3D MHD models (see e.g., the review of Janvier et al., 2015).

In a simple MHD model, Pontin et al. (2005) considered a bundle of parallel magnetic field lines tied at the two opposite boundaries of a cubic domain. These boundaries then started to exhibit shearing motions and the field lines became sheared. Once the nonideal MHD processes were introduced by including the resistivity in the center of the domain, magnetic reconnection begun. Field lines were continually changing their connectivities, as their footpoints flipped to regions with low resistivity. The flipping was occurring until all of the field lines had left the diffusion region (Figure 6 therein). The magnetic flipping was later reproduced by Aulanier et al. (2006) in much narrower QSLs and associated HFT formed in quadrupolar configuration. This can, unlike the configuration of Pontin et al. (2005), be easily related to flares. The authors found that sets of field lines within QSLs, which pass each other, gradually change their connectivities from one to another. A key signature of the *slipping reconnection* is the apparent slipping motion (‘slippage’) of field line footpoints along the photospheric traces of QSLs. The motion is only apparent because it is not a signature of true motion of field lines. Instead, it is a manifestation of a sequential appearance of newly-reconnected field lines one next to another. If QSLs are sufficiently thin, the motion can occur at super-Alfvénic speeds, for which the term *slip-running reconnection* was coined (Aulanier et al., 2006). The same simulation also shows that the slipping reconnection can be triggered by the compression of field lines in HFT (magnetic pinching) and the dissipation of current layers, without the need for the shearing motions induced at the footpoints of field lines.

All of the field lines reconnecting in the standard flare model in 3D do so via the slipping reconnection, in either the slipping or slip-running mode. Characteristics of the slipping reconnection in the standard flare model in 3D were investigated by Janvier et al. (2013). The formation of the sheared flare loops via the slipping reconnection, detailed in Figures 4, 6, and 7 of Janvier et al. (2013), is summarized in Figure 3.4. The first two rows show colored field lines which slip along the *J*-shaped extension of the photospheric footprint of QSLs, viewed from the top (panels (a) – (c)) and side (panels (d) – (f)). In the same panels, the PIL is plotted as the yellow line and the negative and positive polarities of the bipole are indicated using the cyan and magenta contours. The black and white regions of the background plotted in greyscale correspond to regions with high electric currents associated with flare ribbons. As can be seen in panels (a) and (d), the field lines are initially *J*-shaped, joining the straight part of the negative polarity ribbon with the curved part of the conjugate ribbon (hook) in the positive polarity. To demonstrate the rapid evolution of the footpoints moving along the positive polarity, the footpoints in the negative polarity are fixed. As the simulation progresses, the field lines exhibit a rapid slippage directed from the tip of the hook towards the the straight part of the current ribbon (panels (b), (e)). At the end of the slippage (panels (c), (f)), sheared flare loops joining the

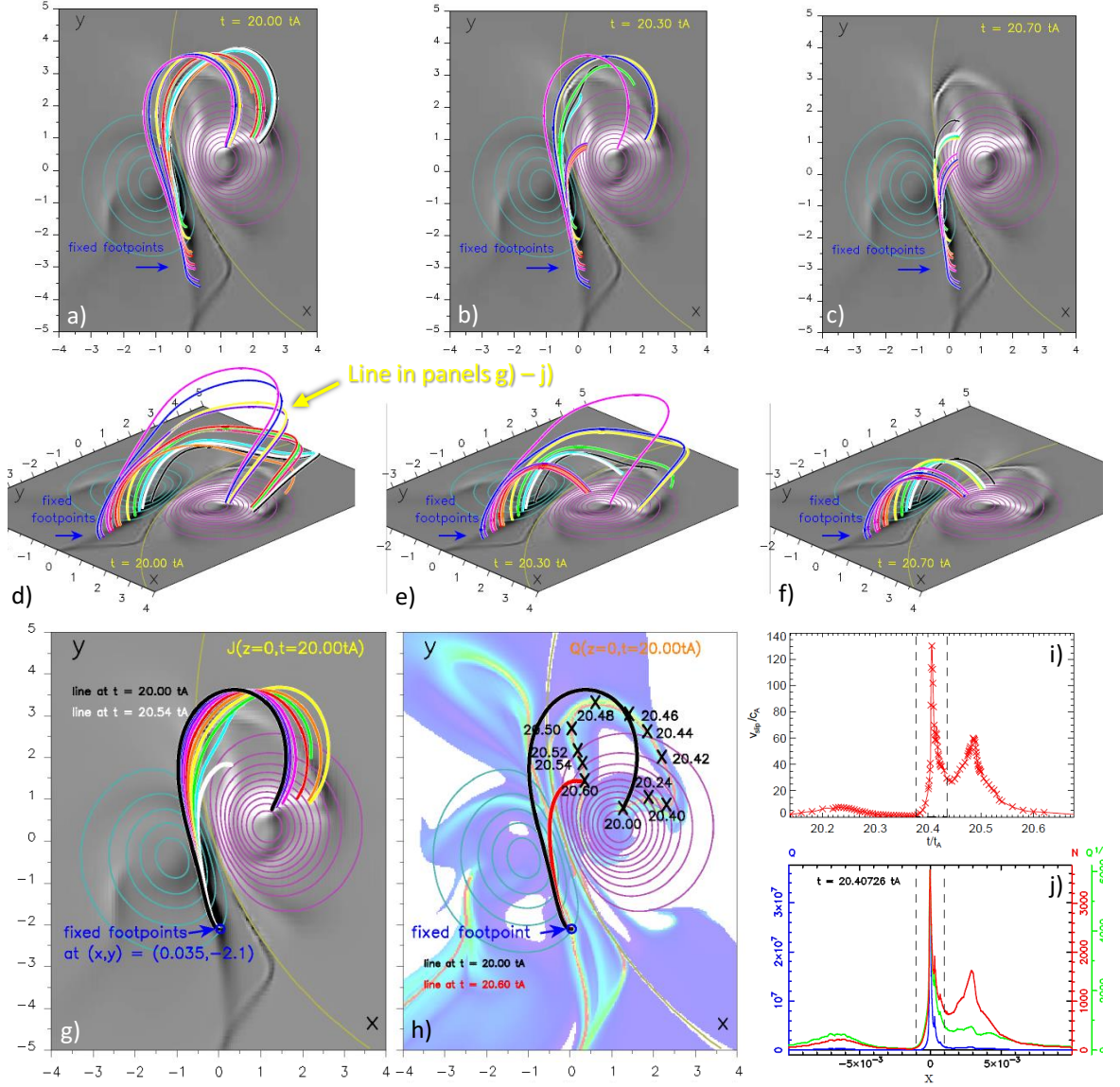


Figure 3.4: Magnetic slipping reconnection of field lines in the standard flare model in 3D. Panels (a) – (c) and (d) – (f) show the top and side views of field lines slipping along the  $J$ -shaped extension of the QSL footprint. Their footprints in the negative polarity are fixed. In panel (d), field line selected for further analysis in panels (g) and (h) is highlighted using the yellow arrow. The profile of the slipping velocity  $v_{\text{slip}}$  is presented in panel (i) and the variations of  $Q$ ,  $Q^{1/2}$ , and  $N$  are shown in panel (j). Adapted from Janvier et al. (2013), reproduced with permission © ESO.

straight parts of the current ribbons are visible (Janvier et al., 2013).

The slipping motion of an example line selected by Janvier et al. (2013), highlighted using the yellow arrow in panel (d), is plotted in panel (g). There, the color-coding was used to distinguish between the position of the line at different instants during the simulation. Locations corresponding to its footpoint, slipping along the positive-polarity ribbon, between the initial (black) and terminal (red) positions are marked using the  $\times$ -signs in panel (h). Their mutual distance is then used to measure the velocity of the slippage  $v_{\text{slip}}$  whose values, normalised to the Alfvén speed  $c_A$ , are presented in panel (i). Clearly,  $v_{\text{slip}}$  varies strongly, as it occurs at both sub- and super-Alfvénic speeds at different periods of the motion. The largest  $v_{\text{slip}}$  can be found between  $t_A = 20.4 - 20.5$ , when two strong peaks in the profile can be identified. On the contrary,  $v_{\text{slip}}$  is the lowest at the beginning and the end of the slippage. The authors related these strong variations to the displacement of QSLs during the eruption. The peak in  $v_{\text{slip}}$  is reached when the fixed footpoint is swept by a high- $Q$  region within QSL. Furthermore, the authors calculated the quantities measuring the distortion of the connectivity, namely  $N$ ,  $Q$ , and  $Q^{1/2}$ , along the path of the footpoint (panel (j)). A comparison of panels (i) and (j) reveals that the location of the main peak of  $v_{\text{slip}}$  corresponds to the peaks of  $N$ ,  $Q$ , and  $Q^{1/2}$ . Clearly, the overall distribution of  $v_{\text{slip}}$  is best matched by that of  $N$ . The authors found the two

quantities are closely related:

$$v_{\text{slip}}(t) = v_{\text{QSL}}N(t), \quad (3.7)$$

where  $v_{\text{QSL}}$  is the velocity of the displacement of QSL corresponding to the motion perpendicular to the PIL. It corresponds to the motion of ribbons in the direction perpendicular to the PIL (Dudík et al., 2016). The peak of  $v_{\text{slip}}$  thus depends on the peak of  $N$ , which can be infinitely high as the flux rope expands and QSLs become true separatrices. More precise determination of  $v_{\text{slip, peak}}$  would require a simulation with even higher high temporal resolution.

The slipping reconnection is manifested as apparent slipping motion of coronal or flare loops (see e.g., Section 4.1 in Janvier, 2017). The first observations of the slipping coronal loops were reported by Aulanier et al. (2007) in an active region observed by the X-ray Telescope (XRT; Golub et al., 2007) onboard the Hinode mission. This process was also consistent with observations of coronal loops in an active region which exhibited signatures of nanoflare heating observed by the Hi-C sounding rocket (Testa et al., 2013). Sun et al. (2013) reported signatures of the slipping reconnection in a null-point flare. The authors proposed that both the observed motion of hot flare loops within fan QSL and the progressive brightening of one of the ribbons were signatures of the slipping reconnection. An unambiguous identification of the slipping reconnection in a solar flare was provided by Dudík et al. (2014). The authors used SDO observations of an eruptive X-class flare from 2012 July 12. The apparent slipping motion of flare loops occurred along the observed ribbons in multiple locations and episodes, and in a similar morphology as predicted by the model. The observed slipping velocities reached several tens of  $\text{km s}^{-1}$ . The S-shaped loops which originated in the slipping reconnection participated in the eruption, vindicating the important theoretical prediction concerning the build-up of the erupting flux rope. Furthermore, the ribbons and their evolution were found to well-match the evolution of the photospheric footprints of QSLs modelled in a magnetic environment similar to the observed one. For the first time, the authors evidenced that signatures of the slipping reconnection can also be traced in flare kernels observed in filter channels sensitive to chromospheric and transition region plasma. The kernels were spatially coincident with footpoints of bright slipping flare loops. In another observation analysed by Dudík et al. (2016), the observed slippage occurred in both directions along both ribbons, as predicted by the standard flare model in 3D. Slipping flare kernels were also studied spectroscopically, which was made possible owing to high temporal, spatial, and spectral resolution of IRIS. Li and Zhang (2015a) reported redshifts of the Si IV 1402.77 Å line formed in

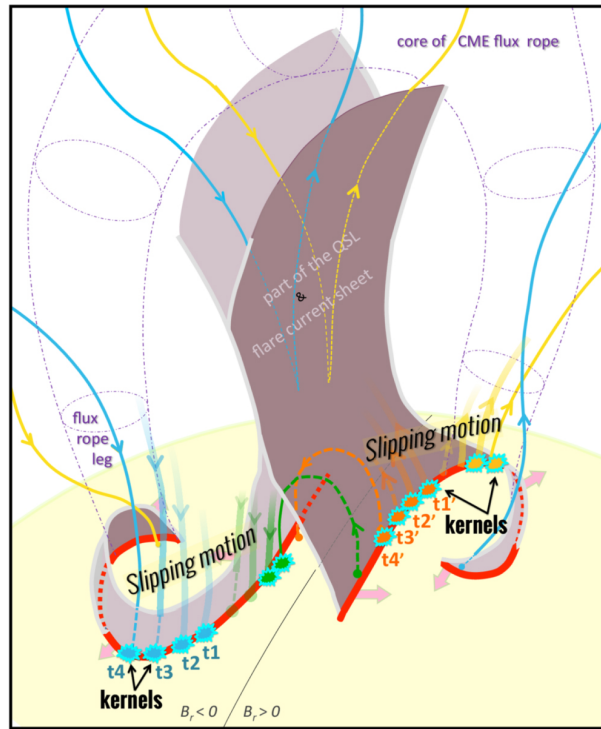


Figure 3.5: A cartoon demonstrating the magnetic slipping reconnection in the standard model of solar flares in 3D. The erupting flux rope (violet) is overlaid by the blue and yellow arcades. These field lines reconnect in the central part of the QSL. Below it, the slipping flare loops (green and orange) and kernels sequentially appear between times  $t_1 - t_4$  along the red current ribbons. Adapted from Dudík et al. (2016). © AAS. Reproduced with permission.

the transition region reaching  $70 \text{ km s}^{-1}$ . The widths of this line exhibited quasi-periodic variations in a fixed position along the analysed ribbon, which was interpreted as a signature of the slipping reconnection. The chromospheric evaporation during the slipping reconnection was investigated by Dudík et al. (2016). At the footpoints of the apparently-slipping flare loops, strongly-blueshifted (up to  $270 \text{ km s}^{-1}$ ) profiles of the Fe XXI  $1354.08 \text{ \AA}$  line forming at flare temperatures were discovered. These studies vindicated that apparently-slipping flare kernels are sites of the deposition of the energy which is consequently released via the chromospheric evaporation filling the apparently-slipping flare loops. This scenario is consistent with the basic picture of the energy deposition and release included in the CSHKP model. Our own analysis focused on variations of velocities of apparently-slipping flare kernels in regions of various magnetic connectivity is presented in Section 5.1.

A cartoon summarizing the theoretical predictions imposed on the slipping reconnection, confirmed by the observations listed above, is presented in Figure 3.5. This version, adapted from Dudík et al. (2016), is based on the original schematic figure of Janvier et al. (2014). In its central part, the core of QSL with a shape characteristic for HFT is shown. The erupting flux rope is indicated using dash-dotted violet lines. It is overlaid by the blue and yellow field lines which are reconnecting in the central part of QSL. Below the reconnected flux rope field lines, the green and orange flare loops are visible. Since the field lines reconnect in the slipping reconnection, the flare loops appear sequentially between the times  $t1 - t4$ . The same applies for the flare kernels corresponding to their footpoints, which appear along the red current ribbons located at either side of the PIL (grey). The ribbons are  $J$ -shaped (hooked), and their extensions encircle the footpoints of the CME flux rope. Last but not least, the semi-transparent pink arrows indicate the separation of the ribbons away from the PIL as well as the expansion of the hooks. As discussed in the following section, field lines which reconnect to produce slipping flare loops and kernels can be of different nature and rooted in different parts of QSLs.

### 3.2.3 Three-dimensional reconnection geometries

The standard flare model of solar flares in 3D was developed under the line-tied assumption, meaning that the footpoints of field lines originating from the photospheric bipole should not move in space (Forbes, 1990; Aulanier et al., 2010). Therefore, as long as the shearing motions of the photosphere are not taken into the account or the field lines do not reconnect with fields of neighboring flux concentrations, the footpoints of the erupting CME should be fixed in space. However, as is clear from the bottom row of Figure 3.3, the  $J$ -shaped current ribbons, encircling the legs of the CME, evolve in time. They exhibit the perpendicular motion away from the PIL (QSL displacement), in addition to the expansion and later contraction of the ribbon hooks. As the ribbon hooks expand, they cross (‘sweep’) footpoints of field lines in the domain, at which they enter QSLs (or leave them) and thus reconnect. As a result, a given location in the photosphere corresponds to different connectivity domains, as QSLs evolve during the eruption. This ‘sweeping’ of field line footpoints by the ribbons is an effective probe for investigating which field lines undergo magnetic reconnection.

The origin of field lines rooted in selected footpoints within the domain of the simulation of Zuccarello et al. (2015) was investigated by Aulanier and Dudík (2019). The standard model of solar flares in 3D contains three types of field lines which undergo the slipping reconnection; the coronal arcades ‘a’ which overlay the flux rope built by the ‘r’ lines, and finally the flare loops ‘f’. In Figure 3.5(a) the coronal arcade field lines are plotted using the green and orange colors. Field lines corresponding to flare loops, plotted in pink and green, can be identified below the erupting flux rope at the end of the simulation once the slippage is over (Figure 3.5(c)).

These field lines reconnect in three specific geometries:

- *aa-rf*: Two field lines from the overlying arcade ‘a’ reconnect into a new field line composing the flux rope ‘r’ and a flare loop ‘f’. The aa-rf reconnection is a 3D generalisation of the geometry included in the standard CSHKP model of solar flares.
- *rr-rf*: New flux rope field line and flare loop form when a flux rope field line reconnects with another flux rope field line. The pairs of flux rope field lines which endure this reconnection originated previously in the aa-rf reconnection. The two geometries therefore sometimes occur in a sequence, producing long, multi-turn field lines of the flux rope. As a result, the poloidal flux of the flux rope increases.
- *ar-rf*: Field line from the leg of the flux rope reconnects with field line from an inclined coronal arcade to form new flux rope field line and flare loop. This geometry will be discussed in detail, since its investigation was the objective of our publications (Lörinčík et al., 2019b; Dudík et al., 2019; Lörinčík et al., 2021a,b) presented in Section 5.

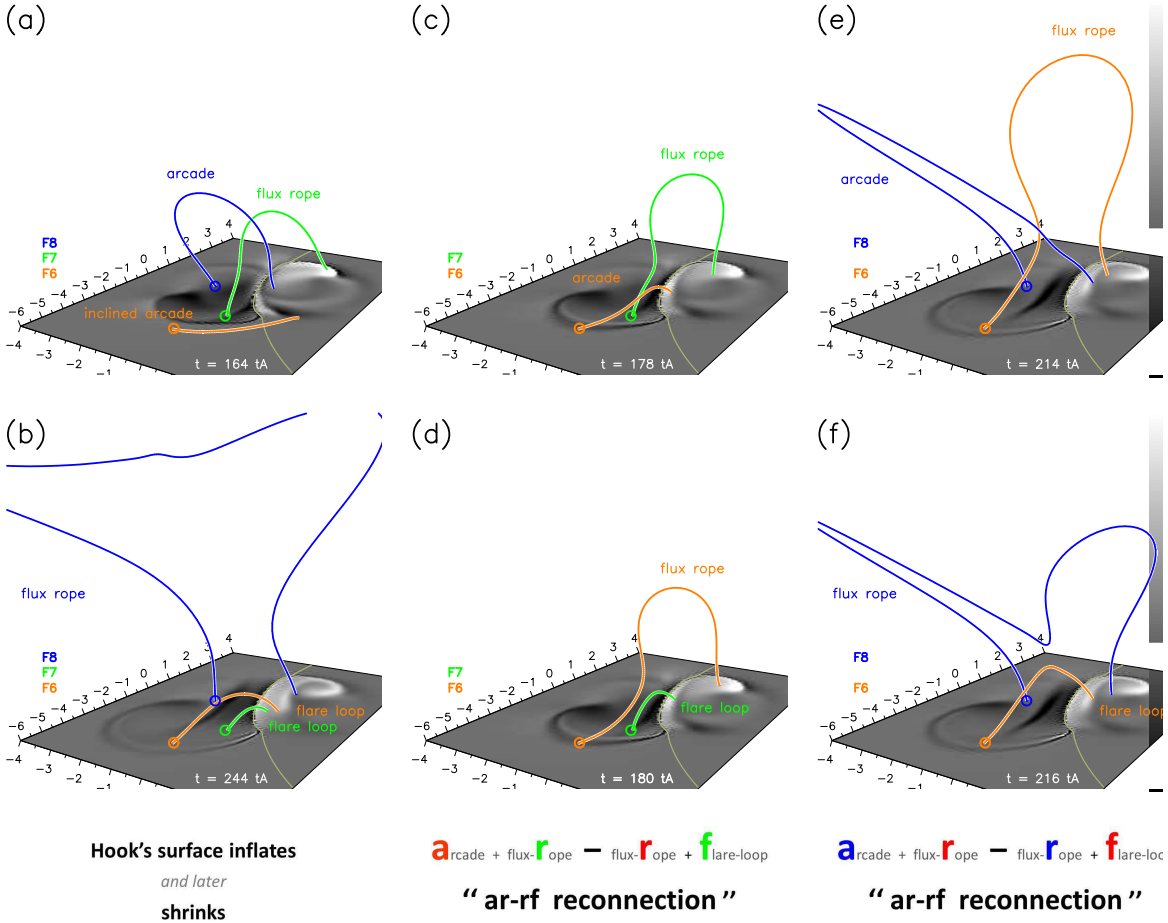


Figure 3.6: Field lines undergoing the ar-rf reconnection at the beginning (panel (a)) and end (panel (b)) of the simulation found at the footpoints F6 – F8. Panels (c), (e) and (d), (f) demonstrate how different pairs of field lines composing and overlying the flux rope change their connectivities to produce new flux rope field line and flare loop. The greyscale image at the bottom shows the photospheric traces of QSLs. Similarly as in previous figures, the brightest (resp. darkest) contours correspond to flare ribbons in the positive (resp. negative) polarity. Adapted from Aulanier and Dudik (2019), reproduced with permission © ESO.

The constituents of these geometries are usually associated with distinct parts of QSLs and therefore produce flare loops joining different portions of ribbons and ribbon hooks. The aa-rf and rr-rf reconnections occur below the erupting flux rope and produce flare loops joining the straight parts of the ribbons. The inclined arcades involved in the ar-rf reconnection are however rooted near the ribbon hook, leading to the formation of relatively-longer flare loops stretched between the hook of one ribbon and the straight part of the conjugate ribbon.

A schematic of the ar-rf reconnection is presented in Figure 3.6. Panel (a) contains three constituent magnetic field lines of this geometry before the reconnection occurs; the low-lying orange line from the inclined arcade overlying the leg of the flux rope, the green field line of the flux rope, and the blue arcade line above the central part of the flux rope. The footpoints of the orange, green, and blue field lines, denoted F6– F8, respectively, are indicated using the colored circles.

First, the orange inclined arcade slips along the ribbon to become the arcade field line visible in panel (c). This reconnection is however not directly related to the evolution of the erupting flux rope. Meanwhile, the surface of the hook inflated and the line’s footpoint (orange circle) entered the reconnection region. Between  $t_A = 178$  and 180 (panels (c) and (d)), the first episode of the ar-rf reconnection occurred. As a result, the connectivity of the orange arcade and green flux rope field lines changed, leading to the formation of a small flare loop (green field line) and a new flux rope field line (orange). This new flux rope field line is a part of the eruption, and is being stretched outward. As the eruption was already underway and the field lines were rapidly expanding, another episode of the ar-rf reconnection occurred between  $t_A = 214$  and 216 (panels (e), (f)). It involved the orange flux rope field line and the blue arcade field line plotted in panel (e) and led to the formation of the longer flare loop (orange) and the blue flux rope field line (panel (f)). The post-reconnection state is

presented in panel (b). The flare loops rooted in the hook are overlaid with the high flux rope field line anchored at the very tip of the hook. A comparison of the panels (a) and (b) reveals what types of field lines do the footpoints F6 – F8 correspond to. The footpoint F6, in which the (inclined) arcade used to be rooted, hosts the relatively-longer flare loop. The footpoint F7, in which the pre-reconnection flux rope was rooted, corresponds to the relatively-shorter loop which reconnected earlier on. In the footpoint F8 located at the tip of the hook, the flux rope field line can be found, as opposed to the overlying arcade before the reconnection occurred. The evolution of the field lines anchored in either F6 or F8, combined with F7, thus indeed follows the ‘arcade + flux rope → flux rope + flare loop’ sequence.

According to Figure 3.6, while the field line rooted in the footpoint F7 turned to the flare loop after one episode of the ar–rf reconnection, two reconnections were needed for F6 to host the flare loop. This footpoint first corresponded to the arcade (panel (c)), then to the flux rope (panel (d)), and finally to the flare loop (panel (f)). This progressive change of connectivity is a signature of the sequential ar–rf reconnection. Aulanier and Dudík (2019) found that the modelled ribbon hook indeed swept the footpoint F6 on two occasions. This indicates that field lines rooted in certain regions at the solar surface can become a part of the flux rope and then leave it again, which is manifested by the back-and-forth motion of the ribbon hook (Figure 3 therein).

The most interesting property of the ar–rf reconnection is the prediction regarding the temporal evolution of field lines composing the flux rope. As the eruption progressed, the flux rope footpoint continuously shifted from the footpoint F7 to F6 and finally to F8 (3.6(c), (d), (f)). Evidently, the flux rope’s footpoints shift further away along the hook. This means that the footpoints of the flux rope are displaced over time, and drift across the solar surface, as they undergo ar–rf reconnections.

The first observational candidate for the ar–rf reconnection was found in an analysis of eruption of a hot channel (Zemanová et al., 2019). One of the hooks which formed during the analysed eruption drifted for several tens of arc seconds. The drifting hook also expanded and subsequently contracted again, during which it swept coronal loops rooted in the vicinity. Even though the erupting flux rope was not entirely visible in the observations of Zemanová et al. (2019), such evolution was consistent with the predictions imposed for the sequential ar–rf reconnection. Study of the 3D magnetic reconnection geometries, mainly the ar–rf geometry, is among the main results of this work. These are described and attached in Section 5 and summarized in four peer-reviewed publications (Lörinčík et al. (2019b); Dudík, Lörinčík et al. (2019); Lörinčík et al. (2021a); Lörinčík et al. (2021b)).

The ar–rf reconnection was also discussed in studies which were not primarily focused on the reconnection geometries included in the standard flare model in 3D (Aulanier and Dudík, 2019). For example, it has been suggested that the ar–rf reconnection caused the drift of the hot channel’s footpoints discussed in Chen et al. (2019). Further, Xing et al. (2020) reported on observations of drifting of footpoints of CMEs associated with multiple flares observed by SDO. According to Hou et al. (2020) the ar–rf reconnection can be associated to the ‘external’ reconnection which they observed above the erupting flux rope. Most recently, a reconnection geometry corresponding to the ar–rf reconnection has been reported in a 3D MHD simulation of a solar eruption of Wang et al. (2021). The fact that this process has been discovered independently in two different models of solar eruptions means that reconnection between erupting structures and field lines rooted at peripheries of regions associated with eruptions are likely generic. We finally note that the ar–rf reconnection is consistent with magnetic reconnection between field lines composing erupting flux ropes and surrounding corona, reported in several other observational studies aimed at morphology of solar flares and eruptions (e.g., Cohen et al., 2010; Grechnev et al., 2015; Li et al., 2016).



# 4. Instruments and data

If it weren't for imaging observations of solar flares in UV and EUV, acquired at as high temporal and spatial resolutions as possible, study of magnetic reconnection would not be possible. In this work we primarily used data acquired by the Atmospheric Imaging Assembly (AIA) and the Helioseismic and Magnetic Imager (HMI), both onboard the Solar Dynamics Observatory. Where needed, datasets of AIA were supplemented by observations of other instruments, such as the X-ray telescope of the Hinode mission, the Extreme Ultraviolet Imager (EUVI; Wuelser et al., 2004) onboard STEREO-B, and the Large Angle and Spectrometric Coronagraph (LASCO) onboard the Solar and Heliospheric Observatory (SOHO).

## 4.1 Solar Dynamics Observatory

The Solar Dynamics Observatory is a NASA mission launched on February 11, 2010 and on May 1 it started to regularly deliver scientific data. The main goals of the project are aimed at our understanding of the solar magnetic field and its variations during the solar cycle. SDO is placed in a geosynchronous orbit and possesses extremely accurate pointing and stability, allowing for continuous observations of the Sun. Observed data are transmitted to the Earth which permits their nearly immediate usage for example for predicting of the space-weather (Pesnell et al., 2012). The scientific mission of SDO was originally planned for five years. Owing to additional propellant carried by the spacecraft, its operations were secured for a much longer period. Nowadays, more than 11 years after its launch, the instrumentation onboard SDO still provides science-ready data widely used in the research of the Sun. Apart from AIA and HMI, which we describe in the following section, SDO carries the Extreme Ultraviolet Variability Experiment (EVE; Woods et al., 2012). EVE is composed of multiple instruments measuring the EUV irradiance of the Sun in a band pass of 1 – 1050 Å. It has a spectral resolution of roughly 1 Å and a cadence of 10 s.

### 4.1.1 Atmospheric Imaging Assembly

AIA was the key instrument used in this work. This instrument consists of four dual-channel telescopes with a 20 cm aperture and a focal length of 4.125 m, designed for narrow-band imaging of the solar atmosphere in EUV and UV domains of the spectrum. The field of view (FOV) of AIA is  $41' \times 41'$ , enough to observe the entire solar disk. The CCD detectors contain  $4096 \times 4096$  pixels with a physical and projected size of 12  $\mu\text{m}$  and 0.6", respectively (Lemen et al., 2012).

The telescopes operate in 7 EUV filter channels (hereafter 'channels') at 94 Å, 131 Å, 171 Å, 193 Å, 211 Å, 304 Å, and 335 Å. The remaining band pass is left for two UV channels at 1600 Å, 1700 Å, and one visible-light channel at 4500 Å which serves for co-alignment with other telescopes. In the standard operating mode, the exposure times of these channels range between 1 and 3 s. However, when flares occur on the Sun, these times are substantially shortened by the automatic exposure control to reduce image saturation. The spatial resolution of AIA depends on the channel and was predicted to range between  $\approx 1.4''$  (193 Å) and  $\approx 2.4''$  (4500 Å) (Boerner et al., 2012). The cadence of the 94 – 335 Å channels is 12 s, while that of the 1600, 1700, and 4500 Å channels is 24 s. The combined effect of the high cadence and resolution of the images is an immense stream of observational data, reaching up to 2 Terabytes per day.

#### 4.1.1.1 AIA temperature responses

The channels of AIA are centred on specific lines of different ions, primarily of iron, allowing to observe plasma at a broad range of temperatures spanning between  $\approx 6 \times 10^4$  K and  $\approx 2 \times 10^7$  K. Each channel has its own characteristic temperature, derived from the formation temperature of the primary line observed by each channel (see Table 1 in Lemen et al., 2012).

The coolest plasma observed by AIA is observed in the photospheric continuum contributing to the 1700 Å and 4500 Å channels with  $\log(T [\text{K}]) = 3.7$ . Next, AIA contains the 304 Å channel, centred at the two 303.8 Å lines of He II formed at  $\log(T [\text{K}]) \approx 4.7$  in the chromosphere and the transition region. The transition region can also be studied via the 1600 Å channel focused at the resonance lines of C IV at 1548 Å and 1550 Å formed at  $\log(T [\text{K}]) \approx 5$ . Plasma of the upper transition region further contributes to the 171 Å channel. The primary line of this channel is the Fe IX 171.1 Å line ( $\log(T [\text{K}]) = 5.8$ ), which makes the channel useful for imaging of the solar corona. AIA also observes coronal emission originating in the strong 192.4 Å, 193.5 Å, and 195.1 Å lines of Fe XII often utilised

in coronal diagnostics (see the review of Del Zanna and Mason, 2018). These lines also contribute to the emission of plasma imaged by the 193 Å channel ( $\log(T \text{ [K]}) = 6.2$ ). Active-region corona is observed in the 211 Å and 335 Å channels, containing the Fe XIV 211.3 Å line ( $\log(T \text{ [K]}) = 6.3$ ), and the Fe XVI 335.4 Å line with  $\log(T \text{ [K]}) = 6.4$ . Finally, the 94 Å ( $\log(T \text{ [K]}) = 6.8$ ) and 131 Å ( $\log(T \text{ [K]}) = 7.0$ ) channels observe the hot 93.9 Å and 128 Å lines of Fe XVIII and Fe XXI, respectively, which are usually used to investigate solar flares.

Wavelength responses, given by the effective areas of each channel, are typically a few angstrom or tens of angstrom broad. Therefore, apart from the primary ones, additional lines contribute to the emission observed by the channels of AIA. These lines often belong to ions of various elements which form in different physical conditions. For this reason, the temperature sensitivity of some of the channels spans more than two orders of magnitude. The temperature responses of each filter are plotted in Figure 4.1. These functions were calculated by Dudík et al. (2014) using the CHIANTI database, v7.1 (Landi et al., 2012; Dere et al., 1997) for  $\log(N_e \text{ [cm}^{-3}\text{]}) = 9.0$  and the abundances of Schmelz et al. (2012).

The emission of plasma associated with different structures of the solar corona, contributing to the EUV channels of AIA, was first investigated by O’Dwyer et al. (2010). For example, the quiet-Sun and coronal hole emission observed in the 94 Å channel is dominated by the 94.0 Å line of Fe X. The peak formation temperature of this line is  $\log(T \text{ [K]}) = 6.05$ , which is manifested in the presence of the left peak of the green curve in Figure 4.1. Del Zanna (2013) found that in active region observations, this channel contains a considerable contribution from the 93.6 Å line of Fe XIV as well as lines of Fe XII. In quiet corona, the 131 Å channel (cyan line) has a strong contribution of two Fe VIII ( $\log(T \text{ [K]}) = 5.6$ ) lines at 130.9 Å and 131.2 Å. Flare emission observed in the 193 Å channel is dominated by the Fe XXIV 192.03 Å line which formation temperature corresponds to  $\log(T \text{ [K]}) = 7.25$ , visible as the right peak of the brown curve (Figure 4.1). The temperature response of this channel exhibits a broad plateau, which is due to a presence of multiple numerous lines of Fe IX – Fe XIII with formation temperatures between  $\log(T \text{ [K]}) = 5.85$  and 6.25 (Dzifčáková et al., 2015). Note that below  $\log(T \text{ [K]}) \approx 6.5$ , the general trend showed by the purple curve, standing for the 211 Å channel, is very similar to that of the 193 Å channel. The peak of its temperature response is however shifted to slightly higher temperatures, which is caused by the higher formation temperature of Fe XIV compared to Fe XII. Analysis of active region spectra presented by Del Zanna et al. (2011) shown that more than 50% of spectral lines emitting at wavelengths observed by this channel are unidentified. Among other lines, the authors were capable of identifying lines of ions such as Cr VIII and Fe VIII. The low-temperature peak of the 304 Å channel response, plotted using the red curve, corresponds to the He II doublet. The peak at  $\log(T \text{ [K]}) = 6.2$  is due to the Si XI 303.33 Å line emission in active regions. In the temperature range from  $\log(T \text{ [K]}) \approx 4.8$  to 6.8, the broad response of the 335 Å channel (blue curve) exhibits three peaks. The right one corresponds to the Fe XVI line ( $\log(T \text{ [K]}) = 6.45$ ) forming in flares and hot cores of active regions (Warren et al., 2011a). The middle peak at  $\log(T \text{ [K]}) \approx 5.8$  comes from lines of ions such as Si VIII, Si IX, Mg VIII, Al X, Fe X, and Fe XIV, forming between  $\log(T \text{ [K]}) = 5.8$  and 6.3. Finally, the low-temperature peak ( $\log(T \text{ [K]}) \approx 5.2$ ) of the response function is due to off-band contribution of lines of the transition region.

#### 4.1.1.2 Processing of AIA data

Raw data observed by AIA are labelled as Level 0. The Level 0 data contain counts recorded by CCD cameras stored as integers in two-dimensional grids consisting of  $4096 \times 4096$  pixel for each exposure. After being recorded by the instrument, they are transmitted to the Earth where they are permanently stored in the Joint SDO Operations Center (JSOC) facility of the Stanford University. The Level 0 data are then converted to calibrated data products of Level 1 via an automated processing pipeline. It consists of five principal steps (Section 5 in Lemen et al., 2012):

1. Data are first cleared of ‘overscan’ regions. This term is used for rows and columns of CCD cameras which are not exposed to the sunlight, but used for the estimation of the dark current.
2. Dark current, CCD read noise, and the digital offsets of the cameras are removed.
3. A flat-field correction is applied. In this process, images are corrected for non-uniformities of the detector, differences of gain in different quadrants of CCD cameras, vignetting, and shadowing caused by the components in the optical path.
4. Images are cleared of bad pixels – pixels which do not respond correctly to the detected light. Their values are interpolated from those of the neighboring pixels. In the same step, data are ‘de-spiked’, i.e., cleared of pixels whose counts are much higher than what normally would be expected assuming the instrument’s point-spread function. Such pixels originate e.g., when

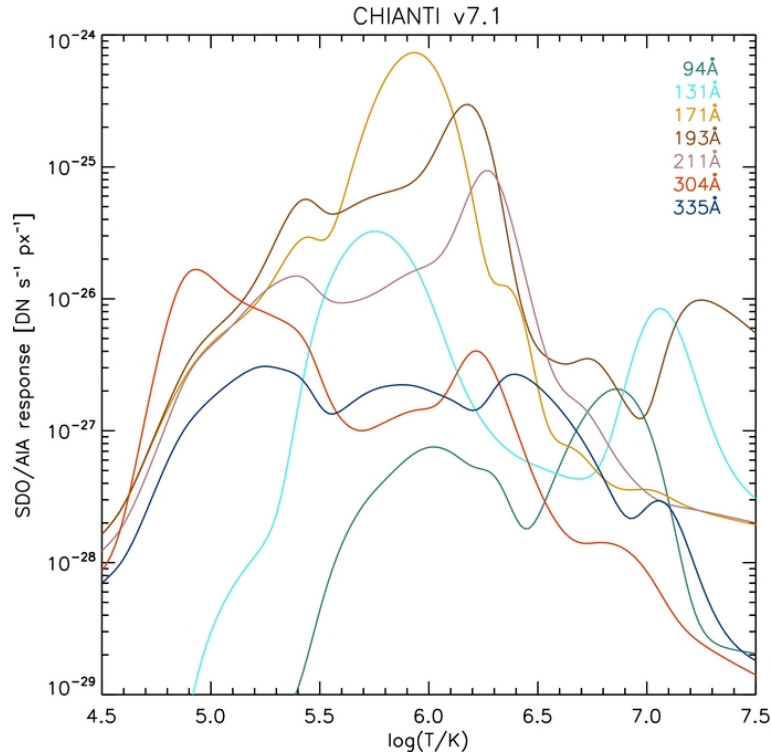


Figure 4.1: Temperature response functions of EUV filter channels of SDO/AIA. Adapted from Dudík et al. (2014). © AAS. Reproduced with permission.

high-energetic particles hit either directly the pixels of the CCD cameras, or the satellite. After the identification, their values are replaced by the median value of the neighboring pixels.

5. Data are flipped in order to place the solar north to the top of the data array. Finally, the metadata accompanying each image are updated for key information about observation.

The Level 1 data, stored in Flexible Image Transport System (FITS) files, can be accessed at various servers. For example, the datasets analysed in this work were acquired via the Virtual Solar Observatory (VSO) service provided by JSOC. The Level 1 data are further usually promoted to Level 1.5. In this process, the plate-scale, the projected spatial extent of the pixels in each channel, is adjusted to a common size of  $0.6''$ . Data are then rotated to a projection in which the solar north is at  $0^\circ$ , what corresponds to the top of the image. Finally, the correction for the misalignment between the four telescopes of AIA is applied. The conversion from the Level 1 to the Level 1.5 can be performed using e.g., the `aia_prep.pro` routine included within the SolarSoft package of Interactive Data Language (IDL). This function has recently been also implemented in the SunPy package dedicated for analysis of solar data using Python (SunPy Community et al., 2020).

The data processing pipeline we employed in this work consisted of several additional steps. Datasets from the EUV channels were corrected for the stray light using the method of Poduval et al. (2013), which implements a fast Fourier transform. Further, a correction for the exposure times was applied. By dividing integer intensities stored in data-number (DN) per pixel by the exposure times of each channel, floating point precision intensities in  $\text{DN s}^{-1} \text{pix}^{-1}$  were obtained. Where necessary, additional co-alignment between the channels and the correction for the differential rotation of the Sun were applied.

#### 4.1.2 Helioseismic Magnetic Imager

HMI is aimed at mapping magnetic and velocity fields at the solar surface. The design of HMI is largely based on its predecessor, the Michelson Doppler Imager (MDI; Scherrer et al., 1995) of SOHO. Its refracting telescope with an aperture of 140 mm observes the full disk of the Sun in a narrow band centred at the  $6173 \text{ \AA}$  line of Fe I (Schou et al., 2012). Observations of this line are used for derivation of the physical observables which are contained in the Level 1.5 data products (Scherrer et al., 2012). The measurements from HMI are stored in a grid of  $4096 \times 4096$  pixels. They can therefore easily be compared to the imaging observations of AIA.

In order to calculate the velocities of flows in the photosphere, the Doppler shifts of the 6173 Å line are measured. Resulting velocity maps have a two-pixel resolution of 1", cadence of 45 s, and the noise level of roughly  $17 \text{ m s}^{-1}$ . Magnetic field strength is measured via the Stokes parameters inferred from observations of the Zeeman effect of the same line. HMI produces two different data products related to the photospheric magnetic field. The first are the full-disk measurements of the line-of-sight (longitudinal) component of the magnetic field. The second are vector magnetograms recovered in selected regions of a smaller spatial extent. HMI is the first instrument to continuously observe the strength of the solar magnetic field at a high cadence. The temporal resolution of the longitudinal and vector magnetograms is 45 s, and 720 s, respectively, and their two-pixel spatial resolution is again 1". The uncertainty of the measurements of the longitudinal component reaches 7 G, while that of the vector magnetograms is roughly 3 G only (Couvidat et al., 2016).

For purposes of our study, observations of the longitudinal component of the magnetic field strength were sufficient. Series of the Level 1.5 HMI data were obtained via the VSO and processed using the `aia_prep.pro` routine. If necessary, data were corrected for the differential rotation.

## 4.2 Other instruments

### 4.2.1 The X-ray Telescope

The X-ray Telescope is an X-ray imaging instrument onboard the Hinode satellite operating since 2006. Hinode is a mission of the Japan Aerospace Exploration Agency (JAXA) constructed in collaboration with NASA and the United Kingdom. A complete description of the instrument was provided by Golub et al. (2007).

XRT is a grazing incidence telescope operating in a wavelength range of 6 – 60 Å, corresponding to the soft X rays. The instrument's focal length is 2.7 m and its entrance diameter is  $\approx 34 \text{ cm}$ , leading to FOV of 35'. The instrument is primarily designed for observations of selected regions of the solar atmosphere at a spatial resolution of 2". In front of its CCD camera composed of  $2048 \times 2048$  pixels, two wheels containing nine focal plane filters for different X-ray passbands are installed. The filters were built using different materials and their thickness varies by a factor of  $10^4$ . The thinnest filters, such as the Al-poly filter whose thickness is 1250 Å, are used for observations of faint targets. On the other hand, thick filters like the Be-thick filter ( $3 \times 10^6 \text{ Å}$ ) are employed for imaging of bright objects. Owing to the design of its filters, XRT is sensitive to plasma radiating at a broad range of temperatures, ranging from  $\log(T [\text{K}]) = 6.1$  to  $\log(T [\text{K}]) = 7.5$ . This makes XRT an ideal instrument for studies of hot plasma of active regions and flares as well as processes occurring therein. Exposure times of XRT range between  $4 \times 10^{-3} \text{ s} - 10^1 \text{ s}$  and the highest possible cadence of the instrument is 2 seconds.

The XRT data used in this work were downloaded from the DARTS archive of Hinode data. The data were first processed using the `xrt_prep.pro` and `xrt_jitter.pro` routines available within the SolarSoft package. Data were then manually co-registered with AIA. This was done using observations of hot plasma observed in the 131 Å channel, where the morphology of flare loop arcades and flare ribbons agreed to that observed by XRT.

### 4.2.2 Extreme Ultraviolet Imager

EUVI is one of five telescopes of the Sun Earth Connection Coronal and Heliospheric Investigation (SECCHI) instrument onboard STEREO. STEREO is a NASA mission consisting of two nearly-identical spacecrafts launched in 2006. STEREO-A (after 'ahead') orbits the Sun faster than the Earth while the other, STEREO-B (after 'behind'), is slower than the Earth for which the two spacecrafts separate from each other. The mean rate of the separation is roughly  $44^\circ$  per year. Up until 2014, when the contact with STEREO-B was lost due to a pointing malfunction, the spacecrafts had been providing stereoscopic images of the Sun. Furthermore, the telescopes comprising SECCHI were designed to image the Sun, the corona nearby, and the heliosphere all the way up to  $R_\odot \approx 318$  (Howard et al., 2008).

The light gathered by the telescope with a focal length of 1.75 m and an aperture of 98 mm is splitted to four EUV filter channels of the instrument: the 171 Å, 195 Å, 284 Å, and 304 Å. The passbands of EUVI have widths of 14 – 30 Å, centred at selected field lines of different ions. The main lines contributing to the 171 Å and 304 Å channels of EUVI are the same as those of the 171 Å and 304 Å channels of SDO/AIA (Section 4.1.1.1). The 195 Å channel is centred at the 195.1 Å line of Fe XII. The main contribution to the 284 Å channel originates in the very strong and relatively-isolated 284.2 Å line of Fe XV. The CCDs of EUVI consist of  $2048 \times 2048$  pixels with a projected scale

(resolution) of 1.6". In FOV of EUVI, the entire solar disk as well as corona extending to  $R_{\odot} \approx 1.7$  are imaged (Wuelser et al., 2004).

EUVI data were obtained from the Multi Experiment Data & Operation Center (MEDOC) service. EUVI data were processed using the standard `secchi_prep.pro` routine in SolarSoft and then manually co-aligned with AIA. To do so, observations of coronal loops from the 171 Å channels of both instruments were used.

### 4.2.3 Large Angle and Spectrometric Coronagraph

LASCO is a package of three coronagraphs mounted on the SOHO spacecraft. The SOHO mission, operating since 1996, recently celebrated 25 years of its existence. Despite the fact that the project was originally planned for two years only, some instruments, including LASCO, are still delivering scientific data. Even though the coronagraph C1 was lost due to a malfunction in 1998, coronagraphs C2 and C3 are operational, providing observations of CMEs (Section 2.1.3.1).

Coronagraphs C2 and C3 observe the white light corona spanning between  $R_{\odot} = 1.5 - 6$  and  $R_{\odot} = 3.7 - 30$ , respectively (Brueckner et al., 1995). Their CCD cameras consist of  $1024 \times 1024$  pixels which projected sizes are 11.4" and 56".

LASCO data were acquired from the VSO, corrected for flat-field, and co-registered to a common grid of coordinates, all using routines available within SolarSoft.



# 5. Results

Our results are summarized in five peer-reviewed publications. In the following sections, the published versions of these articles are attached. At the beginning of each section, we provide a brief description of the main results in each of the works, accompanied by salient figures. In Section 5.1, we analysed velocities of slipping flare kernels in observations of an eruptive flare and their relation to the standard flare model in 3D (Lörinčík et al., 2019a). In Section 5.2, containing results of Lörinčík et al. (2019b), we focus on a conversion of filament strands to flare loops, interpreted in terms of the three-dimensional ar–rf reconnection. Observational analysis of all pre- and post-reconnection constituents partaking in the ar–rf and rr–rf reconnection geometries (Dudík, Lörinčík et al. (2019)) is presented in Section 5.3. Section 5.4 details the first imaging evidence for outflows of plasma from a coronal dimming (Lörinčík et al., 2021a). The role of the ar–rf reconnection in the spatial expansion of the dimming region is discussed. In our last publication (Lörinčík et al., 2021b, Section 5.5), we describe observations of saddle-shaped arcades of flare loops and address their formation as a consequence of the ar–rf reconnection. A summary of the results is provided in Section 6.1.

## 5.1 Velocities of flare kernels and their relation to QSL properties

In Lörinčík et al. (2019a) we studied signatures of the magnetic slipping reconnection in the motion of flare ribbon kernels. Their observed dynamics was consequently studied in relation to the standard flare model in 3D.

The first event we analyse here is the ‘textbook’ 2012 August 31 eruption of a quiescent filament (see the cover of Priest (2014) as well as our Figure 1.1). The eruption was accompanied by a C-class flare. We used observations acquired by AIA and measurements of magnetic field from HMI, both onboard the SDO satellite. As the filament started to erupt, a pair of *J*-shaped (hooked) flare ribbons formed (Figure 5.1(a)). To identify the magnetic polarity of the ribbons, we used measurements of the line-of-sight component of the magnetic field  $B_{\text{LOS}}$  from HMI. As is clear from panel (b) of Figure 5.1, the ribbon ‘NR’ was spatially coincident with regions of the negative polarity flux while the other, ‘PR’, was associated with concentrations of the positive flux. Along the hooked extension of NR (‘NRH’), slipping flare loops were observed in the 131 Å channel of AIA (Figure 2 in Lörinčík et al., 2019a). The velocity of the apparent slipping motion of  $\approx 24 - 85 \text{ km s}^{-1}$  was measured using time-distance diagrams based on artificial cuts that we placed perpendicularly to the direction of the motion of the loops. At the footpoints of the slipping flare loops, slipping flare kernels were visible in the 304 Å and 1600 Å channels of AIA. Positions of the individual kernels, defined as high-intensity contours moving along the ribbons, were obtained using a method for calculating the average intensity-weighted position of each contour. The acquired positions were consequently utilised to estimate the distance the kernels moved and calculate their velocities.

The velocities of the kernel slippage measured near the tip of the ribbon hook (Figure 5.1(c)), analysed within ‘Case 1’, reached  $v_{\parallel} = 40 - 46 \text{ km s}^{-1}$  and were thus similar to those of the slipping flare loops. Another flare kernel was observed to slip along the elbow of NRH towards its tip. The slipping velocity of this kernel of ‘Case 2’ (panel (g)) was much higher, up to  $v_{\parallel} = 254 \text{ km s}^{-1}$ . The velocity of this kernel was also measured using the time-distance diagram constructed along its path with the 304 Å data which cadence is higher compared to the 1600 Å. As is clear from Figure 5.1(i), the kernel initially passed a short distance at  $v_{\parallel} = 70 \text{ km s}^{-1}$  and later it accelerated to nearly  $300 \text{ km s}^{-1}$ . Furthermore, a series of kernels of ‘Case 3’, shown in panel (e), was observed along the elongating ribbon PR. These slipped at the highest velocities  $v_{\parallel}$  of nearly  $450 \text{ km s}^{-1}$ . By analysing strengths of the underlying magnetic field, we found that the relatively-slower kernels of Case 1 moved across concentrations of a relatively-higher flux ranging between  $|B_{\text{LOS}}| \approx 30 \text{ G}$  and  $|B_{\text{LOS}}| \approx 130 \text{ G}$  (panel (d)). In contrary to that, fast kernels of Cases 2 and 3 occurred in weak field regions where  $|B_{\text{LOS}}| < 10 \text{ G}$  (panels (f), (h)). A detailed examination of the photospheric magnetic field in the vicinity of Case 3 revealed a parasitic polarity (Figure 8(c) Lörinčík et al., 2019a). As shown e.g., by Masson et al. (2009), these are known to affect local magnetic topology.

Our analysis indicated that  $v_{\parallel}$  and  $|B_{\text{LOS}}|$  were closely related, which we examined in observations of Case 1. To do so, we investigated how did the velocities of kernels vary between individual segments of their paths with respect to the strengths of the adjacent magnetic field. Our results indicated that the two quantities were anti-correlated (Figure 5(d), (e) in Lörinčík et al., 2019a), in line with results of previous studies focused on measurements of electric currents in flare ribbons and kernels (e.g., Jing

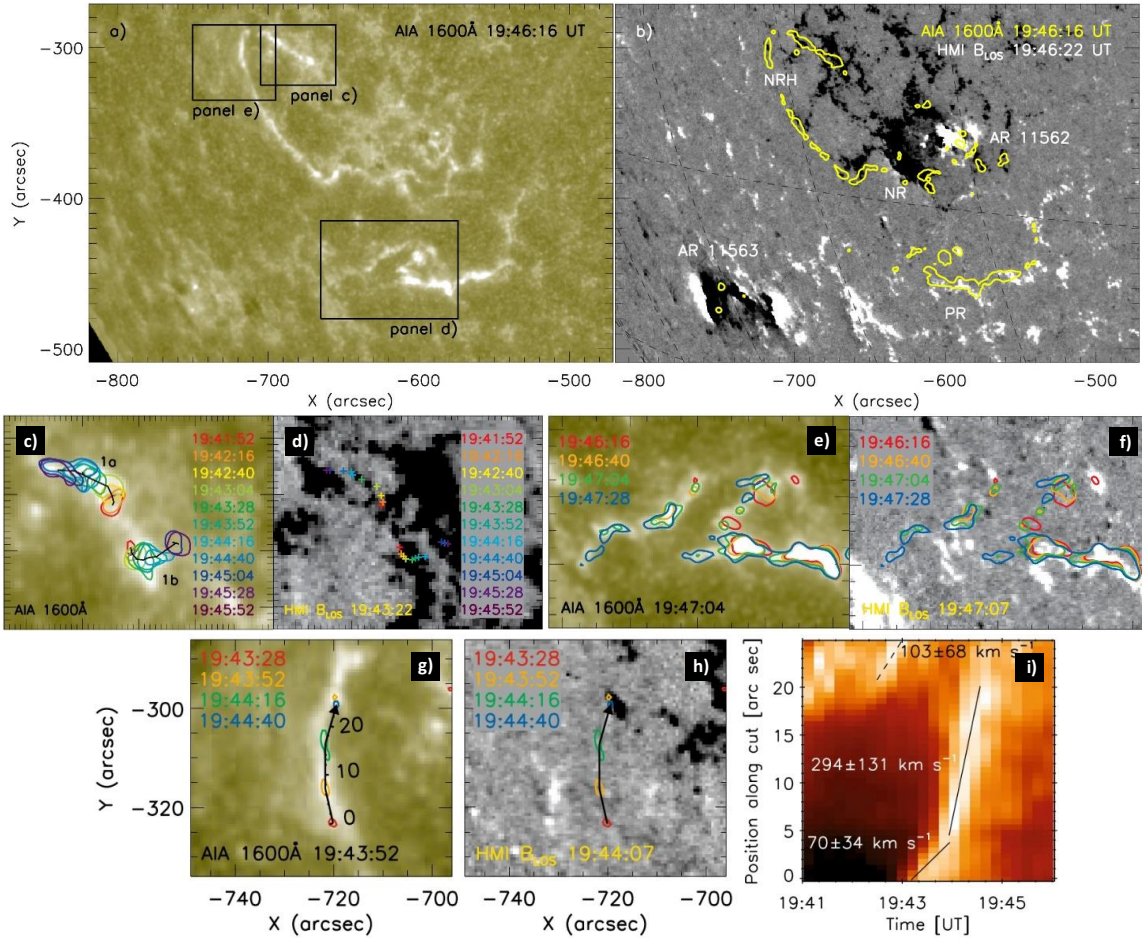


Figure 5.1: Analysis of slipping flare kernels during the 2012 August 31 filament eruption. Panel (a) presents observations of flare ribbons carried out in the 1600 Å channel of SDO/AIA. Contours of the ribbons (yellow) are also plotted in panel (b), atop of  $B_{\text{LOS}}$  measured by SDO/HMI. In the same panel, active regions located in the vicinity of the flare are indicated. Panels (c), (e) (or (d), (f)) show slipping flare kernels analysed in Cases 1 and 3 in the 1600 Å channel of AIA (or plotted atop of measurements of  $B_{\text{LOS}}$ ). The colored contours (or symbols) correspond to the kernels at different times. The kernel of Case 2 is plotted in the bottom row (panels (g), (h)). On the right-hand side, a time-distance diagram depicting the motion of this kernel in the 304 Å channel is shown.

et al., 2008; Qiu et al., 2017; Hinterreiter et al., 2018).

The ties between  $v_{\parallel}$  and  $|B_{\text{LOS}}|$  were then investigated using the standard flare model in 3D. The magnetic environment of the simulated eruption qualitatively corresponded to the observed one. While the tip of the ribbon hook representing NRH was located in a strong-field region, the rest of the hook was located in weak magnetic fields. Further, to the conjugate polarity of the bipole, a small sub-photospheric source of the flux was introduced, producing a weak oppositely-oriented flux at the photosphere (Figure 9(c) in Lörinčík et al., 2019a). We used the TOPOTR code to calculate the spatial distribution of the mapping norm of field line connectivity  $N$ , a quantity proportional to the velocity of the apparent slipping motion of magnetic field lines (Equation 3.7).

We found a good agreement between the spatial distribution of  $N$  and the measured velocities of the flare kernels. As indicated in Figure 9(d) in Lörinčík et al. (2019a), high values of  $N$  were recovered in weak-field regions where the kernels were the fastest. These were found e.g., in the elbow of NRH extending out from the simulated bipole and near the parasitic polarity in the conjugate ribbon PR. On the other hand, low values of  $N$  were found at the tip of NRH in the strong-field region. These results vindicated that dynamics of kernels moving along flare ribbons can be interpreted in terms of reconnection in quasi-separatrix layers (QSLs).

The content of the pages 41 - 54 is protected by copyright of IOP Publishing and is excluded from the online version of this thesis. The pages contain a published version of the manuscript

Lörinčík, J.; Aulanier, G.; Dudík, J.; Zemanová, A.; Dzifčáková, E.  
Velocities of Flare Kernels and the Mapping Norm of Field Line Connectivity  
*The Astrophysical Journal*, Vol. 881, 68 (2019)  
DOI: 10.3847/1538-4357/ab298f.

This manuscript is a separate attachment of the thesis.

## 5.2 Conversion of filament strands to flare loops as a manifestation of the ar–rf reconnection geometry

The filament eruption from 2012 August 31 has proven to be a valuable source of information about three-dimensional magnetic reconnection. The observations of this event were revisited in our analysis (Lörinčík et al., 2019b) of the 3D magnetic reconnection geometries introduced by Aulanier and Dudík (2019).

In the EUV filter channels of AIA, the filament revealed its fine structure composed of individual strands. In order to increase the contrast of the strands composing the filament legs, data from the 171 Å and 211 Å channels were processed with the multiscale Gaussian normalization (MGN) of Morgan and Druckmüller (2014). After doing so, we were capable of tracing the strands all the way to their footpoints (black and white circles in Figure 5.2). After the eruption had started, these footpoints became encircled by the hooked extension NRH of the negative-polarity ribbon NR. Initially, NRH had rapidly elongated, which was followed by its propagation toward west and contraction (Figure 2 in Lörinčík et al. (2019b)). NR later ‘surrounded’ a supergranule located in the vicinity, elongated toward north-west and exhibited a propagation in the same direction. During the hook’s propagation toward west and contraction, it started to cross the footpoints of the filament strands, at which the strands rooted therein disappeared (Figure 5.2, top row). Such process corresponds to the ‘sweeping’ of footpoints of field lines by hooked ribbons (Aulanier and Dudík, 2019). In the regions swept by NRH, footpoints of an arcade of flare loops started to appear, visible in the 94 Å channel of AIA (bottom row of Figure 5.2) as well as in observations carried-out in the Be-thin filter of XRT. The first flare loops started to be visible right after the sweeping commenced.

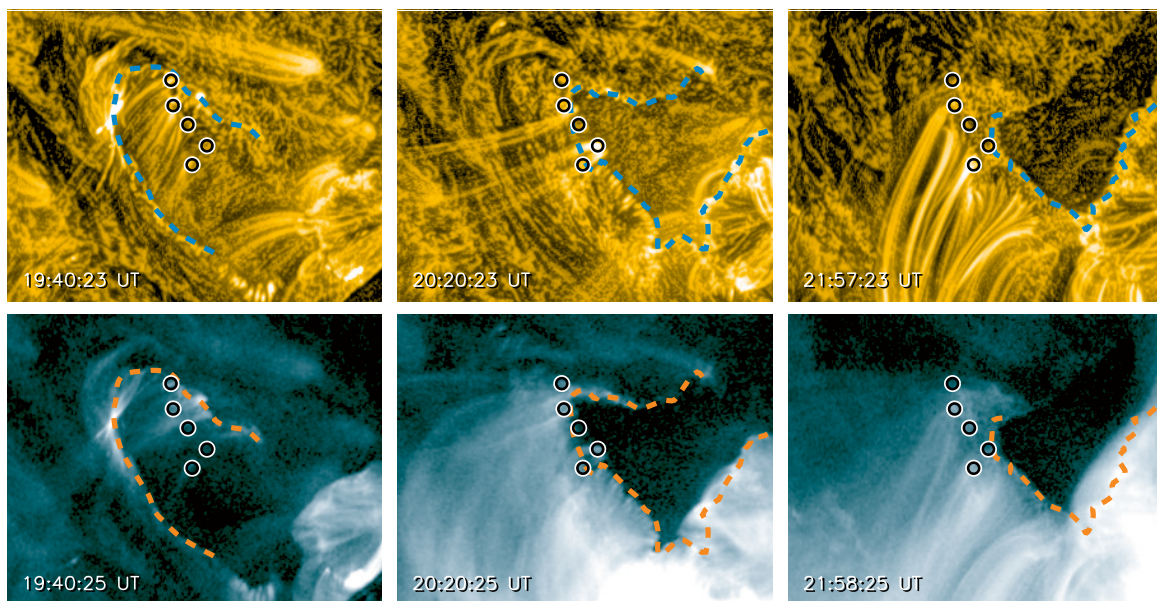


Figure 5.2: SDO/AIA observations of conversion of filament strands to flare loops. The top row presents MGN-processed 171 Å data view of disappearing filament strands, while the bottom row shows the formation of flare loops in the 94 Å channel data. The circles mark footpoints of the filament strands. The blue (top row) and orange (bottom row) dashed lines indicate the positions of the propagating ribbon.

As the time went by during the eruption, these flare loops cooled and started to be visible in filter channels sensitive to plasma at coronal temperatures. At that point, we were capable of distinguishing footpoints of individual flare loops, in particular in the 211 Å channel. Some of them corresponded to the footpoints in which the filament strands were rooted before the eruption. In order to associate these flare loops with the hot flare arcade visible right after sweeping of the filament’s footpoints, their cooling times were examined. We found that the timescale needed for cooling of flare loops from the temperature characteristic for the 94 Å channel down to the temperature of the 211 Å channel well-matched the temporal shift between the lightcurves produced by intensity averaging along a selected flare loop. By doing so, we evidenced that the flare loops rooted in regions swept by NRH originated when the filament strands reconnected.

Apart from this, we observed diminishing of a bundle of coronal loops rooted close to the tip of

NRH (Figure 5 in Lörinčák et al., 2019b). After the loops disappeared, their footpoints became a part of the dimming region encircled by NRH. These loops thus reconnected at the hook, but we were not able to relate them to the reconnection of the *individual* filament strands by the same hook.

Such reconnection is not addressed in the standard CSHKP model of solar flares. It contains neither field lines composing the footpoints of the erupting structure, nor ribbon hooks. Instead, this observed process can be interpreted via the ar–rf reconnection geometry. The conversion of the filament strands to the flare loops can be, in terms of its constituents, denoted as ‘r’  $\rightarrow$  ‘f’. Furthermore, we suggested that the diminishing of the coronal loops and inclusion of their footpoints to the dimming corresponds to ‘a’  $\rightarrow$  ‘r’. This is because dimming regions are strongly associated to footpoints of erupting structures (Section 2.1.3.3).

The content of the pages 57 - 67 is protected by copyright of IOP Publishing and is excluded from the online version of this thesis. The pages contain a published version of the manuscript

Lörinčík, J.; Dudík, J.; Aulanier, G.

Manifestations of Three-dimensional Magnetic Reconnection in an Eruption of a Quiescent Filament:  
Filament Strands Turning to Flare Loops

*The Astrophysical Journal*, Vol. 885, 83 (2019)

DOI: 10.3847/1538-4357/ab4519.

This manuscript is a separate attachment of the thesis.

### 5.3 Observations of all constituents of the three-dimensional magnetic reconnection geometries

In the first observational studies focused on the three-dimensional reconnection geometries (Zemanová et al., 2019; Lörinčík et al., 2019b), important evidence for key predictions imposed by the standard flare model in 3D was provided. However, in neither of the flares analysed in these studies, all of the pre- and post-reconnection constituents were observed. In the eruption analysed by Zemanová et al. (2019), the footpoints of the erupting hot channel drifted for several tens of arc-seconds, which is a signature of the ar–rf reconnection. Further, the observed ribbon hook exhibited the ‘back-and-forth’ motion, characteristic for sequential ar–rf reconnection. The field lines composing the hot channel were however visible only for a short period of time, which limited analysis of individual reconnection constituents. In Lörinčík et al. (2019b), we were capable of resolving the strands composing the filament but their drift along the ribbon hook was not observed. On the other hand, in analysis of another event we presented in Dudík, Lörinčík et al. (2019), we were capable of identifying all constituents of not only the ar–rf reconnection, but also the rr–rf reconnection.

In Dudík, Lörinčík et al. (2019), we were focused on the well-known eruption of an active region filament from 2011 June 7 accompanied by a M-class flare observed by SDO (Figure 5.3(a)). After the onset of the flare, two hooked ribbons formed. The negative-polarity ribbon NR, located to the east, developed a deformed hook NRH1 and NRH2, with the latter portion being located further from PIL. The positive-polarity ribbon PR formed a relatively-fainter hook PRH (panel (b)). Since a part of PRH as well as its overlying corona were obscured by the erupting filament, we focused on the hooks NRH1-2. During the flare, NRH2 exhibited the back-and-forth motion, with a small spatial region becoming a part of the flux rope and then leaving it again (Figure 3 in Dudík, Lörinčík et al. (2019)). This behaviour, previously reported by Aulanier and Dudík (2019) and Zemanová et al. (2019), is consistent with the sequential ar–rf reconnection.

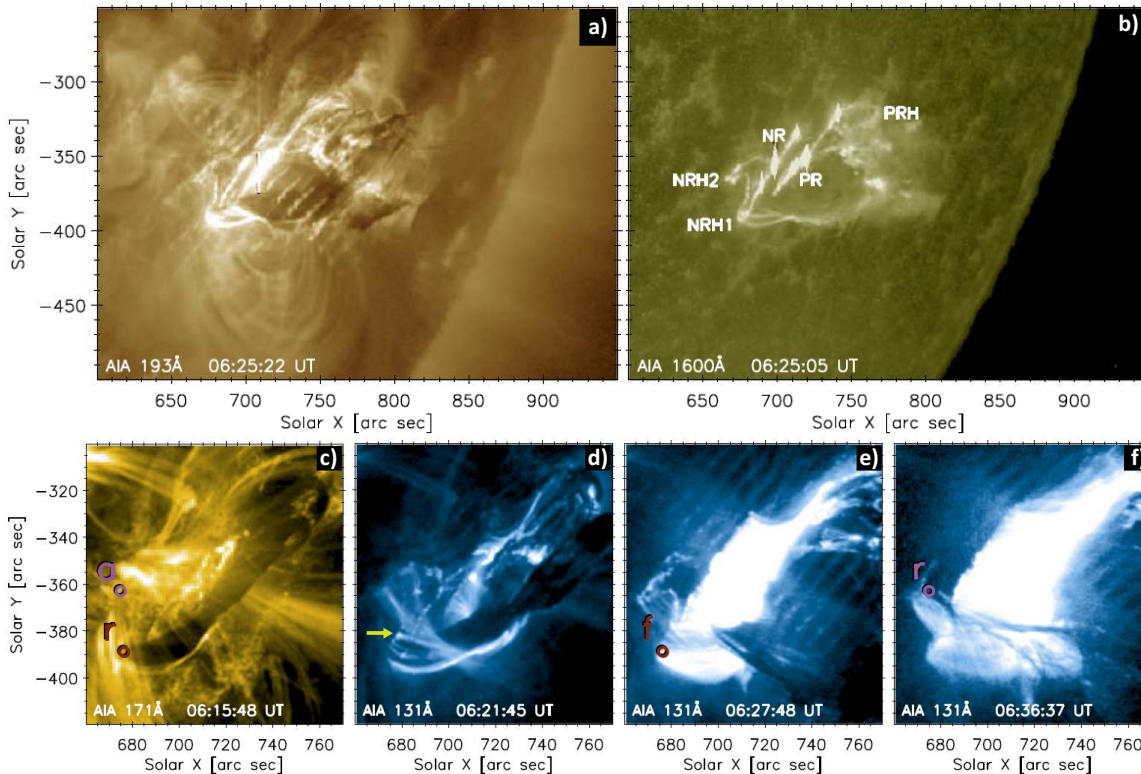


Figure 5.3: Observations of the three-dimensional ar–rf reconnection during the 2011 June 7 eruption. Panels (a) and (b) provide an overview of the eruption and flare ribbons in the 193 Å and 1600 Å filter channels of SDO/AIA, respectively. The individual constituents partaking in the reconnection, observed in the 171 Å and 131 Å channels, are shown in panels (c) – (f). The red circles plotted in panels (c) and (e) mark the location where the leg of the filament (‘r’) was rooted before the eruption, that later corresponded to the flare loop ‘f’. The violet circles in panels (c) and (f) highlight the footpoint of the coronal arcade ‘a’ which transformed to the new footpoint of the filament leg ‘r’. The yellow arrow in panel (d) marks one of the flare loops slipping near the leg of the filament.

The evolution of the filament strands and the coronal loops rooted near NRH2 indeed followed the process predicted for the ar–rf reconnection. Figure 5.3(c) shows the 171 Å channel view of the filament before the eruption. Initial footpoints of the leg of the filament are marked using the red circle ‘r’. Further, in the same panel, the footpoint of the coronal arcade ‘a’ is indicated using the violet circle. After the onset of the flare (panel (d)), the apparent slipping motion of flare loops (yellow arrow) as well as drifting of the leg of the filament from NRH1 to NRH2 started to be evident. As is clear from panel (e), a bright arcade of flare loops ‘f’ later developed. In the meantime, the leg of the filament continued its drift toward the tip of NRH2 (violet circle ‘r’ in Figure 5.3(f)). An examination of panels (c), (e), and (f) revealed the transformation of field lines in the analysed footpoints caused by the ar–rf reconnection. In the violet circle, previously-corresponding to the footpoint of the arcade, the leg of the filament was found (‘a’ → ‘r’). Before the eruption, the leg was located in the region marked using the red circle, in which the arcade of flare loops was later rooted (‘r’ → ‘f’).

Apart from providing the first complete evidence for the ar–rf reconnection and its constituents, we analysed the presence of the rr–rf reconnection geometry. During the peak phase of the flare, two bright strands ‘rr’ of the erupting filament were observed to converge toward one another. These strands subsequently reconnected in a region above the arcade of flare loops, at which a new flare loop appeared above the arcade and a bright blob of plasma ascended to the filament. The reconnection between the field lines composing erupting structures thus corresponds to the rr–rf reconnection. In Dudík, Lörinčík et al. (2019) we present the only observational evidence for such mechanism up to date.

The content of the pages 70 - 77 is protected by copyright of IOP Publishing and is excluded from the online version of this thesis. The pages contain a published version of the manuscript

Dudík, J.; Lörinčík, J.; Aulanier, G.; Zemanová, A.; Schmieder, B.  
Observation of All Pre- and Post-reconnection Structures Involved in Three-dimensional Reconnection Geometries in Solar Eruptions  
*The Astrophysical Journal*, Vol. 887, 71 (2019)  
DOI: 10.3847/1538-4357/ab4f86.

This manuscript is a separate attachment of the thesis.

## 5.4 Plasma outflows from a core dimming region and their relation to the ar–rf reconnection

In Lörinčík et al. (2021a), we describe observations of plasma outflows from a core dimming region formed after the 2015 April 28 eruption of a quiescent filament. Our analysis of imaging data from SDO/AIA indicates that the outflows were signatures of the solar wind. While searching for the most-probable interpretation of this phenomenon, signatures of three-dimensional magnetic reconnection were investigated. Even though traces of the ar–rf reconnection geometry were found in the dimming, this process was not related to the outflows.

During this long-duration eruption (Figure 5.4(a)), a pair of flare ribbons formed, one to the east and the other to the west. The western ribbon exhibited an extensive hook forming toward the south-west. In this hook, a core dimming region started to form after the onset of the eruption (Figure 5.4(b)). We found that the decrease of the intensity of plasma in the dimming region was caused by diminishing of funnel-shaped bundles of quiet Sun loops (hereafter ‘funnels’) located in this region. Along multiple funnels in the dimming, outward-oriented motions of plasma started to be visible in the 171 Å and 193 Å channel data. In time-distance diagrams constructed along the cut c1 plotted in panel (b), these motions imprinted a pattern composed of steep stripes. These were visible since  $\approx 15:00$  UT, corresponding to the fast-rise phase of the eruption, and lasted for more than five hours, until the analysed funnel disappeared (Figure 5.4(c)). The velocities of the motions measured by fitting the stripes ranged between 70 and  $140 \text{ km s}^{-1}$ , comparable with velocities resulting from spectroscopic measurements of the Doppler shifts in another dimming regions (e.g., Veronig et al., 2019).

We next focused on the interpretation of these motions. The timescale at which the motions were observed was found to be much larger than that of the dilution of plasma due to the eruption. Possible associations between the motions and MHD waves were ruled out, because the characteristics of the motions were changing neither with height, nor with time, which would be required due to

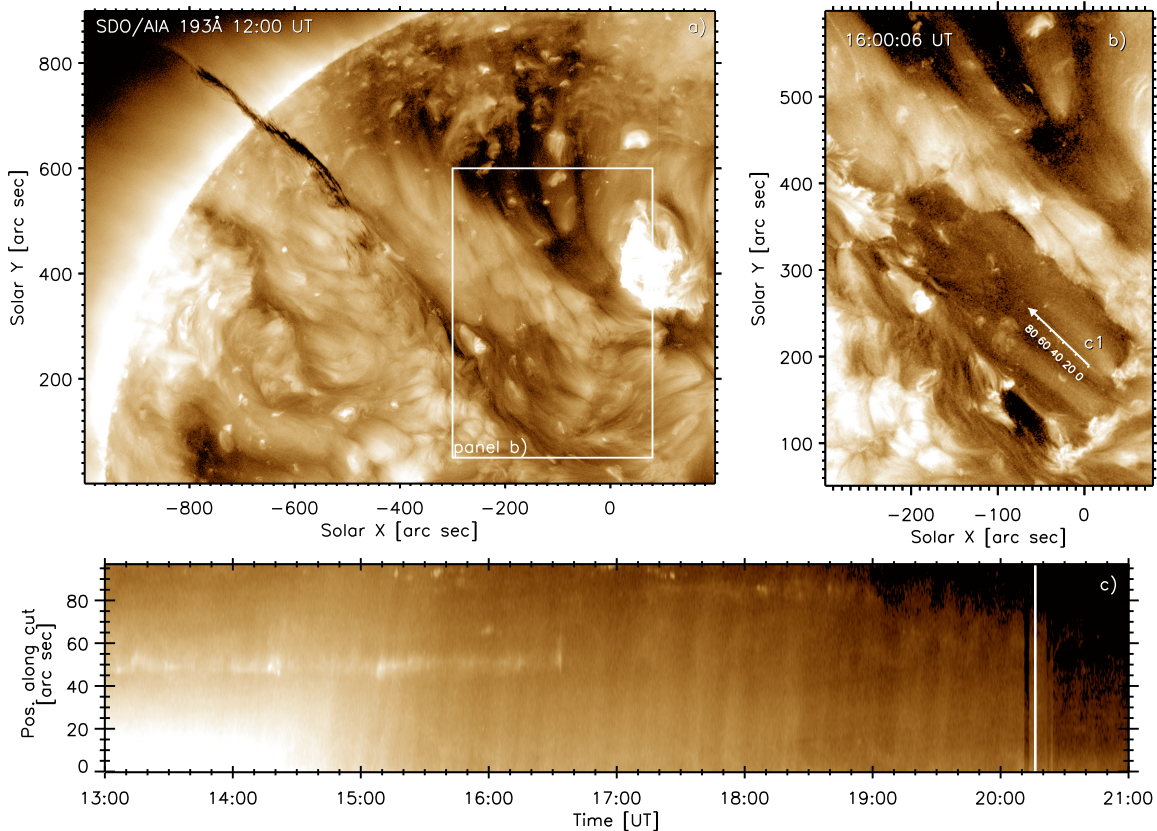


Figure 5.4: Analysis of plasma outflows from a core dimming region using the 193 Å channel SDO/AIA. In panel (a), the filament eruption from 2015 April 28 is presented. Panel (b) details a core dimming region in the south and a coronal hole to the north. The arrow c1 plotted along the funnel in the dimming region denotes the cut used for constructing the time-distance diagram plotted in panel (c).

the dependence of the Alfvén velocity on both the magnetic field strength and electron density. The motions were thus most-likely signatures of outflows of plasma and the funnel-shaped bundles of loops were true funnels, i.e., sources of the solar wind. Indeed, outflows of plasma with similar properties were found in funnel in an ordinary coronal hole located in the vicinity (Figure 6 in Lörinčík et al., 2021a). Since coronal holes are established sources of the fast solar wind, we suggested that the outflows from the dimming region might have also been contributing to the solar wind. Possibly, the eruption led to a reconfiguration of field lines of the funnels to a geometry allowing for the development of the outflows, just as along open field lines of coronal holes. The morphological resemblance between dimming regions and coronal holes is in our study highlighted by the fact that the two structures merged at  $\approx 06:00$  UT of the following day.

Further, we investigated signatures of the ar–rf reconnection at the hook encircling the analysed dimming region (Figure 8 in Lörinčík et al., 2021a). During the early phases of the eruption, faint strands composing the leg of the filament were drifting toward the tip of the hook. As the hook was elongating in the meantime, its outer edge swept footpoints of a canopy located in the vicinity, which subsequently disappeared. By the time the hook and the dimming region were fully formed, the area in which the canopy was rooted was entirely in the dimming region. Roughly 3 hours after the drifting started, very long, faint flare loops started to appear in the  $94 \text{ \AA}$  channel. They were anchored in the region which, before the eruption, corresponded to the leg of the filament. These phenomena are typical observational signatures of the ar–rf reconnection found in previous studies (Zemanová et al. (2019); Lörinčík et al. (2019b); Dudík, Lörinčík et al. (2019)). Unfortunately, we were not able to associate the canopy swept by the hook with the overlying coronal arcades (‘a’), for which we could not provide a complete evidence for all four constituents of this process. Our analysis shown that the funnels, along which the outflows were observed, did not enter the dimming region via the ar–rf reconnection. Therefore, reconnection occurring in this geometry did not play a role in the acceleration of the outflows along the funnels. On the other hand, this reconnection geometry was converting neighboring field lines, such as those of the canopy, to become parts of the erupting flux rope. The ar–rf reconnection thus played a direct role in the spatial expansion of the dimming region.

This study presents the first imaging evidence for outflows of plasma from dimming regions. Moreover, the characteristics of the outflows suggest that the funnels along which they were flowing to the interplanetary space might possibly be newly-discovered sources of the solar wind.

The content of the pages 80 - 94 is protected by copyright of IOP Publishing and is excluded from the online version of this thesis. The pages contain a published version of the manuscript

Lörinčík, J.; Dudík, J.; Aulanier, G.; Schmieder, B.; Golub, L.  
Imaging Evidence for Solar Wind Outflows Originating from a Coronal Mass Ejection Footpoint  
*The Astrophysical Journal*, Vol. 906, 62 (2021)  
DOI: 10.3847/1538-4357/abc8f6.

This manuscript is a separate attachment of the thesis.

## 5.5 Saddle-shaped arcades of flare loops

The last publication is again aimed at three-dimensional magnetic reconnection. In Lörinčík et al. (2021b), we have shown that arcades of flare loops formed during five events known from the literature exhibit a characteristic saddle-like morphology (Figure 5.5). Upon carrying out a detailed investigation of a selected event, we found that the formation of the saddles can be explained via the ar-rf reconnection.

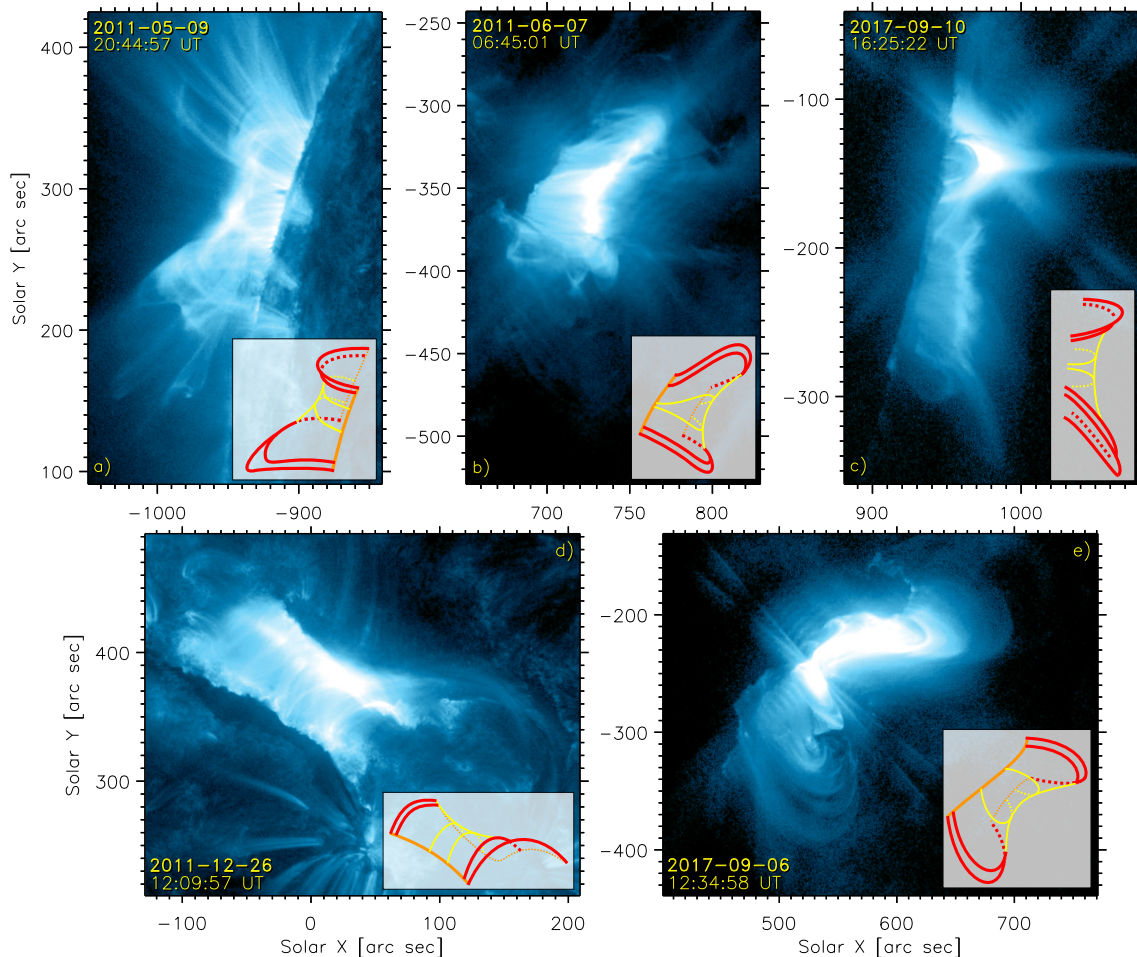


Figure 5.5: SDO/AIA 131 Å observations of the saddle-shaped arcades of flare loops. In the bottom-right of each panel, a cartoon highlighting the overall morphology of the arcade is included. The red lines highlight the longer and higher cantle loops at the edges of the arcades, while the yellow lines mark the central parts of the arcades, and the orange lines stand for the flare ribbons.

In our analysis, we primarily focused at SDO/AIA observations of five eruptive flares from 2011 May 9 (C5.4), 2011 June 7 (M2.5, see also Section 5.3), 2011 December 26 (C5.7), but also the well-known flares from 2017 September 6 (X2.2) and 10 (X8.2). The view of the arcades of flare loops formed during these events in the 131 Å channel of AIA is presented in Figure 5.5(a), (b), (d), (e), and (c), respectively. All of these arcades exhibited a saddle-like morphology. Cartoons depicting their simplified structure are shown in the bottom-right corner of each panel. Clearly, the flare loops in the central part of the arcades (yellow) were relatively-lower and shorter than those at their edges (red) which we termed ‘cantles’. In some cases, where the ribbons were identified and were not obscured, (e.g., in panels (d) and (e)), the cantle loops were seen to extend toward the ribbon hooks where they were anchored.

In order to investigate the origin of the cantle loops, a detailed analysis of the eruption of a hot channel from 2011 May 9 was performed. Apart from utilising the observations from AIA, datasets from the Extreme Ultraviolet Imager (EUVI; Wuelser et al., 2004) onboard STEREO-B were used. Owing to distinct orbits, each instrument observed the flare under different viewpoints. While AIA observed the event at the limb, EUVI did so near the center of the disk. The temperature coverage of the filter channels of AIA as well as its viewing angle allowed for a detailed study of the arcade of flare loops (Figure 5.5(a)).

In the 131 Å channel, the saddle was visible for roughly 15 minutes, until it became obscured by supra-arcade downflows. The southern cantle, which was higher than its northern counterpart, however remained visible even later on, after the arcade had cooled to coronal temperatures (Figure 2 of Lörinčík et al. (2021b)). The cooling arcade was also imaged by EUVI, which revealed that the southern cantle loop was longer than other flare loops along the arcade. Using observations from AIA and EUVI we thus shown that the morphology of saddles is given by presence of the cantle loops; flare loops at the edges of the arcades which are both higher and longer compared to the rest of the arcade.

Apart from that, EUVI data provided important insights into the formation of the cantles. In its 171 Å channel, a pair of hooked flare ribbons was imaged, one to the north and the other to the south. As is shown in Figure 3 in Lörinčík et al. (2021b), when the southern hook formed, it started to propagate and its tip converged to a bundle of inclined coronal loops overlying the hook. Consequently, the coronal loops begun to diminish and flare loops started to appear. Among the flare loops, the southern cantle loop, whose footpoint was located in a region swept by the hook, is found. This evolution of the ribbon hook and the overlying corona is comparable to that we reported in Lörinčík et al. (2019a). Even though the field lines composing the erupting hot channel were not observed by EUVI and a detailed analysis of the constituents was not possible, the evolution of the visible constituents is naturally explained by the ar–rf reconnection.

The discovery of the saddle-shaped flare arcades suggests that the mere morphology of arcades of flare loops can be indicative of the mechanism causing the formation of individual flare loops, in this case the ar–rf reconnection. Further, the fact that this property is common among arcades formed during different flares means that the saddles might be a newly-discovered, generic property of solar flares.

The content of the pages 97 - 104 is protected by copyright of IOP Publishing and is excluded from the online version of this thesis. The pages contain a published version of the manuscript

Löričník, J.; Dudík, J.; Aulanier, G.  
Saddle-shaped solar flare arcades  
*The Astrophysical Journal Letters*, Vol. 909, 4 (2021)  
DOI: 10.3847/2041-8213/abe7f7.

This manuscript is a separate attachment of the thesis.

# 6. Conclusions

## 6.1 Summary of results

We focused on manifestations of three-dimensional magnetic reconnection in observations of solar flares and eruptions. Most of the data analysed here were acquired by the Atmospheric Imaging Assembly and the Helioseismic and Magnetic Imager onboard the Solar Dynamics Observatory, but we also utilised data from the X-ray telescope of the Hinode mission, the Extreme Ultraviolet Imager onboard STEREO-B, and the Large Angle and Spectrometric Coronagraph of the Solar and Heliospheric Observatory satellite. To interpret the observed phenomena, the latest extensions of the standard flare model in 3D (Aulanier et al., 2012, 2013; Janvier et al., 2013; Aulanier and Dudík, 2019) were utilized. The results obtained are summarized in five peer-reviewed publications. In each of them, different aspects of 3D reconnection, important for driving and evolution of solar flares, are discussed (Section 5). In the following list, we summarize the main results important for the overall understanding of magnetic reconnection in 3D.

1. Velocities of the apparent slipping motion of flare kernels are inversely correlated with the photospheric magnetic field strength. Higher kernel velocities, reaching several hundred  $\text{km s}^{-1}$ , were found in the weak-field regions, such as in the elbow of the hook outside of the main bipole or in the vicinity of a parasitic polarity. The velocities depend on the mapping norm of field line connectivity modelled in the standard flare model in 3D (Lörinčík et al., 2019a).
2. Propagating *J*-shaped, or hooked, extensions of solar flare ribbons can sweep strands composing legs of filaments, at which the strands reconnect to form flare loops. As we show in Lörinčík et al. (2019b), such mechanism can be addressed by the 3D ar–rf reconnection geometry constituting the  $r \rightarrow f$  change of connectivity during reconnection between the erupting flux rope and its overlying arcades.
3. All constituents of the reconnection geometries found using the standard flare model in 3D (Aulanier and Dudík, 2019) can be resolved in a single event, though not always. In our analysis Dudík, Lörinčík et al. (2019) we suggested that the ar–rf reconnection occurred during early stages of the flare, while the rr–rf reconnection, between two field lines of the erupting flux rope, occurred later on when the flare peaked. This provides confirmation of the existence of these new, purely 3D reconnection geometries.
4. Solar eruptions can lead to development of long-lasting outflows of plasma from dimming regions (Lörinčík et al., 2021a). The outflows we analysed can be explained by the stretching of magnetic field lines during the analysed CME. It led to the development of funnel-shaped magnetic field geometry favorable for escape of plasma to the interplanetary space, just as in ordinary coronal holes. The ar–rf reconnection did not accelerate these outflows, but acted in the spatial expansion of the observed core dimming region.
5. Arcades of flare loops formed during selected eruptions exhibit a saddle-like morphology. It is related to the presence of long and high flare loops located at the edges of the arcades (Lörinčík et al., 2021b). We showed that the formation of such flare loops can be addressed by the ar–rf reconnection.

All of these results provide observational support for important predictions imposed by the standard flare model in 3D. Most importantly, our results indicate that the recently-predicted 3D reconnection geometries are most-likely generic. We have reported their signatures in seven eruptive flares of different magnitudes. By doing so we highlighted how essential 3D approach is for description of basic properties of solar flares.

## 6.2 Future prospects

The acquired results present possible openings for a follow-up research. Most of the works described here were centred on observational signatures of the three-dimensional magnetic reconnection geometries predicted by Aulanier and Dudík (2019). The search for such processes is contingent on identification of individual pre- and post-reconnection constituents. As indicated by our analyses, this has proven to be a difficult task. A novel approach was involved in Lörinčík et al. (2021b), where,

instead of investigating one event only, we found that a common property exhibited by multiple flares, the saddle-shaped arcades of flare loops, is possibly caused by the ar–rf reconnection. The saddles are the first phenomenon which needs to be studied in the future. The model counterparts of the long and high flare loops composing the saddles have not yet been investigated, meaning that the MHD simulation containing the standard flare model in 3D must be revisited. The properties of such field lines will consequently need to be compared with the observations. Confirming the role of the ar–rf reconnection in the formation of the saddles would mean that the morphology of arcades of flare loops can provide valuable information about processes powering flares and eruptions. Study of global characteristics of flares has proven to be an efficient probe for study of magnetic reconnection in 3D. Nevertheless, observational analyses still need to be performed in order to address how often can the constituents of different geometries be observed and reveal another possible associations between the reconnection geometries and other flare-related phenomena.

An interesting example of such process are the outflows of plasma from a core dimming region. As we suggest in Section 5.4, the outflows could be signatures of the solar wind developing in the footpoints of the filament, where the magnetic field is locally stretched. Observations of this new source of the solar wind remain to be confirmed by future studies. They will need to combine imaging or spectroscopic observations of dimming region outflows with in-situ measurements of physical properties of the outflowing plasma. A current mission well-suited for this task is the Solar Orbiter, whose data will soon be available. Its payload consists of both remote-sensing and in-situ instruments (Auchère et al., 2020) designed to operate in coordinated campaigns.

Another topic for possible future research aims at deposition and release of the energy by the slipping reconnection. Even though both the apparent slipping motion of flare loops and flare kernels are signatures of the same physical mechanism, the velocities of the two often vary even by an order of magnitude. An interesting observable is reported in Lörinčík et al. (2019a), where we argue that only the slowest kernels have counterparts observed as slipping flare loops in the corona. We suggested that this is likely caused by relatively-lower amounts of energy deposited per unit of area per time when the slippage is too fast. Verifying this hypothesis in the future might be subject to spectroscopic research of the slipping reconnection (Li and Zhang, 2015a; Dudík et al., 2016) or next-generation models of solar flares and eruptions. Without a doubt, recent 3D MHD models of solar eruptions, such as the standard flare model in 3D, are capable of well-reproducing the observed phenomena related to flares. Still, the model does not account for the thermodynamic evolution of plasma and cannot be used for modelling emission of plasma associated with field lines undergoing the slipping reconnection. Hopefully, future high-resolution 3D MHD models will be capable of fulfilling this task. Evolution of the plasma density and temperature has already been addressed e.g., in the 3D MHD model of recurrent eruptions in emerging flux regions of Syntelis et al. (2017, 2019). However, this model was not designed to be generic, as it contains two sequentially-erupting flux ropes and the field lines included in the model reconnect in two separated current sheets. Distribution of QSLs as well as the slipping reconnection in such configuration was not yet investigated.

Another category of models of radiation of solar flares relies on a synthesis of emission in individual ‘slabs’ of the solar atmosphere modelled using radiation-hydrodynamical codes such as RADYN (Carlsson and Stein, 1994) or Flarix (Kašparová et al., 2009; Varady et al., 2014). Recently, Kerr et al. (2020) shown that such models can be placed one next to each other in a 2D plane, taking into account the enhancement of the optically thin emission in pixels where overlying loops are present. Even though the model is able to qualitatively reproduce arcades of flare loops above an active region, the synthesized emission decays much more quickly than the observed one.

Such modelling lacks the third dimension, which, as we have shown, is important to understanding flares. For now, the question whether the most recent advances in the research of magnetic reconnection in 3D improve models of flare emission remains open. They should however be accounted for in the simulations to be produced in the near future, at least till high-resolution radiative 3D MHD models of flares powered by QSL reconnection will be developed.

# Bibliography

- Acton, L. W., Leibacher, J. W., Canfield, R. C., Gunkler, T. A., Hudson, H. S., and Kiplinger, A. L. Chromospheric evaporation in a well-observed compact flare. *The Astrophysical Journal*, 263: 409–422, December 1982. doi: 10.1086/160513.
- Al-Hachami, A. K. and Pontin, D. I. Magnetic reconnection at 3D null points: effect of magnetic field asymmetry. *Astronomy and Astrophysics*, 512:A84, March 2010. doi: 10.1051/0004-6361/200913002.
- Alissandrakis, C. E. On the computation of constant alpha force-free magnetic field. *Astronomy and Astrophysics*, 100(1):197–200, July 1981.
- Amari, T., Aly, J. J., Luciani, J. F., Boulmezaoud, T. Z., and Mikic, Z. Reconstructing the Solar Coronal Magnetic Field as a Force-Free Magnetic Field. *Solar Physics*, 174:129–149, August 1997. doi: 10.1023/A:1004966830232.
- Amari, T., Luciani, J. F., Mikic, Z., and Linker, J. A Twisted Flux Rope Model for Coronal Mass Ejections and Two-Ribbon Flares. *The Astrophysical Journal Letters*, 529(1):L49–L52, January 2000. doi: 10.1086/312444.
- Amari, T., Luciani, J. F., Aly, J. J., Mikic, Z., and Linker, J. Coronal Mass Ejection: Initiation, Magnetic Helicity, and Flux Ropes. II. Turbulent Diffusion-driven Evolution. *The Astrophysical Journal*, 595(2):1231–1250, October 2003. doi: 10.1086/377444.
- Amari, T., Canou, A., Aly, J.-J., Delyon, F., and Alauzet, F. Magnetic cage and rope as the key for solar eruptions. *Nature*, 554(7691):211–215, February 2018. doi: 10.1038/nature24671.
- Antiochos, S. K. The Magnetic Topology of Solar Eruptions. *The Astrophysical Journal Letters*, 502(2):L181–L184, August 1998. doi: 10.1086/311507.
- Antiochos, S. K., DeVore, C. R., and Klimchuk, J. A. A Model for Solar Coronal Mass Ejections. *The Astrophysical Journal*, 510(1):485–493, January 1999. doi: 10.1086/306563.
- Antonucci, E. Solar flare spectral diagnosis: Present and future. *Solar Physics*, 121(1-2):31–60, March 1989. doi: 10.1007/BF00161686.
- Archontis, V., Hood, A. W., Savcheva, A., Golub, L., and Deluca, E. On the Structure and Evolution of Complexity in Sigmoids: A Flux Emergence Model. *The Astrophysical Journal*, 691(2):1276–1291, February 2009. doi: 10.1088/0004-637X/691/2/1276.
- Asai, A., Masuda, S., Yokoyama, T., Shimojo, M., Isobe, H., Kurokawa, H., and Shibata, K. Difference between Spatial Distributions of the H $\alpha$  Kernels and Hard X-Ray Sources in a Solar Flare. *The Astrophysical Journal Letters*, 578(1):L91–L94, October 2002. doi: 10.1086/344566.
- Asai, A., Yokoyama, T., Shimojo, M., and Shibata, K. Downflow Motions Associated with Impulsive Nonthermal Emissions Observed in the 2002 July 23 Solar Flare. *The Astrophysical Journal Letters*, 605(1):L77–L80, April 2004. doi: 10.1086/420768.
- Aschwanden, M. J. *Physics of the Solar Corona. An Introduction with Problems and Solutions (2nd edition)*. 2005.
- Aschwanden, M. J., Tarbell, T. D., Nightingale, R. W., Schrijver, C. J., Title, A., Kankelborg, C. C., Martens, P., and Warren, H. P. Time Variability of the “Quiet” Sun Observed with TRACE. II. Physical Parameters, Temperature Evolution, and Energetics of Extreme-Ultraviolet Nanoflares. *The Astrophysical Journal*, 535(2):1047–1065, June 2000. doi: 10.1086/308867.
- Attrill, G. D. R., van Driel-Gesztelyi, L., Démoulin, P., Zhukov, A. N., Steed, K., Harra, L. K., Mandrini, C. H., and Linker, J. The Recovery of CME-Related Dimmings and the ICME’s Enduring Magnetic Connection to the Sun. *Solar Physics*, 252(2):349–372, November 2008. doi: 10.1007/s11207-008-9255-z.
- Attrill, G. D. R., Harra, L. K., van Driel-Gesztelyi, L., and Wills-Davey, M. J. Revealing the Fine Structure of Coronal Dimmings and Associated Flows with Hinode/EIS. Implications for Understanding the Source Regions of Sustained Outflow Following CMEs. *Solar Physics*, 264(1):119–147, June 2010. doi: 10.1007/s11207-010-9558-8.

- Auchère, F., Andretta, V., Antonucci, E., Bach, N., Battaglia, M., Bemporad, A., Berghmans, D., Buchlin, E., Caminade, S., Carlsson, M., Carlyle, J., Cerullo, J. J., Chamberlin, P. C., Colaninno, R. C., Davila, J. M., De Groof, A., Etesi, L., Fahmy, S., Fineschi, S., Fludra, A., Gilbert, H. R., Giunta, A., Grundy, T., Haberreiter, M., Harra, L. K., Hassler, D. M., Hirzberger, J., Howard, R. A., Hurford, G., Kleint, L., Kolleck, M., Krucker, S., Lagg, A., Landini, F., Long, D. M., Lefort, J., Lodirot, S., Mampaey, B., Maloney, S., Marliani, F., Martinez-Pillet, V., McMullin, D. R., Müller, D., Nicolini, G., Orozco Suarez, D., Pacros, A., Pancrazzi, M., Parenti, S., Peter, H., Philippon, A., Plunkett, S., Rich, N., Rochus, P., Rouillard, A., Romoli, M., Sanchez, L., Schühle, U., Sidher, S., Solanki, S. K., Spadaro, D., St Cyr, O. C., Straus, T., Tanco, I., Teriaca, L., Thompson, W. T., del Toro Iniesta, J. C., Verbeeck, C., Vourlidas, A., Watson, C., Wiegelmann, T., Williams, D., Woch, J., Zhukov, A. N., and Zouganelis, I. Coordination within the remote sensing payload on the Solar Orbiter mission. *Astronomy and Astrophysics*, 642:A6, October 2020. doi: 10.1051/0004-6361/201937032.
- Aulanier, G. and Schmieder, B. The magnetic nature of wide EUV filament channels and their role in the mass loading of CMEs. *Astronomy and Astrophysics*, 386:1106–1122, May 2002. doi: 10.1051/0004-6361:20020179.
- Aulanier, G., Parlat, E., and Démoulin, P. Current sheet formation in quasi-separatrix layers and hyperbolic flux tubes. *Astronomy and Astrophysics*, 444(3):961–976, December 2005. doi: 10.1051/0004-6361:20053600.
- Aulanier, G., Parlat, E., Démoulin, P., and DeVore, C. R. Slip-Running Reconnection in Quasi-Separatrix Layers. *Solar Physics*, 238(2):347–376, November 2006. doi: 10.1007/s11207-006-0230-2.
- Aulanier, G., Török, T., Démoulin, P., and DeLuca, E. E. Formation of Torus-Unstable Flux Ropes and Electric Currents in Erupting Sigmoids. *The Astrophysical Journal*, 708(1):314–333, January 2010. doi: 10.1088/0004-637X/708/1/314.
- Aulanier, G., Janvier, M., and Schmieder, B. The standard flare model in three dimensions. I. Strong-to-weak shear transition in post-flare loops. *Astronomy and Astrophysics*, 543:A110, July 2012. doi: 10.1051/0004-6361/201219311.
- Aulanier, G., Démoulin, P., Schrijver, C. J., Janvier, M., Parlat, E., and Schmieder, B. The standard flare model in three dimensions. II. Upper limit on solar flare energy. *Astronomy and Astrophysics*, 549:A66, January 2013. doi: 10.1051/0004-6361/201220406.
- Aulanier, G. and Dudík, J. Drifting of the line-tied footpoints of CME flux-ropes. *Astronomy and Astrophysics*, 621:A72, January 2019. doi: 10.1051/0004-6361/201834221.
- Aulanier, G., Golub, L., DeLuca, E. E., Cirtain, J. W., Kano, R., Lundquist, L. L., Narukage, N., Sakao, T., and Weber, M. A. Slipping Magnetic Reconnection in Coronal Loops. *Science*, 318(5856):1588, December 2007. doi: 10.1126/science.1146143.
- Babcock, H. W. The Topology of the Sun’s Magnetic Field and the 22-YEAR Cycle. *The Astrophysical Journal*, 133:572, March 1961. doi: 10.1086/147060.
- Babcock, H. W. The Solar Magnetograph. *The Astrophysical Journal*, 118:387, November 1953. doi: 10.1086/145767.
- Barczynski, K., Aulanier, G., Masson, S., and Wheatland, M. S. Flare Reconnection-driven Magnetic Field and Lorentz Force Variations at the Sun’s Surface. *The Astrophysical Journal*, 877(2):67, June 2019. doi: 10.3847/1538-4357/ab1b3d.
- Barczynski, K., Aulanier, G., Janvier, M., Schmieder, B., and Masson, S. Electric Current Evolution at the Footpoints of Solar Eruptions. *The Astrophysical Journal*, 895(1):18, May 2020. doi: 10.3847/1538-4357/ab893d.
- Bárta, M., Vršnak, B., and Karlický, M. Dynamics of plasmoids formed by the current sheet tearing. *Astronomy and Astrophysics*, 477(2):649–655, January 2008. doi: 10.1051/0004-6361:20078266.
- Bateman, G. *MHD instabilities*. 1978.
- Bellot Rubio, L. and Orozco Suárez, D. Quiet Sun magnetic fields: an observational view. *Living Reviews in Solar Physics*, 16(1):1, February 2019. doi: 10.1007/s41116-018-0017-1.

- Berger, T. E., Liu, W., and Low, B. C. SDO/AIA Detection of Solar Prominence Formation within a Coronal Cavity. *The Astrophysical Journal Letters*, 758(2):L37, October 2012. doi: 10.1088/2041-8205/758/2/L37.
- Berlicki, A., Schmieder, B., Vilmer, N., Aulanier, G., and Del Zanna, G. Evolution and magnetic topology of the M 1.0 flare of October 22, 2002. *Astronomy and Astrophysics*, 423:1119–1131, September 2004. doi: 10.1051/0004-6361:20040259.
- Boerner, P., Edwards, C., Lemen, J., Rausch, A., Schrijver, C., Shine, R., Shing, L., Stern, R., Tarbell, T., Title, A., Wolfson, C. J., Soufi, R., Spiller, E., Gullikson, E., McKenzie, D., Windt, D., Golub, L., Podgorski, W., Testa, P., and Weber, M. Initial Calibration of the Atmospheric Imaging Assembly (AIA) on the Solar Dynamics Observatory (SDO). *Solar Physics*, 275:41–66, January 2012. doi: 10.1007/s11207-011-9804-8.
- Bogachev, S. A., Somov, B. V., Kosugi, T., and Sakao, T. The Motions of the Hard X-Ray Sources in Solar Flares: Images and Statistics. *The Astrophysical Journal*, 630(1):561–572, September 2005. doi: 10.1086/431918.
- Bommier, V. and Leroy, J. L. Global Pattern of the Magnetic Field Vectors Above Neutral Lines from 1974 to 1982: Pic-du-Midi Observations of Prominences. In Webb, D. F., Schmieder, B., and Rust, D. M., editors, *IAU Colloq. 167: New Perspectives on Solar Prominences*, volume 150 of *Astronomical Society of the Pacific Conference Series*, page 434, January 1998.
- Brown, J. C. The Deduction of Energy Spectra of Non-Thermal Electrons in Flares from the Observed Dynamic Spectra of Hard X-Ray Bursts. *Solar Physics*, 18(3):489–502, July 1971. doi: 10.1007/BF00149070.
- Brueckner, G. E., Howard, R. A., Koomen, M. J., Korendyke, C. M., Michels, D. J., Moses, J. D., Socker, D. G., Dere, K. P., Lamy, P. L., Llebaria, A., Bout, M. V., Schwenn, R., Simnett, G. M., Bedford, D. K., and Eyles, C. J. The Large Angle Spectroscopic Coronagraph (LASCO). *Solar Physics*, 162(1-2):357–402, December 1995. doi: 10.1007/BF00733434.
- Bruzek, A. On the Association Between Loop Prominences and Flares. *The Astrophysical Journal*, 140:746, August 1964. doi: 10.1086/147969.
- Canfield, R. C., Metcalf, T. R., Strong, K. T., and Zarro, D. M. A novel observational test of momentum balance in a solar flare. *Nature*, 326(6109):165–166, March 1987. doi: 10.1038/326165a0.
- Canfield, R. C., Hudson, H. S., and McKenzie, D. E. Sigmoidal morphology and eruptive solar activity. *Geophysical Research Letters*, 26(6):627–630, January 1999. doi: 10.1029/1999GL900105.
- Cargill, P. J. and Priest, E. R. The heating of postflare loops. *The Astrophysical Journal*, 266:383–389, March 1983. doi: 10.1086/160786.
- Cargill, P. J., Mariska, J. T., and Antiochos, S. K. Cooling of Solar Flare Plasmas. I. Theoretical Considerations. *The Astrophysical Journal*, 439:1034, February 1995. doi: 10.1086/175240.
- Carlsson, M. and Stein, R. F. Radiation shock dynamics in the solar chromosphere - results of numerical simulations. In Carlsson, M., editor, *Chromospheric Dynamics*, page 47, 1994.
- Carmichael, H. A Process for Flares. *NASA Special Publication*, 50:451, 1964.
- Carrington, R. C. Description of a Singular Appearance seen in the Sun on September 1, 1859. *Monthly Notices of the Royal Astronomical Society*, 20:13–15, November 1859. doi: 10.1093/mnras/20.1.13.
- Chandra, R., Schmieder, B., Aulanier, G., and Malherbe, J. M. Evidence of Magnetic Helicity in Emerging Flux and Associated Flare. *Solar Physics*, 258(1):53–67, August 2009. doi: 10.1007/s11207-009-9392-z.
- Chen, H., Duan, Y., Yang, J., Yang, B., and Dai, J. Witnessing Tether-cutting Reconnection at the Onset of a Partial Eruption. *The Astrophysical Journal*, 869(1):78, December 2018. doi: 10.3847/1538-4357/aaead1.
- Chen, H., Yang, J., Ji, K., and Duan, Y. Observational Analysis on the Early Evolution of a CME Flux Rope: Preflare Reconnection and Flux Rope’s Footpoint Drift. *The Astrophysical Journal*, 887(2):118, December 2019. doi: 10.3847/1538-4357/ab527e.

- Chen, H., Zhang, J., Ma, S., Yang, S., Li, L., Huang, X., and Xiao, J. Confined Flares in Solar Active Region 12192 from 2014 October 18 to 29. *The Astrophysical Journal Letters*, 808(1):L24, July 2015. doi: 10.1088/2041-8205/808/1/L24.
- Chen, J., Santoro, R. A., Krall, J., Howard, R. A., Duffin, R., Moses, J. D., Brueckner, G. E., Darnell, J. A., and Burkepile, J. T. Magnetic Geometry and Dynamics of the Fast Coronal Mass Ejection of 1997 September 9. *The Astrophysical Journal*, 533(1):481–500, April 2000. doi: 10.1086/308646.
- Chen, J. Effects of Toroidal Forces in Current Loops Embedded in a Background Plasma. *The Astrophysical Journal*, 338:453, March 1989. doi: 10.1086/167211.
- Chen, J. Theory of prominence eruption and propagation: Interplanetary consequences. *Journal of Geophysical Research*, 101(A12):27499–27520, December 1996. doi: 10.1029/96JA02644.
- Chen, P. F. Coronal Mass Ejections: Models and Their Observational Basis. *Living Reviews in Solar Physics*, 8(1):1, April 2011. doi: 10.12942/lrsp-2011-1.
- Chen, P. F. and Shibata, K. An Emerging Flux Trigger Mechanism for Coronal Mass Ejections. *The Astrophysical Journal*, 545(1):524–531, December 2000. doi: 10.1086/317803.
- Cheng, J. X., Kerr, G., and Qiu, J. Hard X-Ray and Ultraviolet Observations of the 2005 January 15 Two-ribbon Flare. *The Astrophysical Journal*, 744(1):48, January 2012. doi: 10.1088/0004-637X/744/1/48.
- Cheng, X., Zhang, J., Ding, M. D., Liu, Y., and Poomvises, W. The Driver of Coronal Mass Ejections in the Low Corona: A Flux Rope. *The Astrophysical Journal*, 763(1):43, January 2013. doi: 10.1088/0004-637X/763/1/43.
- Cheng, X., Zhang, J., Kliem, B., Török, T., Xing, C., Zhou, Z. J., Inhester, B., and Ding, M. D. Initiation and Early Kinematic Evolution of Solar Eruptions. *The Astrophysical Journal*, 894(2):85, May 2020. doi: 10.3847/1538-4357/ab886a.
- Chifor, C., Mason, H. E., Tripathi, D., Isobe, H., and Asai, A. The early phases of a solar prominence eruption and associated flare: a multi-wavelength analysis. *Astronomy and Astrophysics*, 458(3):965–973, November 2006. doi: 10.1051/0004-6361:20065687.
- Chifor, C., Tripathi, D., Mason, H. E., and Dennis, B. R. X-ray precursors to flares and filament eruptions. *Astronomy and Astrophysics*, 472(3):967–979, September 2007. doi: 10.1051/0004-6361:20077771.
- Christensen-Dalsgaard, J., Dappen, W., Ajukov, S. V., Anderson, E. R., Antia, H. M., Basu, S., Baturin, V. A., Berthomieu, G., Chaboyer, B., Chitre, S. M., Cox, A. N., Demarque, P., Donatowicz, J., Dziembowski, W. A., Gabriel, M., Gough, D. O., Guenther, D. B., Guzik, J. A., Harvey, J. W., Hill, F., Houdek, G., Iglesias, C. A., Kosovichev, A. G., Leibacher, J. W., Morel, P., Proffitt, C. R., Provost, J., Reiter, J., Rhodes, J., E. J., Rogers, F. J., Roxburgh, I. W., Thompson, M. J., and Ulrich, R. K. The Current State of Solar Modeling. *Science*, 272(5266):1286–1292, May 1996. doi: 10.1126/science.272.5266.1286.
- Christensen-Dalsgaard, J. Helioseismology. *Reviews of Modern Physics*, 74(4):1073–1129, November 2002. doi: 10.1103/RevModPhys.74.1073.
- Cliwer, E. W., Dennis, B. R., Kiplinger, A. L., Kane, S. R., Neidig, D. F., Sheeley, J., N. R., and Koomen, M. J. Solar Gradual Hard X-Ray Bursts and Associated Phenomena. *The Astrophysical Journal*, 305:920, June 1986. doi: 10.1086/164306.
- Cohen, O., Attrill, G. D. R., Schwadron, N. A., Crooker, N. U., Owens, M. J., Downs, C., and Gombosi, T. I. Numerical simulation of the 12 May 1997 CME Event: The role of magnetic reconnection. *Journal of Geophysical Research (Space Physics)*, 115(A10):A10104, October 2010. doi: 10.1029/2010JA015464.
- Couvidat, S., Schou, J., Hoeksema, J. T., Bogart, R. S., Bush, R. I., Duvall, T. L., Liu, Y., Norton, A. A., and Scherrer, P. H. Observables Processing for the Helioseismic and Magnetic Imager Instrument on the Solar Dynamics Observatory. *Solar Physics*, 291:1887–1938, August 2016. doi: 10.1007/s11207-016-0957-3.
- Cranmer, S. R. Coronal Holes. *Living Reviews in Solar Physics*, 6(1):3, September 2009. doi: 10.12942/lrsp-2009-3.

- Crosby, N. B., Aschwanden, M. J., and Dennis, B. R. Frequency distributions and correlations of solar X-ray flare parameters. *Solar Physics*, 143(2):275–299, February 1993. doi: 10.1007/BF00646488.
- De Pontieu, B. High-Resolution Observations of Small-Scale Emerging Flux in the Photosphere. *The Astrophysical Journal*, 569(1):474–486, April 2002. doi: 10.1086/339231.
- De Pontieu, B., Title, A. M., Lemen, J. R., Kushner, G. D., Akin, D. J., Allard, B., Berger, T., Boerner, P., Cheung, M., Chou, C., Drake, J. F., Duncan, D. W., Freeland, S., Heyman, G. F., Hoffman, C., Hurlburt, N. E., Lindgren, R. W., Mathur, D., Rehse, R., Sabolish, D., Seguin, R., Schrijver, C. J., Tarbell, T. D., Wülser, J. P., Wolfson, C. J., Yanari, C., Mudge, J., Nguyen-Phuc, N., Timmons, R., van Bezooijen, R., Weingrod, I., Brookner, R., Butcher, G., Dougherty, B., Eder, J., Knagenhjelm, V., Larsen, S., Mansir, D., Phan, L., Boyle, P., Cheimets, P. N., DeLuca, E. E., Golub, L., Gates, R., Hertz, E., McKillip, S., Park, S., Perry, T., Podgorski, W. A., Reeves, K., Saar, S., Testa, P., Tian, H., Weber, M., Dunn, C., Eccles, S., Jaeggli, S. A., Kankelborg, C. C., Mashburn, K., Pust, N., Springer, L., Carvalho, R., Kleint, L., Marmie, J., Mazmanian, E., Pereira, T. M. D., Sawyer, S., Strong, J., Worden, S. P., Carlsson, M., Hansteen, V. H., Leenaarts, J., Wiesmann, M., Aloise, J., Chu, K. C., Bush, R. I., Scherrer, P. H., Brekke, P., Martinez-Sykora, J., Lites, B. W., McIntosh, S. W., Uitenbroek, H., Okamoto, T. J., Gummin, M. A., Auken, G., Jerram, P., Pool, P., and Waltham, N. The Interface Region Imaging Spectrograph (IRIS). *Solar Physics*, 289(7):2733–2779, July 2014. doi: 10.1007/s11207-014-0485-y.
- Del Zanna, G. The multi-thermal emission in solar active regions. *Astronomy and Astrophysics*, 558:A73, October 2013. doi: 10.1051/0004-6361/201321653.
- Del Zanna, G., Gibson, S. E., Mason, H. E., Pike, C. D., and Mandrini, C. H. Sigmoidal diagnostics with SOHO/CDS. *Advances in Space Research*, 30(3):551–556, January 2002. doi: 10.1016/S0273-1177(02)00341-1.
- del Zanna, G., Schmieder, B., Mason, H., Berlicki, A., and Bradshaw, S. The Gradual Phase of the X17 Flare on October 28, 2003. *Solar Physics*, 239(1-2):173–191, December 2006. doi: 10.1007/s11207-006-0184-4.
- Del Zanna, G., O’Dwyer, B., and Mason, H. E. SDO AIA and Hinode EIS observations of “warm” loops. *Astronomy and Astrophysics*, 535:A46, November 2011. doi: 10.1051/0004-6361/201117470.
- Del Zanna, G. and Mason, H. E. Solar UV and X-ray spectral diagnostics. *Living Reviews in Solar Physics*, 15(1):5, August 2018. doi: 10.1007/s41116-018-0015-3.
- Démoulin, P. A review of the quantitative links between CMEs and magnetic clouds. *Annales Geophysicae*, 26(10):3113–3125, October 2008. doi: 10.5194/angeo-26-3113-2008.
- Démoulin, P. and Aulanier, G. Criteria for Flux Rope Eruption: Non-equilibrium Versus Torus Instability. *The Astrophysical Journal*, 718(2):1388–1399, August 2010. doi: 10.1088/0004-637X/718/2/1388.
- Démoulin, P., Henoux, J. C., and Mandrini, C. H. Are magnetic null points important in solar flares ? *Astronomy and Astrophysics*, 285:1023–1037, May 1994.
- Démoulin, P., Henoux, J. C., Priest, E. R., and Mandrini, C. H. Quasi-Separatrix layers in solar flares. I. Method. *Astronomy and Astrophysics*, 308:643–655, April 1996a.
- Démoulin, P., Priest, E. R., and Lonie, D. P. Three-dimensional magnetic reconnection without null points 2. Application to twisted flux tubes. *Journal of Geophysical Research*, 101(A4):7631–7646, April 1996b. doi: 10.1029/95JA03558.
- Dere, K. P., Brueckner, G. E., Howard, R. A., Koomen, M. J., Korendyke, C. M., Kreplin, R. W., Michels, D. J., Moses, J. D., Moulton, N. E., Socker, D. G., St. Cyr, O. C., Delaboudinière, J. P., Artzner, G. E., Brunaud, J., Gabriel, A. H., Hochedez, J. F., Millier, F., Song, X. Y., Chauvineau, J. P., Marioge, J. P., Defise, J. M., Jamar, C., Rochus, P., Catura, R. C., Lemen, J. R., Gurman, J. B., Neupert, W., Clette, F., Cugnon, P., van Dessel, E. L., Lamy, P. L., Llebaria, A., Schwenn, R., and Simnett, G. M. EIT and LASCO Observations of the Initiation of a Coronal Mass Ejection. *Solar Physics*, 175(2):601–612, October 1997. doi: 10.1023/A:1004907307376.
- Doschek, G. A., Kreplin, R. W., and Feldman, U. High-resolution solar flare X-ray spectra. *The Astrophysical Journal Letters*, 233:L157–L160, November 1979. doi: 10.1086/183096.

- Doschek, G. A., Feldman, U., Kreplin, R. W., and Cohen, L. High-resolution X-ray spectra of solar flares. III - General spectral properties of X1-X5 type flares. *The Astrophysical Journal*, 239:725–737, July 1980. doi: 10.1086/158158.
- Dudík, J., Aulanier, G., Schmieder, B., Bommier, V., and Roudier, T. Topological Departures from Translational Invariance along a Filament Observed by THEMIS. *Solar Physics*, 248(1):29–50, March 2008. doi: 10.1007/s11207-008-9155-2.
- Dudík, J., Janvier, M., Aulanier, G., Del Zanna, G., Karlický, M., Mason, H. E., and Schmieder, B. Slipping Magnetic Reconnection during an X-class Solar Flare Observed by SDO/AIA. *The Astrophysical Journal*, 784:144, April 2014. doi: 10.1088/0004-637X/784/2/144.
- Dudík, J., Polito, V., Janvier, M., Mulay, S. M., Karlický, M., Aulanier, G., Del Zanna, G., Dzifčáková, E., Mason, H. E., and Schmieder, B. Slipping Magnetic Reconnection, Chromospheric Evaporation, Implosion, and Precursors in the 2014 September 10 X1.6-Class Solar Flare. *The Astrophysical Journal*, 823:41, May 2016. doi: 10.3847/0004-637X/823/1/41.
- Dudík, J., Zuccarello, F. P., Aulanier, G., Schmieder, B., and Démoulin, P. Expanding and Contracting Coronal Loops as Evidence of Vortex Flows Induced by Solar Eruptions. *The Astrophysical Journal*, 844(1):54, July 2017. doi: 10.3847/1538-4357/aa7aab.
- Dudík, J., Lörinčík, J., Aulanier, G., Zemanová, A., and Schmieder, B. Observation of All Pre- and Post-reconnection Structures Involved in Three-dimensional Reconnection Geometries in Solar Eruptions. *The Astrophysical Journal*, 887(1):71, December 2019. doi: 10.3847/1538-4357/ab4f86.
- Dungey, J. W. The motion of magnetic fields. *Monthly Notices of the Royal Astronomical Society*, 113:679, January 1953. doi: 10.1093/mnras/113.6.679.
- Dzifčáková, E., Dudík, J., Kotrč, P., Fárník, F., and Zemanová, A. KAPPA: A Package for Synthesis of Optically Thin Spectra for the Non-Maxwellian  $\kappa$ -distributions Based on the Chianti Database. *The Astrophysical Journal Supplement Series*, 217(1):14, March 2015. doi: 10.1088/0067-0049/217/1/14.
- Evans, R. M., Opher, M., and Gombosi, T. I. Learning from the Outer Heliosphere: Interplanetary Coronal Mass Ejection Sheath Flows and the Ejecta Orientation in the Lower Corona. *The Astrophysical Journal*, 728(1):41, February 2011. doi: 10.1088/0004-637X/728/1/41.
- Falchi, A., Qiu, J., and Cauzzi, G. Chromospheric evidence for magnetic reconnection. *Astronomy and Astrophysics*, 328:371–380, December 1997.
- Fan, Y. and Gibson, S. E. Onset of Coronal Mass Ejections Due to Loss of Confinement of Coronal Flux Ropes. *The Astrophysical Journal*, 668(2):1232–1245, October 2007. doi: 10.1086/521335.
- Fárník, F. and Savy, S. K. Soft X-Ray Pre-Flare Emission Studied in Yohkoh-SXT Images. *Solar Physics*, 183(2):339–357, December 1998. doi: 10.1023/A:1005092927592.
- Feldman, U., Doschek, G. A., and Kreplin, R. W. High-resolution X-ray spectra of the 1979 March 25 solar flare. *The Astrophysical Journal*, 238:365–374, May 1980a. doi: 10.1086/157993.
- Feldman, U., Doschek, G. A., Kreplin, R. W., and Mariska, J. T. High-resolution X-ray spectra of solar flares. IV - General spectral properties of M type flares. *The Astrophysical Journal*, 241:1175–1185, November 1980b. doi: 10.1086/158434.
- Fisk, L. A. and Schwadron, N. A. The Behavior of the Open Magnetic Field of the Sun. *The Astrophysical Journal*, 560(1):425–438, October 2001. doi: 10.1086/322503.
- Fletcher, L. and Hudson, H. The Magnetic Structure and Generation of EUV Flare Ribbons. *Solar Physics*, 204:69–89, December 2001. doi: 10.1023/A:1014275821318.
- Fletcher, L. and Hudson, H. S. Spectral and Spatial Variations of Flare Hard X-ray Footpoints. *Solar Physics*, 210(1):307–321, November 2002. doi: 10.1023/A:1022479610710.
- Fletcher, L., Dennis, B. R., Hudson, H. S., Krucker, S., Phillips, K., Veronig, A., Battaglia, M., Bone, L., Caspi, A., Chen, Q., Gallagher, P., Grigis, P. T., Ji, H., Liu, W., Milligan, R. O., and Temmer, M. An Observational Overview of Solar Flares. *Space Science Reviews*, 159(1-4):19–106, September 2011. doi: 10.1007/s11214-010-9701-8.
- Fletcher, L., Pollock, J. A., and Potts, H. E. Tracking of TRACE Ultraviolet Flare Footpoints. *Solar Physics*, 222(2):279–298, August 2004. doi: 10.1023/B:SOLA.0000043580.89730.4d.

- Forbes, T. G. Numerical simulation of a catastrophe model for coronal mass ejections. *Journal of Geophysical Research*, 95(A8):11919–11931, August 1990. doi: 10.1029/JA095iA08p11919.
- Forbes, T. G. A review on the genesis of coronal mass ejections. *Journal of Geophysical Research*, 105(A10):23153–23166, October 2000. doi: 10.1029/2000JA000005.
- Forbes, T. G. and Malherbe, J. M. A Shock Condensation Mechanism for Loop Prominences. *The Astrophysical Journal Letters*, 302:L67, March 1986. doi: 10.1086/184639.
- Foukal, P. V. *Solar Astrophysics, 2nd, Revised Edition*. 2004.
- Furth, H. P., Killeen, J., and Rosenbluth, M. N. Finite-Resistivity Instabilities of a Sheet Pinch. *Physics of Fluids*, 6(4):459–484, April 1963. doi: 10.1063/1.1706761.
- Gallagher, P. T., Dennis, B. R., Krucker, S., Schwartz, R. A., and Tolbert, A. K. Rhesi and Trace Observations of the 21 April 2002 x1.5 Flare. *Solar Physics*, 210(1):341–356, November 2002. doi: 10.1023/A:1022422019779.
- Glover, A., Harra, L. K., Matthews, S. A., Hori, K., and Culhane, J. L. Long term evolution of a non-active region sigmoid and its CME activity. *Astronomy and Astrophysics*, 378:239–246, October 2001. doi: 10.1051/0004-6361:20011170.
- Golub, L., Deluca, E., Austin, G., Bookbinder, J., Caldwell, D., Cheimets, P., Cirtain, J., Cosmo, M., Reid, P., Sette, A., Weber, M., Sakao, T., Kano, R., Shibasaki, K., Hara, H., Tsuneta, S., Kumagai, K., Tamura, T., Shimojo, M., McCracken, J., Carpenter, J., Haight, H., Siler, R., Wright, E., Tucker, J., Rutledge, H., Barbera, M., Peres, G., and Varisco, S. The X-Ray Telescope (XRT) for the Hinode Mission. *Solar Physics*, 243:63–86, June 2007. doi: 10.1007/s11207-007-0182-1.
- Gopalswamy, N., Yashiro, S., Krucker, S., Stenborg, G., and Howard, R. A. Intensity variation of large solar energetic particle events associated with coronal mass ejections. *Journal of Geophysical Research (Space Physics)*, 109(A12):A12105, December 2004. doi: 10.1029/2004JA010602.
- Gopalswamy, N., Yashiro, S., Michalek, G., Xie, H., Mäkelä, P., Vourlidas, A., and Howard, R. A. A Catalog of Halo Coronal Mass Ejections from SOHO. *Sun and Geosphere*, 5(1):7–16, November 2010.
- Graham, D. R., Cauzzi, G., Zangrilli, L., Kowalski, A., Simões, P., and Allred, J. Spectral Signatures of Chromospheric Condensation in a Major Solar Flare. *The Astrophysical Journal*, 895(1):6, May 2020. doi: 10.3847/1538-4357/ab88ad.
- Grechnev, V. V., Uralov, A. M., Kuzmenko, I. V., Kochanov, A. A., Chertok, I. M., and Kalashnikov, S. S. Responsibility of a Filament Eruption for the Initiation of a Flare, CME, and Blast Wave, and its Possible Transformation into a Bow Shock. *Solar Physics*, 290(1):129–158, January 2015. doi: 10.1007/s11207-014-0621-8.
- Hagenaar, H. J., Schrijver, C. J., and Title, A. M. The Distribution of Cell Sizes of the Solar Chromospheric Network. *The Astrophysical Journal*, 481(2):988–995, May 1997. doi: 10.1086/304066.
- Hagyard, M. J., Moore, R. L., and Emslie, A. G. The role of magnetic field shear in solar flares. *Advances in Space Research*, 4(7):71–80, January 1984. doi: 10.1016/0273-1177(84)90162-5.
- Handy, B. N., Acton, L. W., Kankelborg, C. C., Wolfson, C. J., Akin, D. J., Bruner, M. E., Carvalho, R., Catura, R. C., Chevalier, R., Duncan, D. W., Edwards, C. G., Feinstein, C. N., Freeland, S. L., Friedlaender, F. M., Hoffmann, C. H., Hurlburt, N. E., Jurcevich, B. K., Katz, N. L., Kelly, G. A., Lemen, J. R., Levay, M., Lindgren, R. W., Mathur, D. P., Meyer, S. B., Morrison, S. J., Morrison, M. D., Nightingale, R. W., Pope, T. P., Rehse, R. A., Schrijver, C. J., Shine, R. A., Shing, L., Strong, K. T., Tarbell, T. D., Title, A. M., Torgerson, D. D., Golub, L., Bookbinder, J. A., Caldwell, D., Cheimets, P. N., Davis, W. N., Deluca, E. E., McMullen, R. A., Warren, H. P., Amato, D., Fisher, R., Maldonado, H., and Parkinson, C. The transition region and coronal explorer. *Solar Physics*, 187(2):229–260, July 1999. doi: 10.1023/A:1005166902804.
- Hannah, I. G. and Kontar, E. P. The spectral difference between solar flare HXR coronal and footpoint sources due to wave-particle interactions. *Astronomy and Astrophysics*, 529:A109, May 2011. doi: 10.1051/0004-6361/201015710.

- Hannah, I. G. and Kontar, E. P. Multi-thermal dynamics and energetics of a coronal mass ejection in the low solar atmosphere. *Astronomy and Astrophysics*, 553:A10, May 2013. doi: 10.1051/0004-6361/201219727.
- Hara, H., Nishino, Y., Ichimoto, K., and Delaboudinière, J.-P. A Spectroscopic Observation of a Magnetic Reconnection Site in a Small Flaring Event. *The Astrophysical Journal*, 648(1):712–721, September 2006. doi: 10.1086/505638.
- Hara, H., Watanabe, T., Matsuzaki, K., Harra, L. K., Culhane, J. L., Cargill, P., Mariska, J. T., and Doschek, G. A. 2006 December 17 Long Duration Flare Observed with the Hinode EUV Imaging Spectrometer. *Publications of the Astronomical Society of Japan*, 60:275, April 2008. doi: 10.1093/pasj/60.2.275.
- Harra, L. K. and Sterling, A. C. Material Outflows from Coronal Intensity “Dimming Regions” during Coronal Mass Ejection Onset. *The Astrophysical Journal Letters*, 561(2):L215–L218, November 2001. doi: 10.1086/324767.
- Harra, L. K., Hara, H., Imada, S., Young, P. R., Williams, D. R., Sterling, A. C., Korendyke, C., and Attrill, G. D. R. Coronal Dimming Observed with Hinode: Outflows Related to a Coronal Mass Ejection. *Publications of the Astronomical Society of Japan*, 59:S801, November 2007. doi: 10.1093/pasj/59.sp3.S801.
- Harrison, R. A. The nature of solar flares associated with coronal mass ejection. *Astronomy and Astrophysics*, 304:585, December 1995.
- Heinzel, P., Schmieder, B., and Mein, P. Structure and Dynamics of Cool Flare Loops. *Solar Physics*, 139(1):81–104, May 1992. doi: 10.1007/BF00147883.
- Heinzel, P., Schmieder, B., and Tziotziou, K. Why Are Solar Filaments More Extended in Extreme-Ultraviolet Lines than in H $\alpha$ ? *The Astrophysical Journal Letters*, 561(2):L223–L227, November 2001. doi: 10.1086/324755.
- Heinzel, P., Schmieder, B., Fárník, F., Schwartz, P., Labrosse, N., Kotrč, P., Anzer, U., Molodij, G., Berlicki, A., DeLuca, E. E., Golub, L., Watanabe, T., and Berger, T. Hinode, TRACE, SOHO, and Ground-based Observations of a Quiescent Prominence. *The Astrophysical Journal*, 686(2):1383–1396, October 2008. doi: 10.1086/591018.
- Hernandez-Perez, A., Su, Y., Veronig, A. M., Thalmann, J., Gömöry, P., and Joshi, B. Pre-eruption Processes: Heating, Particle Acceleration, and the Formation of a Hot Channel before the 2012 October 20 M9.0 Limb Flare. *The Astrophysical Journal*, 874(2):122, April 2019. doi: 10.3847/1538-4357/ab09ed.
- Hesse, M. and Schindler, K. A theoretical foundation of general magnetic reconnection. *Journal of Geophysical Research*, 93(A6):5559–5567, June 1988. doi: 10.1029/JA093iA06p05559.
- Heyvaerts, J., Priest, E. R., and Rust, D. M. An emerging flux model for the solar phenomenon. *The Astrophysical Journal*, 216:123–137, August 1977. doi: 10.1086/155453.
- Hinterreiter, J., Veronig, A. M., Thalmann, J. K., Tschernitz, J., and Pötzi, W. Statistical Properties of Ribbon Evolution and Reconnection Electric Fields in Eruptive and Confined Flares. *Solar Physics*, 293(3):38, March 2018. doi: 10.1007/s11207-018-1253-1.
- Hirayama, T. Theoretical Model of Flares and Prominences. I: Evaporating Flare Model. *Solar Physics*, 34:323–338, February 1974. doi: 10.1007/BF00153671.
- Holman, G. D., Sui, L., Schwartz, R. A., and Emslie, A. G. Electron Bremsstrahlung Hard X-Ray Spectra, Electron Distributions, and Energetics in the 2002 July 23 Solar Flare. *The Astrophysical Journal Letters*, 595(2):L97–L101, October 2003. doi: 10.1086/378488.
- Hood, A. W. and Priest, E. R. Critical conditions for magnetic instabilities in force-free coronal loops. *Geophysical and Astrophysical Fluid Dynamics*, 17(1):297–318, January 1981. doi: 10.1080/03091928108243687.
- Hou, Y. J., Li, T., Song, Z. P., and Zhang, J. External reconnection and resultant reconfiguration of overlying magnetic fields during sympathetic eruptions of two filaments. *Astronomy and Astrophysics*, 640:A101, August 2020. doi: 10.1051/0004-6361/202038348.

- Howard, R. A., Moses, J. D., Vourlidas, A., Newmark, J. S., Socker, D. G., Plunkett, S. P., Korendyke, C. M., Cook, J. W., Hurley, A., Davila, J. M., Thompson, W. T., St Cyr, O. C., Mentzell, E., Mehalick, K., Lemen, J. R., Wuelser, J. P., Duncan, D. W., Tarbell, T. D., Wolfson, C. J., Moore, A., Harrison, R. A., Waltham, N. R., Lang, J., Davis, C. J., Eyles, C. J., Mapson-Menard, H., Simnett, G. M., Halain, J. P., Defise, J. M., Mazy, E., Rochus, P., Mercier, R., Ravet, M. F., Delmotte, F., Auchere, F., Delaboudiniere, J. P., Bothmer, V., Deutsch, W., Wang, D., Rich, N., Cooper, S., Stephens, V., Maahs, G., Baugh, R., McMullin, D., and Carter, T. Sun Earth Connection Coronal and Heliospheric Investigation (SECCHI). *Space Science Reviews*, 136(1-4): 67–115, April 2008. doi: 10.1007/s11214-008-9341-4.
- Howard, T. A., DeForest, C. E., Schneck, U. G., and Alden, C. R. Challenging Some Contemporary Views of Coronal Mass Ejections. II. The Case for Absent Filaments. *The Astrophysical Journal*, 834(1):86, January 2017. doi: 10.3847/1538-4357/834/1/86.
- Howard, T. A. and Harrison, R. A. On the Coronal Mass Ejection onset and Coronal Dimming. *Solar Physics*, 219(2):315–342, February 2004. doi: 10.1023/B:SOLA.0000022946.98359.63.
- Huang, S. Y., Retino, A., Phan, T. D., Daughton, W., Vaivads, A., Karimabadi, H., Zhou, M., Sahraoui, F., Li, G. L., Yuan, Z. G., Deng, X. H., Fu, H. S., Fu, S., Pang, Y., and Wang, D. D. In situ observations of flux rope at the separatrix region of magnetic reconnection. *Journal of Geophysical Research (Space Physics)*, 121(1):205–213, January 2016. doi: 10.1002/2015JA021468.
- Hudson, H. S. Thick-Target Processes and White-Light Flares. *Solar Physics*, 24(2):414–428, June 1972. doi: 10.1007/BF00153384.
- Hudson, H. S. Implosions in Coronal Transients. *The Astrophysical Journal Letters*, 531(1):L75–L77, March 2000. doi: 10.1086/312516.
- Hudson, H. S. and Cliver, E. W. Observing coronal mass ejections without coronagraphs. *Journal of Geophysical Research*, 106(A11):25199–25214, November 2001. doi: 10.1029/2000JA904026.
- Hudson, H. S., Strong, K. T., Dennis, B. R., Zarro, D., Inda, M., Kosugi, T., and Sakao, T. Impulsive Behavior in Solar Soft X-Radiation. *The Astrophysical Journal Letters*, 422:L25, February 1994. doi: 10.1086/187203.
- Hudson, H. S., Acton, L. W., and Freeland, S. L. A Long-Duration Solar Flare with Mass Ejection and Global Consequences. *The Astrophysical Journal*, 470:629, October 1996. doi: 10.1086/177894.
- Hudson, H. S., Wolfson, C. J., and Metcalf, T. R. White-Light Flares: A TRACE/RHESSI Overview. *Solar Physics*, 234(1):79–93, March 2006. doi: 10.1007/s11207-006-0056-y.
- Hudson, H. S. Global Properties of Solar Flares. *Space Science Reviews*, 158(1):5–41, January 2011. doi: 10.1007/s11214-010-9721-4.
- Hundhausen, A. J. Sizes and locations of coronal mass ejections: SMM observations from 1980 and 1984-1989. *Journal of Geophysical Research*, 98(A8):13177–13200, August 1993. doi: 10.1029/93JA00157.
- Ichimoto, K. and Kurokawa, H.  $H\alpha$  Red Asymmetry of Solar Flares. *Solar Physics*, 93(1):105–121, June 1984. doi: 10.1007/BF00156656.
- Illing, R. M. E. and Hundhausen, A. J. Observation of a coronal transient from 1.2 to 6 solar radii. *Journal of Geophysical Research*, 90(A1):275–282, January 1985. doi: 10.1029/JA090iA01p00275.
- Imada, S., Hara, H., Watanabe, T., Kamio, S., Asai, A., Matsuzaki, K., Harra, L. K., and Mariska, J. T. Discovery of a Temperature-Dependent Upflow in the Plage Region During a Gradual Phase of the X-Class Flare. *Publications of the Astronomical Society of Japan*, 59:S793, November 2007. doi: 10.1093/pasj/59.sp3.S793.
- Inglis, A. R. and Gilbert, H. R. Hard X-Ray and Ultraviolet Emission during the 2011 June 7 Solar Flare. *The Astrophysical Journal*, 777(1):30, November 2013. doi: 10.1088/0004-637X/777/1/30.
- Inoue, S., Hayashi, K., Magara, T., Choe, G. S., and Park, Y. D. Magnetohydrodynamic Simulation of the X2.2 Solar Flare on 2011 February 15. II. Dynamics Connecting the Solar Flare and the Coronal Mass Ejection. *The Astrophysical Journal*, 803(2):73, April 2015. doi: 10.1088/0004-637X/803/2/73.

- Inoue, S., Hayashi, K., and Kusano, K. Structure and Stability of Magnetic Fields in Solar Active Region 12192 Based on the Nonlinear Force-free Field Modeling. *The Astrophysical Journal*, 818(2):168, February 2016. doi: 10.3847/0004-637X/818/2/168.
- Isenberg, P. A. and Forbes, T. G. A Three-dimensional Line-tied Magnetic Field Model for Solar Eruptions. *The Astrophysical Journal*, 670(2):1453–1466, December 2007. doi: 10.1086/522025.
- Isobe, H., Shibata, K., and Machida, S. “Dawn-dusk asymmetry” in solar coronal arcade formations. *Geophysical Research Letters*, 29(21):2014, November 2002. doi: 10.1029/2001GL013816.
- James, A. W., Green, L. M., Palmerio, E., Valori, G., Reid, H. A. S., Baker, D., Brooks, D. H., van Driel-Gesztelyi, L., and Kilpua, E. K. J. On-Disc Observations of Flux Rope Formation Prior to Its Eruption. *Solar Physics*, 292(5):71, May 2017. doi: 10.1007/s11207-017-1093-4.
- Janvier, M., Aulanier, G., Pariat, E., and Démoulin, P. The standard flare model in three dimensions. III. Slip-running reconnection properties. *Astronomy and Astrophysics*, 555:A77, July 2013. doi: 10.1051/0004-6361/201321164.
- Janvier, M., Aulanier, G., Bommier, V., Schmieder, B., Démoulin, P., and Pariat, E. Electric Currents in Flare Ribbons: Observations and Three-dimensional Standard Model. *The Astrophysical Journal*, 788(1):60, June 2014. doi: 10.1088/0004-637X/788/1/60.
- Janvier, M., Aulanier, G., and Démoulin, P. From Coronal Observations to MHD Simulations, the Building Blocks for 3D Models of Solar Flares (Invited Review). *Solar Physics*, 290(12):3425–3456, December 2015. doi: 10.1007/s11207-015-0710-3.
- Janvier, M., Savcheva, A., Pariat, E., Tassev, S., Millholland, S., Bommier, V., McCauley, P., McKillop, S., and Dougan, F. Evolution of flare ribbons, electric currents, and quasi-separatrix layers during an X-class flare. *Astronomy and Astrophysics*, 591:A141, July 2016. doi: 10.1051/0004-6361/201628406.
- Janvier, M. Three-dimensional magnetic reconnection and its application to solar flares. *Journal of Plasma Physics*, 83(1):535830101, February 2017. doi: 10.1017/S0022377817000034.
- Jelínek, P., Karlický, M., Van Doorselaere, T., and Bárta, M. Oscillations Excited by Plasmoids Formed During Magnetic Reconnection in a Vertical Gravitationally Stratified Current Sheet. *The Astrophysical Journal*, 847(2):98, October 2017. doi: 10.3847/1538-4357/aa88a6.
- Jing, J., Chae, J., and Wang, H. Spatial Distribution of Magnetic Reconnection in the 2006 December 13 Solar Flare as Observed by Hinode. *The Astrophysical Journal Letters*, 672(1):L73, January 2008. doi: 10.1086/526339.
- Jing, J., Liu, C., Lee, J., Ji, H., Liu, N., Xu, Y., and Wang, H. Statistical Analysis of Torus and Kink Instabilities in Solar Eruptions. *The Astrophysical Journal*, 864(2):138, September 2018. doi: 10.3847/1538-4357/aad6e4.
- Joshi, N. C., Zhu, X., Schmieder, B., Aulanier, G., Janvier, M., Joshi, B., Magara, T., Chandra, R., and Inoue, S. Generalization of the Magnetic Field Configuration of Typical and Atypical Confined Flares. *The Astrophysical Journal*, 871(2):165, February 2019. doi: 10.3847/1538-4357/aaf3b5.
- Jurčák, J. Azimuthal variations of magnetic field strength and inclination on penumbral boundaries. *Astronomy and Astrophysics*, 531:A118, July 2011. doi: 10.1051/0004-6361/201015959.
- Kahler, S. W. and Hudson, H. S. Origin and development of transient coronal holes. *Journal of Geophysical Research*, 106(A12):29239–29248, December 2001. doi: 10.1029/2001JA000127.
- Kane, S. R. and Donnelly, R. F. Impulsive Hard X-Ray and Ultraviolet Emission during Solar Flares. *The Astrophysical Journal*, 164:151, February 1971. doi: 10.1086/150826.
- Karlický, M. and Bárta, M. Drifting pulsating structures generated during tearing and coalescence processes in a flare current sheet. *Astronomy and Astrophysics*, 464(2):735–740, March 2007. doi: 10.1051/0004-6361:20065983.
- Kašparová, J., Varady, M., Heinzel, P., Karlický, M., and Moravec, Z. Response of optical hydrogen lines to beam heating. I. Electron beams. *Astronomy and Astrophysics*, 499(3):923–934, June 2009. doi: 10.1051/0004-6361/200811559.

- Kerr, G. S., Allred, J. C., and Polito, V. Solar Flare Arcade Modeling: Bridging the Gap from 1D to 3D Simulations of Optically Thin Radiation. *The Astrophysical Journal*, 900(1):18, September 2020. doi: 10.3847/1538-4357/abaa46.
- Kim, S., Moon, Y. J., Kim, Y. H., Park, Y. D., Kim, K. S., Choe, G. S., and Kim, K. H. Preflare Eruption Triggered by a Tether-cutting Process. *The Astrophysical Journal*, 683(1):510–515, August 2008. doi: 10.1086/588717.
- Kliem, B. and Török, T. Torus Instability. *Physical Review Letters*, 96(25):255002, June 2006. doi: 10.1103/PhysRevLett.96.255002.
- Kliem, B., Lee, J., Liu, R., White, S. M., Liu, C., and Masuda, S. Nonequilibrium Flux Rope Formation by Confined Flares Preceding a Solar Coronal Mass Ejection. *The Astrophysical Journal*, 909(1):91, March 2021. doi: 10.3847/1538-4357/abda37.
- Klimchuk, J. A. On Solving the Coronal Heating Problem. *Solar Physics*, 234(1):41–77, March 2006. doi: 10.1007/s11207-006-0055-z.
- Klimchuk, J. A. Key aspects of coronal heating. *Philosophical Transactions of the Royal Society of London Series A*, 373(2042):20140256–20140256, April 2015. doi: 10.1098/rsta.2014.0256.
- Kopp, R. A. and Pneuman, G. W. Magnetic reconnection in the corona and the loop prominence phenomenon. *Solar Physics*, 50:85–98, October 1976. doi: 10.1007/BF00206193.
- Krucker, S., Battaglia, M., Cargill, P. J., Fletcher, L., Hudson, H. S., MacKinnon, A. L., Masuda, S., Sui, L., Tomczak, M., Veronig, A. L., Vlahos, L., and White, S. M. Hard X-ray emission from the solar corona. *The Astronomy and Astrophysics Review*, 16:155–208, October 2008. doi: 10.1007/s00159-008-0014-9.
- Krucker, S. and Battaglia, M. Particle Densities within the Acceleration Region of a Solar Flare. *The Astrophysical Journal*, 780(1):107, January 2014. doi: 10.1088/0004-637X/780/1/107.
- Krucker, S., Hudson, H. S., Glesener, L., White, S. M., Masuda, S., Wuelser, J. P., and Lin, R. P. Measurements of the Coronal Acceleration Region of a Solar Flare. *The Astrophysical Journal*, 714(2):1108–1119, May 2010. doi: 10.1088/0004-637X/714/2/1108.
- Kusano, K., Maeshiro, T., Yokoyama, T., and Sakurai, T. The Trigger Mechanism of Solar Flares in a Coronal Arcade with Reversed Magnetic Shear. *The Astrophysical Journal*, 610(1):537–549, July 2004. doi: 10.1086/421547.
- Labrosse, N., Heinzel, P., Vial, J. C., Kucera, T., Parenti, S., Gunár, S., Schmieder, B., and Kilper, G. Physics of Solar Prominences: I—Spectral Diagnostics and Non-LTE Modelling. *Space Science Reviews*, 151(4):243–332, April 2010. doi: 10.1007/s11214-010-9630-6.
- Landi, E., Del Zanna, G., Young, P. R., Dere, K. P., and Mason, H. E. CHIANTI—An Atomic Database for Emission Lines. XII. Version 7 of the Database. *The Astrophysical Journal*, 744(2):99, Jan 2012. doi: 10.1088/0004-637X/744/2/99.
- Lang, K. R. *The Sun From Space*. 2009. doi: 10.1007/978-3-540-76953-8.
- Lau, Y.-T. Magnetic Nulls and Topology in a Class of Solar Flare Models. *Solar Physics*, 148(2): 301–324, December 1993. doi: 10.1007/BF00645092.
- Lau, Y.-T. and Finn, J. M. Three-dimensional Kinematic Reconnection in the Presence of Field Nulls and Closed Field Lines. *The Astrophysical Journal*, 350:672, February 1990. doi: 10.1086/168419.
- Lemen, J. R., Title, A. M., Akin, D. J., Boerner, P. F., Chou, C., Drake, J. F., Duncan, D. W., Edwards, C. G., Friedlaender, F. M., Heyman, G. F., Hurlburt, N. E., Katz, N. L., Kushner, G. D., Levay, M., Lindgren, R. W., Mathur, D. P., McFeaters, E. L., Mitchell, S., Rehse, R. A., Schrijver, C. J., Springer, L. A., Stern, R. A., Tarbell, T. D., Wuelser, J.-P., Wolfson, C. J., Yanari, C., Bookbinder, J. A., Cheimets, P. N., Caldwell, D., Deluca, E. E., Gates, R., Golub, L., Park, S., Podgorski, W. A., Bush, R. I., Scherrer, P. H., Gummin, M. A., Smith, P., Auken, G., Jerram, P., Pool, P., Souffi, R., Windt, D. L., Beardsley, S., Clapp, M., Lang, J., and Waltham, N. The Atmospheric Imaging Assembly (AIA) on the Solar Dynamics Observatory (SDO). *Solar Physics*, 275:17–40, January 2012. doi: 10.1007/s11207-011-9776-8.

- Li, H., Schmieder, B., Aulanier, G., and Berlicki, A. Is Pre-Eruptive Null Point Reconnection Required for Triggering Eruptions? *Solar Physics*, 237(1):85–100, August 2006. doi: 10.1007/s11207-006-0173-7.
- Li, J., Mickey, D. L., and LaBonte, B. J. The X3 Flare of 2002 July 15. *The Astrophysical Journal*, 620(2):1092–1100, February 2005. doi: 10.1086/427205.
- Li, L. and Zhang, J. On the Brightening Propagation of Post-Flare Loops Observed by TRACE. *The Astrophysical Journal*, 690(1):347–357, January 2009. doi: 10.1088/0004-637X/690/1/347.
- Li, L., Zhang, J., Peter, H., Priest, E., Chen, H., Guo, L., Chen, F., and Mackay, D. Magnetic reconnection between a solar filament and nearby coronal loops. *Nature Physics*, 12(9):847–851, September 2016. doi: 10.1038/nphys3768.
- Li, T. and Zhang, J. Quasi-periodic Slipping Magnetic Reconnection During an X-class Solar Flare Observed by the Solar Dynamics Observatory and Interface Region Imaging Spectrograph. *The Astrophysical Journal Letters*, 804:L8, May 2015a. doi: 10.1088/2041-8205/804/1/L8.
- Li, T., Yang, S., Zhang, Q., Hou, Y., and Zhang, J. Two Episodes of Magnetic Reconnections during a Confined Circular-ribbon Flare. *The Astrophysical Journal*, 859:122, June 2018. doi: 10.3847/1538-4357/aabe84.
- Li, T. and Zhang, J. High-Resolution Observations of a Flux Rope with the Interface Region Imaging Spectrograph. *Solar Physics*, 290(10):2857–2870, October 2015b. doi: 10.1007/s11207-015-0768-y.
- Li, T., Zhang, J., and Hou, Y. Flare Ribbons Approach Observed by the Interface Region Imaging Spectrograph and the Solar Dynamics Observatory. *The Astrophysical Journal*, 848(1):32, October 2017. doi: 10.3847/1538-4357/aa8c01.
- Li, X., Morgan, H., Leonard, D., and Jeska, L. A Solar Tornado Observed by AIA/SDO: Rotational Flow and Evolution of Magnetic Helicity in a Prominence and Cavity. *The Astrophysical Journal Letters*, 752(2):L22, June 2012. doi: 10.1088/2041-8205/752/2/L22.
- Lim, E.-K., Yurchyshyn, V., Kumar, P., Cho, K., Jiang, C., Kim, S., Yang, H., Chae, J., Cho, K.-S., and Lee, J. Observation of a Large-scale Quasi-circular Secondary Ribbon Associated with Successive Flares and a Halo CME. *The Astrophysical Journal*, 850(2):167, December 2017. doi: 10.3847/1538-4357/aa93f7.
- Lin, J., Forbes, T. G., Isenberg, P. A., and Démoulin, P. The Effect of Curvature on Flux-Rope Models of Coronal Mass Ejections. *The Astrophysical Journal*, 504(2):1006–1019, September 1998. doi: 10.1086/306108.
- Lin, J., Soon, W., and Baliunas, S. L. Theories of solar eruptions: a review. *New Astronomy Reviews*, 47(2):53–84, April 2003. doi: 10.1016/S1387-6473(02)00271-3.
- Lin, R. P., Dennis, B. R., Hurford, G. J., Smith, D. M., Zehnder, A., Harvey, P. R., Curtis, D. W., Pankow, D., Turin, P., Bester, M., Csillaghy, A., Lewis, M., Madden, N., van Beek, H. F., Appleby, M., Raudorf, T., McTiernan, J., Ramaty, R., Schmahl, E., Schwartz, R., Krucker, S., Abiad, R., Quinn, T., Berg, P., Hashii, M., Sterling, R., Jackson, R., Pratt, R., Campbell, R. D., Malone, D., Landis, D., Barrington-Leigh, C. P., Slassi-Sennou, S., Cork, C., Clark, D., Amato, D., Orwig, L., Boyle, R., Banks, I. S., Shirey, K., Tolbert, A. K., Zarro, D., Snow, F., Thomsen, K., Henneck, R., McHedlishvili, A., Ming, P., Fivian, M., Jordan, J., Wanner, R., Crubb, J., Preble, J., Matranga, M., Benz, A., Hudson, H., Canfield, R. C., Holman, G. D., Crannell, C., Kosugi, T., Emslie, A. G., Vilmer, N., Brown, J. C., Johns-Krull, C., Aschwanden, M., Metcalf, T., and Conway, A. The Reuven Ramaty High-Energy Solar Spectroscopic Imager (RHESSI). *Solar Physics*, 210(1):3–32, November 2002. doi: 10.1023/A:1022428818870.
- Lin, Y., Martin, S. F., and Engvold, O. Filament Substructures and their Interrelation. In Howe, R., Komm, R. W., Balasubramaniam, K. S., and Petrie, G. J. D., editors, *Subsurface and Atmospheric Influences on Solar Activity*, volume 383 of *Astronomical Society of the Pacific Conference Series*, page 235, January 2008.
- Linker, J. A., Mikić, Z., Lionello, R., Riley, P., Amari, T., and Odstreil, D. Flux cancellation and coronal mass ejections. *Physics of Plasmas*, 10(5):1971–1978, May 2003. doi: 10.1063/1.1563668.

- Litvinenko, Y. E. and Martin, S. F. Magnetic reconnection as the cause of a photospheric canceling feature and mass flows in a filament. *Solar Physics*, 190:45–58, December 1999. doi: 10.1023/A:1005284116353.
- Liu, C., Prasad, A., Lee, J., and Wang, H. An Eruptive Circular-ribbon Flare with Extended Remote Brightenings. *The Astrophysical Journal*, 899(1):34, August 2020. doi: 10.3847/1538-4357/ab9cbe.
- Longcope, D. W. and Cowley, S. C. Current sheet formation along three-dimensional magnetic separators. *Physics of Plasmas*, 3(8):2885–2897, August 1996. doi: 10.1063/1.871627.
- Longcope, D. W. and Forbes, T. G. Breakout and Tether-Cutting Eruption Models Are Both Catastrophic (Sometimes). *Solar Physics*, 289(6):2091–2122, June 2014. doi: 10.1007/s11207-013-0464-8.
- Longcope, D. W. Topological Methods for the Analysis of Solar Magnetic Fields. *Living Reviews in Solar Physics*, 2(1):7, December 2005. doi: 10.12942/lrsp-2005-7.
- López Ariste, A., Aulanier, G., Schmieder, B., and Sainz Dalda, A. First observation of bald patches in a filament channel and at a barb endpoint. *Astronomy and Astrophysics*, 456(2):725–735, September 2006. doi: 10.1051/0004-6361:20064923.
- Lörinčík, J., Aulanier, G., Dudík, J., Zemanová, A., and Dzifčáková, E. Velocities of Flare Kernels and the Mapping Norm of Field Line Connectivity. *The Astrophysical Journal*, 881(1):68, August 2019a. doi: 10.3847/1538-4357/ab298f.
- Lörinčík, J., Dudík, J., and Aulanier, G. Manifestations of Three-dimensional Magnetic Reconnection in an Eruption of a Quiescent Filament: Filament Strands Turning to Flare Loops. *The Astrophysical Journal*, 885(1):83, November 2019b. doi: 10.3847/1538-4357/ab4519.
- Lörinčík, J., Dudík, J., Aulanier, G., Schmieder, B., and Golub, L. Imaging Evidence for Solar Wind Outflows Originating from a Coronal Mass Ejection Footpoint. *The Astrophysical Journal*, 906(1):62, January 2021a. doi: 10.3847/1538-4357/abc8f6.
- Lörinčík, J., Dudík, J., and Aulanier, G. Saddle-shaped Solar Flare Arcades. *The Astrophysical Journal Letters*, 909(1):L4, March 2021b. doi: 10.3847/2041-8213/abe7f7.
- Low, B. C. and Wolfson, R. Spontaneous Formation of Electric Current Sheets and the Origin of Solar Flares. *The Astrophysical Journal*, 324:574, January 1988. doi: 10.1086/165918.
- Lugaz, N. and Roussev, I. I. Numerical modeling of interplanetary coronal mass ejections and comparison with heliospheric images. *Journal of Atmospheric and Solar-Terrestrial Physics*, 73(10):1187–1200, June 2011. doi: 10.1016/j.jastp.2010.08.016.
- Lugaz, N., Downs, C., Shibata, K., Roussev, I. I., Asai, A., and Gombosi, T. I. Numerical Investigation of a Coronal Mass Ejection from an Anemone Active Region: Reconnection and Deflection of the 2005 August 22 Eruption. *The Astrophysical Journal*, 738(2):127, September 2011. doi: 10.1088/0004-637X/738/2/127.
- Mackay, D. H., Karpen, J. T., Ballester, J. L., Schmieder, B., and Aulanier, G. Physics of Solar Prominences: II—Magnetic Structure and Dynamics. *Space Science Reviews*, 151(4):333–399, April 2010. doi: 10.1007/s11214-010-9628-0.
- Mackay, D. H., Gaizauskas, V., and Yeates, A. R. Where Do Solar Filaments Form?: Consequences for Theoretical Models. *Solar Physics*, 248(1):51–65, March 2008. doi: 10.1007/s11207-008-9127-6.
- Maehara, H., Shibayama, T., Notsu, Y., Notsu, S., Honda, S., Nogami, D., and Shibata, K. Statistical properties of superflares on solar-type stars based on 1-min cadence data. *Earth, Planets, and Space*, 67:59, April 2015. doi: 10.1186/s40623-015-0217-z.
- Magara, T., Mineshige, S., Yokoyama, T., and Shibata, K. Numerical Simulation of Magnetic Reconnection in Eruptive Flares. *The Astrophysical Journal*, 466:1054, August 1996. doi: 10.1086/177575.
- Mandrini, C. H., Demoulin, P., Henoux, J. C., and Machado, M. E. Evidence for the interaction of large scale magnetic structures in solar flares. *Astronomy and Astrophysics*, 250:541–547, October 1991.
- Mandrini, C. H., Nakwacki, M. S., Attrill, G., van Driel-Gesztelyi, L., Démoulin, P., Dasso, S., and Elliott, H. Are CME-Related Dimmings Always a Simple Signature of Interplanetary Magnetic Cloud Footprints? *Solar Physics*, 244(1-2):25–43, August 2007. doi: 10.1007/s11207-007-9020-8.

- Mandrini, C. H., Schmieder, B., Démoulin, P., Guo, Y., and Cristiani, G. D. Topological Analysis of Emerging Bipole Clusters Producing Violent Solar Events. *Solar Physics*, 289(6):2041–2071, June 2014. doi: 10.1007/s11207-013-0458-6.
- Martin, S. F. Conditions for the Formation and Maintenance of Filaments (Invited Review). *Solar Physics*, 182(1):107–137, September 1998. doi: 10.1023/A:1005026814076.
- Masson, S., Pariat, E., Aulanier, G., and Schrijver, C. J. The Nature of Flare Ribbons in Coronal Null-Point Topology. *The Astrophysical Journal*, 700(1):559–578, July 2009. doi: 10.1088/0004-637X/700/1/559.
- Masson, S., Pariat, É., Valori, G., Deng, N., Liu, C., Wang, H., and Reid, H. Flux rope, hyperbolic flux tube, and late extreme ultraviolet phases in a non-eruptive circular-ribbon flare. *Astronomy and Astrophysics*, 604:A76, August 2017. doi: 10.1051/0004-6361/201629654.
- McAllister, A. H., Dryer, M., McIntosh, P., Singer, H., and Weiss, L. A large polar crown coronal mass ejection and a “problem” geomagnetic storm: April 14–23, 1994. *Journal of Geophysical Research*, 101(A6):13497–13516, June 1996. doi: 10.1029/96JA00510.
- McIntosh, P. S. The Classification of Sunspot Groups. *Solar Physics*, 125(2):251–267, September 1990. doi: 10.1007/BF00158405.
- McKenzie, D. E. and Canfield, R. C. Hinode XRT observations of a long-lasting coronal sigmoid. *Astronomy and Astrophysics*, 481(1):L65–L68, April 2008. doi: 10.1051/0004-6361:20079035.
- McKenzie, D. E. and Hudson, H. S. X-Ray Observations of Motions and Structure above a Solar Flare Arcade. *The Astrophysical Journal Letters*, 519(1):L93–L96, July 1999. doi: 10.1086/312110.
- Metcalf, T. R., Alexander, D., Hudson, H. S., and Longcope, D. W. TRACE and Yohkoh Observations of a White-Light Flare. *The Astrophysical Journal*, 595(1):483–492, September 2003. doi: 10.1086/377217.
- Mikić, Z. and Linker, J. A. The Initiation of coronal mass ejections by magnetic shear. *Washington DC American Geophysical Union Geophysical Monograph Series*, 99:57–64, January 1997. doi: 10.1029/GM099p0057.
- Miklenic, C., Veronig, A. M., Temmer, M., Möstl, C., and Biernat, H. K. Coronal Dimmings and the Early Phase of a CME Observed with STEREO and Hinode/EIS. *Solar Physics*, 273(1):125–142, October 2011. doi: 10.1007/s11207-011-9852-0.
- Moore, R. L. and Roumeliotis, G. *Triggering of Eruptive Flares - Destabilization of the Preflare Magnetic Field Configuration*, volume 399, page 69. 1992. doi: 10.1007/3-540-55246-4\_79.
- Moore, R. L., Sterling, A. C., Hudson, H. S., and Lemen, J. R. Onset of the Magnetic Explosion in Solar Flares and Coronal Mass Ejections. *The Astrophysical Journal*, 552(2):833–848, May 2001. doi: 10.1086/320559.
- Morgan, H. and Druckmüller, M. Multi-Scale Gaussian Normalization for Solar Image Processing. *Solar Physics*, 289(8):2945–2955, August 2014. doi: 10.1007/s11207-014-0523-9.
- Narukage, N. and Shibata, K. Statistical Analysis of Reconnection Inflows in Solar Flares Observed with SOHO EIT. *The Astrophysical Journal*, 637(2):1122–1134, February 2006. doi: 10.1086/498492.
- Nindos, A., Patsourakos, S., Vourlidas, A., and Tagikas, C. How Common Are Hot Magnetic Flux Ropes in the Low Solar Corona? A Statistical Study of EUV Observations. *The Astrophysical Journal*, 808(2):117, August 2015. doi: 10.1088/0004-637X/808/2/117.
- O’Dwyer, B., Del Zanna, G., Mason, H. E., Weber, M. A., and Tripathi, D. SDO/AIA response to coronal hole, quiet Sun, active region, and flare plasma. *Astronomy and Astrophysics*, 521:A21, October 2010. doi: 10.1051/0004-6361/201014872.
- Ohyama, M. and Shibata, K. X-Ray Plasma Ejection Associated with an Impulsive Flare on 1992 October 5: Physical Conditions of X-Ray Plasma Ejection. *The Astrophysical Journal*, 499(2):934–944, May 1998. doi: 10.1086/305652.

- Oka, M., Krucker, S., Hudson, H. S., and Saint-Hilaire, P. Electron Energy Partition in the Above-the-looptop Solar Hard X-Ray Sources. *The Astrophysical Journal*, 799(2):129, February 2015. doi: 10.1088/0004-637X/799/2/129.
- Olmedo, O. and Zhang, J. Partial Torus Instability. *The Astrophysical Journal*, 718(1):433–440, July 2010. doi: 10.1088/0004-637X/718/1/433.
- Orozco Suárez, D., Asensio Ramos, A., and Trujillo Bueno, J. Evidence for Rotational Motions in the Feet of a Quiescent Solar Prominence. *The Astrophysical Journal Letters*, 761(2):L25, December 2012. doi: 10.1088/2041-8205/761/2/L25.
- Pariat, E. and Démoulin, P. Estimation of the squashing degree within a three-dimensional domain. *Astronomy and Astrophysics*, 541:A78, May 2012. doi: 10.1051/0004-6361/201118515.
- Parker, E. N. Sweet’s Mechanism for Merging Magnetic Fields in Conducting Fluids. *Journal of Geophysical Research*, 62(4):509–520, December 1957. doi: 10.1029/JZ062i004p00509.
- Parker, E. N. The Solar-Flare Phenomenon and the Theory of Reconnection and Annihilation of Magnetic Fields. *Astrophysical Journal Supplement*, 8:177, July 1963. doi: 10.1086/190087.
- Parker, E. N. Spontaneous current sheets in magnetic fields : with applications to stellar x-rays. *Spontaneous current sheets in magnetic fields : with applications to stellar x-rays. International Series in Astronomy and Astrophysics*, 1, January 1994.
- Pesnell, W. D., Thompson, B. J., and Chamberlin, P. C. The Solar Dynamics Observatory (SDO). *Solar Physics*, 275(1-2):3–15, January 2012. doi: 10.1007/s11207-011-9841-3.
- Petkaki, P., Del Zanna, G., Mason, H. E., and Bradshaw, S. J. SDO AIA and EVE observations and modelling of solar flare loops. *Astronomy and Astrophysics*, 547:A25, November 2012. doi: 10.1051/0004-6361/201219812.
- Petschek, H. E. *Magnetic Field Annihilation*, volume 50, page 425. 1964.
- Phillips, K. J. H., Feldman, U., and Landi, E. *Ultraviolet and X-ray Spectroscopy of the Solar Atmosphere*. 2008.
- Poduval, B., DeForest, C. E., Schmelz, J. T., and Pathak, S. Point-spread Functions for the Extreme-ultraviolet Channels of SDO/AIA Telescopes. *The Astrophysical Journal*, 765(2):144, March 2013. doi: 10.1088/0004-637X/765/2/144.
- Polito, V., Reep, J. W., Reeves, K. K., Simões, P. J. A., Dudík, J., Del Zanna, G., Mason, H. E., and Golub, L. Simultaneous IRIS and Hinode/EIS Observations and Modelling of the 2014 October 27 X2.0 Class Flare. *The Astrophysical Journal*, 816(2):89, January 2016. doi: 10.3847/0004-637X/816/2/89.
- Polito, V., Galan, G., Reeves, K. K., and Musset, S. Possible Signatures of a Termination Shock in the 2014 March 29 X-class Flare Observed by IRIS. *The Astrophysical Journal*, 865(2):161, October 2018. doi: 10.3847/1538-4357/aadada.
- Pontin, D. I., Galsgaard, K., Hornig, G., and Priest, E. R. A fully magnetohydrodynamic simulation of three-dimensional non-null reconnection. *Physics of Plasmas*, 12(5):052307, May 2005. doi: 10.1063/1.1891005.
- Price, D. J., Pomoell, J., Lumme, E., and Kilpua, E. K. J. Time-dependent data-driven coronal simulations of AR 12673 from emergence to eruption. *Astronomy and Astrophysics*, 628:A114, August 2019. doi: 10.1051/0004-6361/201935535.
- Priest, E. R. and Démoulin, P. Three-dimensional magnetic reconnection without null points. 1. Basic theory of magnetic flipping. *Journal of Geophysical Research*, 100(A12):23443–23464, December 1995. doi: 10.1029/95JA02740.
- Priest, E. R. and Forbes, T. G. Magnetic Field Evolution during Prominence Eruptions and Two-Ribbon Flares. *Solar Physics*, 126(2):319–350, April 1990. doi: 10.1007/BF00153054.
- Priest, E. R. and Forbes, T. G. Magnetic Flipping: Reconnection in Three Dimensions Without Null Points. *Journal of Geophysical Research*, 97(A2):1521–1531, February 1992. doi: 10.1029/91JA02435.

- Priest, E. R. and Forbes, T. G. The magnetic nature of solar flares. *The Astronomy and Astrophysics Review*, 10(4):313–377, January 2002. doi: 10.1007/s001590100013.
- Priest, E. R. and Schrijver, C. J. Aspects of Three-Dimensional Magnetic Reconnection - (Invited Review). *Solar Physics*, 190:1–24, December 1999. doi: 10.1023/A:1005248007615.
- Priest, E. R. and Titov, V. S. Magnetic Reconnection at Three-Dimensional Null Points. *Philosophical Transactions of the Royal Society of London Series A*, 354(1721):2951–2992, December 1996. doi: 10.1098/rsta.1996.0136.
- Priest, E. *Magnetohydrodynamics of the Sun*. 2014. doi: 10.1017/CBO9781139020732.
- Priest, E. and Forbes, T. *Magnetic Reconnection*. 2000.
- Priest, E. R. Three-dimensional reconnection on the Sun. *Earth, Planets, and Space*, 53:483–490, June 2001. doi: 10.1186/BF03353259.
- Qiu, J., Longcope, D. W., Cassak, P. A., and Priest, E. R. Elongation of Flare Ribbons. *The Astrophysical Journal*, 838:17, March 2017. doi: 10.3847/1538-4357/aa6341.
- Qiu, J., Lee, J., Gary, D. E., and Wang, H. Motion of Flare Footpoint Emission and Inferred Electric Field in Reconnecting Current Sheets. *The Astrophysical Journal*, 565(2):1335–1347, February 2002. doi: 10.1086/324706.
- Qiu, J., Liu, W., Hill, N., and Kazachenko, M. Reconnection and Energetics in Two-ribbon Flares: A Revisit of the Bastille-day Flare. *The Astrophysical Journal*, 725(1):319–330, December 2010. doi: 10.1088/0004-637X/725/1/319.
- Reames, D. V. Particle acceleration at the Sun and in the heliosphere. *Space Science Reviews*, 90: 413–491, October 1999. doi: 10.1023/A:1005105831781.
- Rees-Crockford, T., Bloomfield, D. S., Scullion, E., and Park, S. H. 2D and 3D Analysis of a Torus-unstable Quiet-Sun Prominence Eruption. *The Astrophysical Journal*, 897(1):35, July 2020. doi: 10.3847/1538-4357/ab92a0.
- Reeves, K. K. and Golub, L. Atmospheric Imaging Assembly Observations of Hot Flare Plasma. *The Astrophysical Journal Letters*, 727(2):L52, February 2011. doi: 10.1088/2041-8205/727/2/L52.
- Roussev, I. I., Forbes, T. G., Gombosi, T. I., Sokolov, I. V., DeZeeuw, D. L., and Birn, J. A Three-dimensional Flux Rope Model for Coronal Mass Ejections Based on a Loss of Equilibrium. *The Astrophysical Journal Letters*, 588(1):L45–L48, May 2003. doi: 10.1086/375442.
- Russell, A. J. B., Simões, P. J. A., and Fletcher, L. A unified view of coronal loop contraction and oscillation in flares. *Astronomy and Astrophysics*, 581:A8, September 2015. doi: 10.1051/0004-6361/201525746.
- Rust, D. M. Coronal Disturbances and Their Terrestrial Effects. *Space Science Reviews*, 34(1):21–36, January 1983. doi: 10.1007/BF00221193.
- Rutten, R. J. On the Nature of the Solar Chromosphere. In Leibacher, J., Stein, R. F., and Uitenbroek, H., editors, *Solar MHD Theory and Observations: A High Spatial Resolution Perspective*, volume 354 of *Astronomical Society of the Pacific Conference Series*, page 276, December 2006.
- Sakao, T., Kano, R., Narukage, N., Kotoku, J., Bando, T., DeLuca, E. E., Lundquist, L. L., Tsuneta, S., Harra, L. K., Katsukawa, Y., Kubo, M., Hara, H., Matsuzaki, K., Shimojo, M., Bookbinder, J. A., Golub, L., Korreck, K. E., Su, Y., Shibasaki, K., Shimizu, T., and Nakatani, I. Continuous Plasma Outflows from the Edge of a Solar Active Region as a Possible Source of Solar Wind. *Science*, 318(5856):1585, December 2007. doi: 10.1126/science.1147292.
- Savage, S. L., McKenzie, D. E., Reeves, K. K., Forbes, T. G., and Longcope, D. W. Reconnection Outflows and Current Sheet Observed with Hinode/XRT in the 2008 April 9 “Cartwheel CME” Flare. *The Astrophysical Journal*, 722(1):329–342, October 2010. doi: 10.1088/0004-637X/722/1/329.
- Savage, S. L., McKenzie, D. E., and Reeves, K. K. Re-interpretation of Supra-arcade Downflows in Solar Flares. *The Astrophysical Journal Letters*, 747(2):L40, March 2012. doi: 10.1088/2041-8205/747/2/L40.

- Savcheva, A., Pariat, E., McKillop, S., McCauley, P., Hanson, E., Su, Y., Werner, E., and DeLuca, E. E. The Relation between Solar Eruption Topologies and Observed Flare Features. I. Flare Ribbons. *The Astrophysical Journal*, 810(2):96, September 2015. doi: 10.1088/0004-637X/810/2/96.
- Savcheva, A. S., van Ballegooijen, A. A., and DeLuca, E. E. Field Topology Analysis of a Long-lasting Coronal Sigmoid. *The Astrophysical Journal*, 744(1):78, January 2012. doi: 10.1088/0004-637X/744/1/78.
- Scherrer, P. H., Bogart, R. S., Bush, R. I., Hoeksema, J. T., Kosovichev, A. G., Schou, J., Rosenberg, W., Springer, L., Tarbell, T. D., Title, A., Wolfson, C. J., Zayer, I., and MDI Engineering Team. The Solar Oscillations Investigation - Michelson Doppler Imager. *Solar Physics*, 162(1-2):129–188, December 1995. doi: 10.1007/BF00733429.
- Scherrer, P. H., Schou, J., Bush, R. I., Kosovichev, A. G., Bogart, R. S., Hoeksema, J. T., Liu, Y., Duvall, T. L., Zhao, J., Title, A. M., Schrijver, C. J., Tarbell, T. D., and Tomczyk, S. The Helioseismic and Magnetic Imager (HMI) Investigation for the Solar Dynamics Observatory (SDO). *Solar Physics*, 275:207–227, January 2012. doi: 10.1007/s11207-011-9834-2.
- Schindler, K., Hesse, M., and Birn, J. General magnetic reconnection, parallel electric fields, and helicity. *Journal of Geophysical Research*, 93(A6):5547–5557, June 1988. doi: 10.1029/JA093iA06p05547.
- Schmahl, E. J. and Hurford, G. J. RHESSI Observations of the Size Scales of Solar Hard X-ray Sources. *Solar Physics*, 210(1):273–286, November 2002. doi: 10.1023/A:1022484822851.
- Schmelz, J. T. and Winebarger, A. R. What can observations tell us about coronal heating? *Philosophical Transactions of the Royal Society of London Series A*, 373(2042):20140257–20140257, April 2015. doi: 10.1098/rsta.2014.0257.
- Schmelz, J. T., Jenkins, B. S., Worley, B. T., Anderson, D. J., Pathak, S., and Kimble, J. A. Isothermal and Multithermal Analysis of Coronal Loops Observed with AIA. *The Astrophysical Journal*, 731(1):49, April 2011. doi: 10.1088/0004-637X/731/1/49.
- Schmelz, J. T., Reames, D. V., von Steiger, R., and Basu, S. Composition of the Solar Corona, Solar Wind, and Solar Energetic Particles. *The Astrophysical Journal*, 755(1):33, August 2012. doi: 10.1088/0004-637X/755/1/33.
- Schmieder, B., Forbes, T. G., Malherbe, J. M., and Machado, M. E. Evidence for Gentle Chromospheric Evaporation during the Gradual Phase of Large Solar Flares. *The Astrophysical Journal*, 317:956, June 1987. doi: 10.1086/165344.
- Schmieder, B., Raadu, M. A., and Wiik, J. E. Fine structure of solar filaments. II - Dynamics of threads and footpoints. *Astronomy and Astrophysics*, 252(1):353–365, December 1991.
- Schmieder, B., Heinzel, P., Wiik, J. E., Lemen, J., Anwar, B., Kotrc, P., and Hiei, E. Relation between Cool and Hot Post-Flare Loops of 26 June 1992 Derived from Optical and X-Ray (SXT-YOHKOH) Observations. *Solar Physics*, 156(2):337–361, February 1995. doi: 10.1007/BF00670231.
- Schmieder, B., Delannée, C., Yong, D. Y., Vial, J. C., and Madjarska, M. Multi-wavelength study of the slow “disparition brusque” of a filament observed with SOHO. *Astronomy and Astrophysics*, 358:728–740, June 2000.
- Schmieder, B., Mandrini, C. H., Démoulin, P., Aulanier, G., Li, H., and Berlicki, A. What is the role of magnetic null points in large flares? *Advances in Space Research*, 39(12):1840–1846, January 2007. doi: 10.1016/j.asr.2007.03.058.
- Schmieder, B., Aulanier, G., and Vršnak, B. Flare-CME Models: An Observational Perspective (Invited Review). *Solar Physics*, 290(12):3457–3486, December 2015. doi: 10.1007/s11207-015-0712-1.
- Schmieder, B. and Aulanier, G. What are the physical mechanisms of eruptions and CMEs? *Advances in Space Research*, 49(11):1598–1606, June 2012. doi: 10.1016/j.asr.2011.10.023.
- Schou, J., Scherrer, P. H., Bush, R. I., Wachter, R., Couvidat, S., Rabello-Soares, M. C., Bogart, R. S., Hoeksema, J. T., Liu, Y., Duvall, T. L., Akin, D. J., Allard, B. A., Miles, J. W., Rairden, R., Shine, R. A., Tarbell, T. D., Title, A. M., Wolfson, C. J., Elmore, D. F., Norton, A. A., and Tomczyk, S. Design and Ground Calibration of the Helioseismic and Magnetic Imager (HMI) Instrument on the Solar Dynamics Observatory (SDO). *Solar Physics*, 275(1-2):229–259, January 2012. doi: 10.1007/s11207-011-9842-2.

- Schrijver, C. J., Beer, J., Baltensperger, U., Cliver, E. W., Güdel, M., Hudson, H. S., McCracken, K. G., Osten, R. A., Peter, T., Soderblom, D. R., Usoskin, I. G., and Wolff, E. W. Estimating the frequency of extremely energetic solar events, based on solar, stellar, lunar, and terrestrial records. *Journal of Geophysical Research (Space Physics)*, 117(A8):A08103, August 2012. doi: 10.1029/2012JA017706.
- Schrijver, C. J., Aulanier, G., Title, A. M., Pariat, E., and Delannée, C. The 2011 February 15 X2 Flare, Ribbons, Coronal Front, and Mass Ejection: Interpreting the Three-dimensional Views from the Solar Dynamics Observatory and STEREO Guided by Magnetohydrodynamic Flux-rope Modeling. *The Astrophysical Journal*, 738(2):167, September 2011. doi: 10.1088/0004-637X/738/2/167.
- Sharykin, I. N. and Kosovichev, A. G. Fine Structure of Flare Ribbons and Evolution of Electric Currents. *The Astrophysical Journal Letters*, 788(1):L18, June 2014. doi: 10.1088/2041-8205/788/1/L18.
- Shibata, K., Masuda, S., Shimojo, M., Hara, H., Yokoyama, T., Tsuneta, S., Kosugi, T., and Ogawara, Y. Hot-Plasma Ejections Associated with Compact-Loop Solar Flares. *The Astrophysical Journal Letters*, 451:L83, October 1995. doi: 10.1086/309688.
- Shibata, K. and Magara, T. Solar Flares: Magnetohydrodynamic Processes. *Living Reviews in Solar Physics*, 8:6, December 2011. doi: 10.12942/lrsp-2011-6.
- Shimizu, T. Energetics and Occurrence Rate of Active-Region Transient Brightenings and Implications for the Heating of the Active-Region Corona. *Publications of the Astronomical Society of Japan*, 47:251–263, April 1995.
- Shimojo, M., Narukage, N., Kano, R., Sakao, T., Tsuneta, S., Shibasaki, K., Cirtain, J. W., Lundquist, L. L., Reeves, K. K., and Savcheva, A. Fine Structures of Solar X-Ray Jets Observed with the X-Ray Telescope aboard Hinode. *Publications of the Astronomical Society of Japan*, 59:S745, November 2007. doi: 10.1093/pasj/59.sp3.S745.
- Shiota, D., Isobe, H., Chen, P. F., Yamamoto, T. T., Sakajiri, T., and Shibata, K. Self-Consistent Magnetohydrodynamic Modeling of a Coronal Mass Ejection, Coronal Dimming, and a Giant Cusp-shaped Arcade Formation. *The Astrophysical Journal Letters*, 634(1):663–678, November 2005. doi: 10.1086/496943.
- Simões, P. J. A., Fletcher, L., Hudson, H. S., and Russell, A. J. B. Implosion of Coronal Loops during the Impulsive Phase of a Solar Flare. *The Astrophysical Journal*, 777(2):152, November 2013. doi: 10.1088/0004-637X/777/2/152.
- Sobotka, M., Dudík, J., Denker, C., Balthasar, H., Jurčák, J., Liu, W., Berkefeld, T., Collados Vera, M., Feller, A., Hofmann, A., Kneer, F., Kuckein, C., Lagg, A., Louis, R. E., von der Lühe, O., Nicklas, H., Schlichenmaier, R., Schmidt, D., Schmidt, W., Sigwarth, M., Solanki, S. K., Soltau, D., Staude, J., Strassmeier, K. G., Volkmer, R., and Waldmann, T. Slipping reconnection in a solar flare observed in high resolution with the GREGOR solar telescope. *Astronomy and Astrophysics*, 596:A1, November 2016. doi: 10.1051/0004-6361/201527966.
- Solanki, S. K., Inhester, B., and Schüssler, M. The solar magnetic field. *Reports on Progress in Physics*, 69(3):563–668, March 2006. doi: 10.1088/0034-4885/69/3/R02.
- Somov, B. V. and Kosugi, T. Collisionless Reconnection and High-Energy Particle Acceleration in Solar Flares. *The Astrophysical Journal*, 485(2):859–868, August 1997. doi: 10.1086/304449.
- Sterling, A. C. and Hudson, H. S. Yohkoh SXT Observations of X-Ray “Dimming” Associated with a Halo Coronal Mass Ejection. *The Astrophysical Journal Letters*, 491(1):L55–L58, December 1997. doi: 10.1086/311043.
- Sterling, A. C., Moore, R. L., and Freeland, S. L. Insights into Filament Eruption Onset from Solar Dynamics Observatory Observations. *The Astrophysical Journal Letters*, 731(1):L3, April 2011. doi: 10.1088/2041-8205/731/1/L3.
- Stix, M. *The sun: an introduction*. 2002.
- Sturrock, P. A. Model of the High-Energy Phase of Solar Flares. *Nature*, 211:695–697, August 1966. doi: 10.1038/211695a0.

- Sun, X., Hoeksema, J. T., Liu, Y., Aulanier, G., Su, Y., Hannah, I. G., and Hock, R. A. Hot Spine Loops and the Nature of a Late-phase Solar Flare. *The Astrophysical Journal*, 778(2):139, December 2013. doi: 10.1088/0004-637X/778/2/139.
- SunPy Community, Barnes, W. T., Bobra, M. G., Christe, S. D., Freij, N., Hayes, L. A., Ireland, J., Mumford, S., Perez-Suarez, D., Ryan, D. F., Shih, A. Y., Chanda, P., Glogowski, K., Hewett, R., Hughitt, V. K., Hill, A., Hiware, K., Inglis, A., Kirk, M. S. F., Konge, S., Mason, J. P., Maloney, S. A., Murray, S. A., Panda, A., Park, J., Pereira, T. M. D., Reardon, K., Savage, S., Sipócz, B. M., Stansby, D., Jain, Y., Taylor, G., Yadav, T., Rajul, and Dang, T. K. The SunPy Project: Open Source Development and Status of the Version 1.0 Core Package. *The Astrophysical Journal*, 890(1):68, February 2020. doi: 10.3847/1538-4357/ab4f7a.
- Sweet, P. A. The Neutral Point Theory of Solar Flares. In Lehnert, B., editor, *Electromagnetic Phenomena in Cosmical Physics*, volume 6, page 123, January 1958.
- Syntelis, P., Archontis, V., and Tsinganos, K. Recurrent CME-like Eruptions in Emerging Flux Regions. I. On the Mechanism of Eruptions. *The Astrophysical Journal*, 850(1):95, November 2017. doi: 10.3847/1538-4357/aa9612.
- Syntelis, P., Archontis, V., and Tsinganos, K. Recurrent CME-like Eruptions in Emerging Flux Regions. II. Scaling of Energy and Collision of Successive Eruptions. *The Astrophysical Journal*, 876(1):61, May 2019. doi: 10.3847/1538-4357/ab16d2.
- Tassev, S. and Savcheva, A. QSL Squasher: A Fast Quasi-separatrix Layer Map Calculator. *The Astrophysical Journal*, 840(2):89, May 2017. doi: 10.3847/1538-4357/aa6f06.
- Testa, P., De Pontieu, B., Martínez-Sykora, J., DeLuca, E., Hansteen, V., Cirtain, J., Winebarger, A., Golub, L., Kobayashi, K., Korreck, K., Kuzin, S., Walsh, R., DeForest, C., Title, A., and Weber, M. Observing Coronal Nanoflares in Active Region Moss. *The Astrophysical Journal Letters*, 770(1):L1, June 2013. doi: 10.1088/2041-8205/770/1/L1.
- Thalmann, J. K., Su, Y., Temmer, M., and Veronig, A. M. The Confined X-class Flares of Solar Active Region 2192. *The Astrophysical Journal Letters*, 801(2):L23, March 2015. doi: 10.1088/2041-8205/801/2/L23.
- Thompson, B. J., Plunkett, S. P., Gurman, J. B., Newmark, J. S., St. Cyr, O. C., and Michels, D. J. SOHO/EIT observations of an Earth-directed coronal mass ejection on May 12, 1997. *Geophysical Research Letters*, 25(14):2465–2468, January 1998. doi: 10.1029/98GL50429.
- Thompson, B. J., Cliver, E. W., Nitta, N., Delannée, C., and Delaboudinière, J. P. Coronal dimmings and energetic CMEs in April-May 1998. *Geophysical Research Letters*, 27(10):1431–1434, May 2000. doi: 10.1029/1999GL003668.
- Tian, H., Li, G., Reeves, K. K., Raymond, J. C., Guo, F., Liu, W., Chen, B., and Murphy, N. A. Imaging and Spectroscopic Observations of Magnetic Reconnection and Chromospheric Evaporation in a Solar Flare. *The Astrophysical Journal Letters*, 797(2):L14, December 2014. doi: 10.1088/2041-8205/797/2/L14.
- Title, A. M., Tarbell, T. D., Topka, K. P., Ferguson, S. H., Shine, R. A., and SOUP Team. Statistical Properties of Solar Granulation Derived from the SOUP Instrument on Spacelab 2. *The Astrophysical Journal*, 336:475, January 1989. doi: 10.1086/167026.
- Titov, V. S. and Démoulin, P. Basic topology of twisted magnetic configurations in solar flares. *Astronomy and Astrophysics*, 351:707–720, November 1999.
- Titov, V. S., Priest, E. R., and Démoulin, P. Conditions for the appearance of “bald patches” at the solar surface. *Astronomy and Astrophysics*, 276:564, September 1993.
- Titov, V. S., Galsgaard, K., and Neukirch, T. Magnetic Pinching of Hyperbolic Flux Tubes. I. Basic Estimations. *The Astrophysical Journal*, 582(2):1172–1189, January 2003. doi: 10.1086/344799.
- Titov, V. S., Hornig, G., and Démoulin, P. Theory of magnetic connectivity in the solar corona. *Journal of Geophysical Research (Space Physics)*, 107(A8):1164, August 2002. doi: 10.1029/2001JA000278.
- Tomczak, M. and Ciborski, T. Footpoint versus loop-top hard X-ray emission sources in solar flares. *Astronomy and Astrophysics*, 461(1):315–323, January 2007. doi: 10.1051/0004-6361:20066115.

- Török, T. and Kliem, B. The evolution of twisting coronal magnetic flux tubes. *Astronomy and Astrophysics*, 406:1043–1059, August 2003. doi: 10.1051/0004-6361:20030692.
- Török, T. and Kliem, B. Confined and Ejective Eruptions of Kink-unstable Flux Ropes. *The Astrophysical Journal Letters*, 630(1):L97–L100, September 2005. doi: 10.1086/462412.
- Török, T. and Kliem, B. Numerical simulations of fast and slow coronal mass ejections. *Astronomische Nachrichten*, 328(8):743, October 2007. doi: 10.1002/asna.200710795.
- Török, T., Aulanier, G., Schmieder, B., Reeves, K. K., and Golub, L. Fan-Spine Topology Formation Through Two-Step Reconnection Driven by Twisted Flux Emergence. *The Astrophysical Journal*, 704(1):485–495, October 2009. doi: 10.1088/0004-637X/704/1/485.
- Török, T., Berger, M. A., and Kliem, B. The writhe of helical structures in the solar corona. *Astronomy and Astrophysics*, 516:A49, June 2010. doi: 10.1051/0004-6361/200913578.
- Tripathi, D., Isobe, H., and Mason, H. E. On the propagation of brightening after filament/prominence eruptions, as seen by SoHO-EIT. *Astronomy and Astrophysics*, 453(3):1111–1116, July 2006. doi: 10.1051/0004-6361:20064993.
- Tsuneta, S. Particle Acceleration and Magnetic Reconnection in Solar Flares. *Publications of the Astronomical Society of Japan*, 47:691–697, October 1995.
- Tsuneta, S. Structure and Dynamics of Magnetic Reconnection in a Solar Flare. *The Astrophysical Journal*, 456:840, January 1996. doi: 10.1086/176701.
- Tsuneta, S. and Naito, T. Fermi Acceleration at the Fast Shock in a Solar Flare and the Impulsive Loop-Top Hard X-Ray Source. *The Astrophysical Journal*, 495(1):L67–L70, March 1998. doi: 10.1086/311207.
- Tsuneta, S., Hara, H., Shimizu, T., Acton, L. W., Strong, K. T., Hudson, H. S., and Ogawara, Y. Observation of a Solar Flare at the Limb with the YOHKOH Soft X-Ray Telescope. *Publications of the Astronomical Society of Japan*, 44:L63–L69, October 1992.
- Tsurutani, B. T., Judge, D. L., Guarnieri, F. L., Gangopadhyay, P., Jones, A. R., Nuttall, J., Zambon, G. A., Didkovsky, L., Manucci, A. J., Iijima, B., Meier, R. R., Immel, T. J., Woods, T. N., Prasad, S., Floyd, L., Huba, J., Solomon, S. C., Straus, P., and Viereck, R. The October 28, 2003 extreme EUV solar flare and resultant extreme ionospheric effects: Comparison to other Halloween events and the Bastille Day event. *Geophysical Research Letters*, 32(3):L03S09, January 2005. doi: 10.1029/2004GL021475.
- Ugarte-Urra, I., Warren, H. P., and Brooks, D. H. Active Region Transition Region Loop Populations and Their Relationship to the Corona. *The Astrophysical Journal*, 695(1):642–651, April 2009. doi: 10.1088/0004-637X/695/1/642.
- van Ballegoijen, A. A. and Martens, P. C. H. Formation and Eruption of Solar Prominences. *The Astrophysical Journal*, 343:971, August 1989. doi: 10.1086/167766.
- van Driel-Gesztelyi, L., Wiik, J. E., Schmieder, B., Tarbell, T., Kitai, R., Funakoshi, Y., and Anwar, B. Post-Flare Loops of 26 June 1992 - IV. Formation and Expansion of Hot and Cool Loops. *Solar Physics*, 174:151–162, August 1997. doi: 10.1023/A:1004993809061.
- Vanninathan, K., Veronig, A. M., Dissauer, K., and Temmer, M. Plasma Diagnostics of Coronal Dimming Events. *The Astrophysical Journal*, 857(1):62, April 2018. doi: 10.3847/1538-4357/aab09a.
- Varady, M., Karlický, M., Moravec, Z., and Kašparová, J. Modifications of thick-target model: re-acceleration of electron beams by static and stochastic electric fields. *Astronomy and Astrophysics*, 563:A51, March 2014. doi: 10.1051/0004-6361/201322391.
- Vasantharaju, N., Vemareddy, P., Ravindra, B., and Doddamani, V. H. Finding the Critical Decay Index in Solar Prominence Eruptions. *The Astrophysical Journal*, 885(1):89, November 2019. doi: 10.3847/1538-4357/ab4793.
- Vasyliunas, V. M. Theoretical models of magnetic field line merging, 1. *Reviews of Geophysics and Space Physics*, 13:303–336, February 1975. doi: 10.1029/RG013i001p00303.

- Vernazza, J. E., Avrett, E. H., and Loeser, R. Structure of the solar chromosphere. III. Models of the EUV brightness components of the quiet sun. *Astrophysical Journal Supplement Series*, 45:635–725, April 1981. doi: 10.1086/190731.
- Veronig, A. M., Karlický, M., Vršnak, B., Temmer, M., Magdaleníć, J., Dennis, B. R., Otruba, W., and Pötzi, W. X-ray sources and magnetic reconnection in the X3.9 flare of 2003 November 3. *Astronomy and Astrophysics*, 446(2):675–690, February 2006. doi: 10.1051/0004-6361:20053112.
- Veronig, A. M., Gömöry, P., Dissauer, K., Temmer, M., and Vanninathan, K. Spectroscopy and Differential Emission Measure Diagnostics of a Coronal Dimming Associated with a Fast Halo CME. *The Astrophysical Journal*, 879(2):85, July 2019. doi: 10.3847/1538-4357/ab2712.
- Vourlidas, A., Lynch, B. J., Howard, R. A., and Li, Y. How Many CMEs Have Flux Ropes? Deciphering the Signatures of Shocks, Flux Ropes, and Prominences in Coronagraph Observations of CMEs. *Solar Physics*, 284(1):179–201, May 2013. doi: 10.1007/s11207-012-0084-8.
- Švestka, Z. and Cliver, E. W. *History and Basic Characteristics of Eruptive Flares*, volume 399, page 1. 1992. doi: 10.1007/3-540-55246-4-70.
- Švestka, Z. Optical Observations of Solar Flares. *Space Science Reviews*, 5(3):388–418, May 1966. doi: 10.1007/BF02653250.
- Švestka, Z. Solar Flares - the Gradual Phase. *Solar Physics*, 121(1-2):399–417, March 1989. doi: 10.1007/BF00161709.
- Švestka, Z. Varieties of Coronal Mass Ejections and Their Relation to Flares. *Space Science Reviews*, 95:135–146, January 2001.
- Švestka, Z. The Misnomer of “Post-Flare Loops”. *Solar Physics*, 246(2):393–397, December 2007. doi: 10.1007/s11207-007-9088-1.
- Wang, H. and Liu, C. Signatures of Magnetic Flux Ropes in the Low Solar Atmosphere Observed in High Resolution. *Frontiers in Astronomy and Space Sciences*, 6:18, April 2019. doi: 10.3389/fspas.2019.00018.
- Wang, J., Jiang, C., Yuan, D., and Zou, P. The Causes of Peripheral Coronal Loop Contraction and Disappearance Revealed in a Magnetohydrodynamic Simulation of Solar Eruption. *The Astrophysical Journal*, 911(1):2, April 2021. doi: 10.3847/1538-4357/abe637.
- Wang, Y., Su, Y., Shen, J., Yang, X., Cao, W., and Ji, H. High-resolution He I 10830 Å Narrowband Imaging for an M-class Flare. II. Multiple Hot Channels: Their Origin and Destination. *The Astrophysical Journal*, 859(2):148, June 2018. doi: 10.3847/1538-4357/aac0f7.
- Wang, Y. and Zhang, J. A Comparative Study between Eruptive X-Class Flares Associated with Coronal Mass Ejections and Confined X-Class Flares. *The Astrophysical Journal*, 665(2):1428–1438, August 2007. doi: 10.1086/519765.
- Warren, H. P. and Warshall, A. D. Ultraviolet Flare Ribbon Brightenings and the Onset of Hard X-Ray Emission. *The Astrophysical Journal Letters*, 560(1):L87–L90, October 2001. doi: 10.1086/324060.
- Warren, H. P., Winebarger, A. R., and Brooks, D. H. Evidence for Steady Heating: Observations of an Active Region Core with Hinode and TRACE. *The Astrophysical Journal*, 711(1):228–238, March 2010. doi: 10.1088/0004-637X/711/1/228.
- Warren, H. P., Brooks, D. H., and Winebarger, A. R. Constraints on the Heating of High-temperature Active Region Loops: Observations from Hinode and the Solar Dynamics Observatory. *The Astrophysical Journal*, 734(2):90, June 2011a. doi: 10.1088/0004-637X/734/2/90.
- Warren, H. P., O’Brien, C. M., and Sheeley, J., Neil R. Observations of Reconnecting Flare Loops with the Atmospheric Imaging Assembly. *The Astrophysical Journal*, 742(2):92, December 2011b. doi: 10.1088/0004-637X/742/2/92.
- Watanabe, T., Hara, H., Sterling, A. C., and Harra, L. K. Production of High-temperature Plasmas During the Early Phases of a C9.7 Flare. *The Astrophysical Journal*, 719(1):213–219, August 2010. doi: 10.1088/0004-637X/719/1/213.
- Webb, D. F. and Hundhausen, A. J. Activity Associated with the Solar Origin of Coronal Mass Ejections. *Solar Physics*, 108(2):383–401, September 1987. doi: 10.1007/BF00214170.

- Webb, D. F., Cliver, E. W., Crooker, N. U., Cry, O. C. S., and Thompson, B. J. Relationship of halo coronal mass ejections, magnetic clouds, and magnetic storms. *Journal of Geophysical Research*, 105(A4):7491–7508, April 2000. doi: 10.1029/1999JA000275.
- Webb, D. F. and Howard, T. A. Coronal Mass Ejections: Observations. *Living Reviews in Solar Physics*, 9(1):3, June 2012. doi: 10.12942/lrsp-2012-3.
- Wiegelmann, T. Nonlinear force-free modeling of the solar coronal magnetic field. *Journal of Geophysical Research (Space Physics)*, 113(A3):A03S02, March 2008. doi: 10.1029/2007JA012432.
- Wolfson, R. and Saran, S. Energetics of Coronal Mass Ejections: Role of the Streamer Cavity. *The Astrophysical Journal*, 499(1):496–503, May 1998. doi: 10.1086/305619.
- Woods, T. N., Eparvier, F. G., Hock, R., Jones, A. R., Woodraska, D., Judge, D., Didkovsky, L., Lean, J., Mariska, J., Warren, H., McMullin, D., Chamberlin, P., Berthiaume, G., Bailey, S., Fuller-Rowell, T., Sojka, J., Tobiska, W. K., and Viereck, R. Extreme Ultraviolet Variability Experiment (EVE) on the Solar Dynamics Observatory (SDO): Overview of Science Objectives, Instrument Design, Data Products, and Model Developments. *Solar Physics*, 275(1-2):115–143, January 2012. doi: 10.1007/s11207-009-9487-6.
- Wuelser, J.-P., Canfield, R. C., Acton, L. W., Culhane, J. L., Phillips, A., Fludra, A., Sakao, T., Masuda, S., Kosugi, T., and Tsuneta, S. Multispectral Observations of Chromospheric Evaporation in the 1991 November 15 X-Class Solar Flare. *The Astrophysical Journal*, 424:459, March 1994. doi: 10.1086/173903.
- Wuelser, J.-P., Lemen, J. R., Tarbell, T. D., Wolfson, C. J., Cannon, J. C., Carpenter, B. A., Duncan, D. W., Gradwohl, G. S., Meyer, S. B., Moore, A. S., Navarro, R. L., Pearson, J. D., Rossi, G. R., Springer, L. A., Howard, R. A., Moses, J. D., Newmark, J. S., Delaboudiniere, J.-P., Artzner, G. E., Auchere, F., Bougnet, M., Bouyries, P., Bridou, F., Clotaire, J.-Y., Colas, G., Delmotte, F., Jerome, A., Lamare, M., Mercier, R., Mullot, M., Ravet, M.-F., Song, X., Bothmer, V., and Deutsch, W. EUVI: the STEREO-SECCHI extreme ultraviolet imager. In Fineschi, S. and Gummin, M. A., editors, *Telescopes and Instrumentation for Solar Astrophysics*, volume 5171 of *Society of Photo-Optical Instrumentation Engineers (SPIE) Conference Series*, pages 111–122, February 2004. doi: 10.1117/12.506877.
- Xing, C., Cheng, X., and Ding, M. D. Evolution of the Toroidal Flux of CME Flux Ropes during Eruption. *The Innovation*, 1(3):100059, November 2020. doi: 10.1016/j.xinn.2020.100059.
- Xue, Z., Yan, X., Cheng, X., Yang, L., Su, Y., Kliem, B., Zhang, J., Liu, Z., Bi, Y., Xiang, Y., Yang, K., and Zhao, L. Observing the release of twist by magnetic reconnection in a solar filament eruption. *Nature Communications*, 7:11837, June 2016. doi: 10.1038/ncomms11837.
- Yan, X. L., Yang, L. H., Xue, Z. K., Mei, Z. X., Kong, D. F., Wang, J. C., and Li, Q. L. Simultaneous Observation of a Flux Rope Eruption and Magnetic Reconnection during an X-class Solar Flare. *The Astrophysical Journal Letters*, 853(1):L18, January 2018. doi: 10.3847/2041-8213/aaa6c2.
- Yang, Y.-H., Cheng, C. Z., Krucker, S., Lin, R. P., and Ip, W. H. A Statistical Study of Hard X-Ray Footpoint Motions in Large Solar Flares. *The Astrophysical Journal*, 693(1):132–139, March 2009. doi: 10.1088/0004-637X/693/1/132.
- Yashiro, S., Gopalswamy, N., Akiyama, S., Michalek, G., and Howard, R. A. Visibility of coronal mass ejections as a function of flare location and intensity. *Journal of Geophysical Research (Space Physics)*, 110(A12):A12S05, December 2005. doi: 10.1029/2005JA011151.
- Yokoyama, T., Akita, K., Morimoto, T., Inoue, K., and Newmark, J. Clear Evidence of Reconnection Inflow of a Solar Flare. *The Astrophysical Journal Letters*, 546(1):L69–L72, January 2001. doi: 10.1086/318053.
- Zarro, D. M., Slater, G. L., and Freeland, S. L. Impulsive Phase Soft X-Ray Blueshifts at a Loop Footpoint. *The Astrophysical Journal Letters*, 333:L99, October 1988. doi: 10.1086/185296.
- Zemanová, A., Dudík, J., Aulanier, G., Thalmann, J. K., and Gömöry, P. Observations of a Footpoint Drift of an Erupting Flux Rope. *The Astrophysical Journal*, 883(1):96, September 2019. doi: 10.3847/1538-4357/ab3926.
- Zhang, J., Cheng, X., and Ding, M.-D. Observation of an evolving magnetic flux rope before and during a solar eruption. *Nature Communications*, 3:747, March 2012. doi: 10.1038/ncomms1753.

- Zhang, J., Li, T., and Yang, S. Secondary Flare Ribbons Observed by the Solar Dynamics Observatory. *The Astrophysical Journal Letters*, 782(2):L27, February 2014. doi: 10.1088/2041-8205/782/2/L27.
- Zhao, J., Gilchrist, S. A., Aulanier, G., Schmieder, B., Pariat, E., and Li, H. Hooked Flare Ribbons and Flux-rope-related QSL Footprints. *The Astrophysical Journal*, 823(1):62, May 2016. doi: 10.3847/0004-637X/823/1/62.
- Zheng, R., Korsós, M. B., and Erdélyi, R. Semicircular-like Secondary Flare Ribbons Associated with a Failed Eruption. *The Astrophysical Journal*, 809(1):45, August 2015. doi: 10.1088/0004-637X/809/1/45.
- Zhou, G., Wang, J., and Cao, Z. Correlation between halo coronal mass ejections and solar surface activity. *Astronomy and Astrophysics*, 397:1057–1067, January 2003. doi: 10.1051/0004-6361:20021463.
- Zhu, C., Liu, R., Alexander, D., and McAteer, R. T. J. Observation of the Evolution of a Current Sheet in a Solar Flare. *The Astrophysical Journal Letters*, 821(2):L29, April 2016. doi: 10.3847/2041-8205/821/2/L29.
- Zuccarello, F. P., Seaton, D. B., Mierla, M., Poedts, S., Rachmeler, L. A., Romano, P., and Zuccarello, F. Observational Evidence of Torus Instability as Trigger Mechanism for Coronal Mass Ejections: The 2011 August 4 Filament Eruption. *The Astrophysical Journal*, 785(2):88, April 2014. doi: 10.1088/0004-637X/785/2/88.
- Zuccarello, F. P., Aulanier, G., and Gilchrist, S. A. Critical Decay Index at the Onset of Solar Eruptions. *The Astrophysical Journal*, 814(2):126, December 2015. doi: 10.1088/0004-637X/814/2/126.
- Zuccarello, F. P., Aulanier, G., and Gilchrist, S. A. The Apparent Critical Decay Index at the Onset of Solar Prominence Eruptions. *The Astrophysical Journal Letters*, 821(2):L23, April 2016. doi: 10.3847/2041-8205/821/2/L23.
- Zuccarello, F. P., Aulanier, G., Dudík, J., Démoulin, P., Schmieder, B., and Gilchrist, S. A. Vortex and Sink Flows in Eruptive Flares as a Model for Coronal Implosions. *The Astrophysical Journal*, 837(2):115, March 2017. doi: 10.3847/1538-4357/aa6110.



# List of publications

## Refereed

1. **Lörinčík, J.**; Dudík, J.; Aulanier, G.  
Saddle-shaped solar flare arcades, *The Astrophysical Journal Letters*, Vol. 909, 4 (2021), doi 10.3847/2041-8213/abe7f7
2. Dudík, J.; Del Zanna, G.; Rybák, J.; **Lörinčík, J.**; Dzifčáková, E.; Mason, H. E.; Tomczyk, S.; Galloy, M.  
Electron Densities in the Solar Corona Measured Simultaneously in the Extreme-Ultraviolet and Infra-Red, *The Astrophysical Journal*, Vol. 906, 118 (2021), doi 10.3847/1538-4357/abcd91
3. Joshi, R.; Schmieder, B.; Tei, A.; Aulanier, G.; **Lörinčík, J.**; Chandra, R.; Heinzel, P.  
Multi thermal atmosphere of a mini solar flare during magnetic reconnection observed with IRIS, *Astronomy & Astrophysics*, Vol. 645, 118 (2021), doi 10.1051/0004-6361/202039229
4. **Lörinčík, J.**; Dudík, J.; Aulanier, G.; Schmieder, B.; Golub, L.  
Imaging Evidence for Solar Wind Outflows Originating from a Coronal Mass Ejection Footpoint, *The Astrophysical Journal*, Vol. 906, 62 (2021), doi 10.3847/1538-4357/abc8f6
5. **Lörinčík, J.**; Dudík, J.; Del Zanna, G.; Dzifčáková, E.; Mason, H. E.  
Plasma Diagnostics from Active Region and Quiet-Sun Spectra Observed by Hinode/EIS: Quantifying the Departures from a Maxwellian Distribution, *The Astrophysical Journal*, Vol. 893, 34 (2020), doi 10.3847/1538-4357/ab8010
6. Heinzel, P.; Schwartz, P.; **Lörinčík, J.**; Koza, J.; Jejič, S.; Kuridze, D.  
Signatures of Helium Continuum in Cool Flare Loops Observed by SDO/AIA, *The Astrophysical Journal Letters*, Vol. 893, 34 (2020), doi 10.3847/2041-8213/ab9839
7. Dudík, J.; **Lörinčík, J.**; Aulanier, G.; Zemanová, A.; Schmieder, B.  
Observation of All Pre- and Post-reconnection Structures Involved in Three-dimensional Reconnection Geometries in Solar Eruptions, *The Astrophysical Journal*, Vol. 887, 71 (2019), doi 10.3847/1538-4357/ab4f86
8. **Lörinčík, J.**; Dudík, J.; Aulanier, G.  
Manifestations of Three-dimensional Magnetic Reconnection in an Eruption of a Quiescent Filament: Filament Strands Turning to Flare Loops, *The Astrophysical Journal*, Vol. 885, 83 (2019), doi 10.3847/1538-4357/ab4519
9. **Lörinčík, J.**; Aulanier, G.; Dudík, J.; Zemanová, A.; Dzifčáková, E.  
Velocities of Flare Kernels and the Mapping Norm of Field Line Connectivity, *The Astrophysical Journal*, Vol. 881, 68 (2019), doi 10.3847/1538-4357/ab298f
10. Dudík, J.; Mackovjak, Š.; Dzifčáková, E.; Del Zanna, G.; Williams, D. R.; Karlický, M.; Mason, H. E.; **Lörinčík, J.**; Kotrč, P.; Fárník, F.; Zemanová, A.  
Imaging and Spectroscopic Observations of a Transient Coronal Loop: Evidence for the Non-Maxwellian K Distributions, *The Astrophysical Journal*, Vol. 807, 123 (2015), doi 10.1088/0004-637X/807/2/123

## Non-refereed

1. Dzifčáková, E.; Zemanová, A.; Dudík, J.; **Lörinčík, J.**  
Diagnostics of non-thermal-distributions from solar flare EUV line spectra, *Proceedings of the International Astronomical Union*, Vol. 354, pp. 414 (2020), doi 10.1017/S1743921320001039

